Assessing the potential application of remote sensing and field surveying in identifying blind low enthalpy geothermal systems in Harihari, New Zealand

A THESIS SUBMITTED IN PARTIAL FULFILMENT

OF THE REQUIREMENTS FOR THE DEGREE OF

MASTER OF SCIENCE IN GEOLOGY

AT THE

DEPARTMENT OF GEOLOGICAL SCIENCES

UNIVERSITY OF CANTERBURY

BY JAMAL SUMMERS

UNIVERSITY OF CANTERBURY

2019

TABLE OF CONTENTS

LIST OF FIGURES AND TABLES

I. PROLOGUE

Renewable resources are an important part of human society and can offer a number of benefits to the environment. Geothermal activity, a type of renewable resource, is common frequently along the Australian-Pacific subduction plate boundary and can often be seen from the surface in the form of hot springs or geysers. However, not all geothermal activity can be seen from the surface as they can reside underground and remain undetectable. These hidden types are no less important than visible geothermal activity, only much harder to locate. Traditionally, the methods used for locating hidden geothermal systems been limited. Taking the initial steps to design and develop new innovative methods in identifying hidden geothermal systems, is the focus of this research. Success pivots on the understanding of permeability, fluid migration, fluid signatures that are favourable in locating low enthalpy hydrothermal systems. The current methods of tracing geothermal systems can often result in undesirable results that significantly raise exploration costs. Reducing risk through improvements in understanding and methodology is key.

II. INTRODUCTION

The objective of this thesis is to assess the potential application of utilizing remote sensing and field surveying to identify hidden geothermal systems on the West Coast of New Zealand. A hidden geothermal system is one that may not reach the surface (in the form of a hot spring or geyser) but is still active below. It is expected that the geothermal interaction with the overlying surfaces are to affect the overlying soil temperature, soil CO_2 flux and possibly surface temperature. Surface manifestations of geothermal activity such as volcanoes, hot springs, geysers are the major conduits for CO_2 movement from within the Earth to the Earth's surface and eventually the atmosphere (Fischer, T.P., 2019). By assessing these surface indicators, through remote sensing and field surveying could prove useful in identifying these hidden geothermal systems. The hydrothermal fluids that circulate the Alpine Fault present a unique opportunity, where shallow ascending heat resources could be harnessed for renewable energy production. In New Zealand, geothermal energy makes up 14.5% of the total energy generated (Ministry of Primary Industries 2015).

Remote sensing itself can be conducted by orbital satellites, aircraft, terrestrial sensory equipment and unmanned aerial vehicles UAV (Schowengerdt, R.A., 2006). UAV technology is rapidly advancing and gradually becoming more affordable and can be fitted with more accurate on-board multispectral sensory equipment. Although studies in the past have used remote sensing for geothermal resource identification, there remains no single study that has used remote sensing with field surveying that involved CO2 flux, soil temperature analysis and thermal imaging all simultaneously. This new methodology is still in its developmental stage. Vegetation could be used to identify fluid migration through geothermal and terrace interaction.

Aotearoa New Zealand's geology is dominated by the Alpine Fault, of which marks the point of tectonic collision between the Australian and Pacific plates. The Southern Alps are formed as a result of the mountain building processes from continental collision. The highly permeable region holds a significant volume of circulating fluid that feeds from percolation of meteoric water. Permeating fluids are heated and then ascend back up to the surface (Reyes, 2010). This cycle migrates hydrothermal fluid throughout the South Island, coupled with the CO_2 flow within the thermal fluids, interacts with the overlying vegetation. Agricultural analysis into how vegetation near hot springs is affected by an influx of heat and CO_2 could be measured and may lead to the discovery of indicative factors which signal crustal fluid flow. Industrial applications could involve the prospect evaluation of hydrothermal fluids for renewable energy development. UAV surveying is an attractive cost-efficient method that can assist future drill targets to ensure that future prospect selection can be made with greater accuracy.

Study Sites

Located adjacent to the Wanganui River on the West Coast of the South Island is the study site in Harihari. One of the main hot springs located in the area, is known as Amethyst hot springs, which was found after the flooding event in 2010 that uncovered it. This will be the primary research site. Ilam fields in Christchurch, New Zealand will be used as the control site where the same set of rules and methods applied in Harihari will be used. Both sites will be compared to each other to see how they perform under the necessary tests to assess their environmental indicators.

Statistics	**Harihari**	**Ilam Fields**
Area (M^2)	98,000	94,000
Perimeter (m)	1600	1500
Length (m)	620	470
Width (m)	220	230
Latitude	-43.163	-43.313
Longitude	170.621	172.238
Metres above sea Level (m)	100	23

Table 2.0: Table comparing the parameters of both field

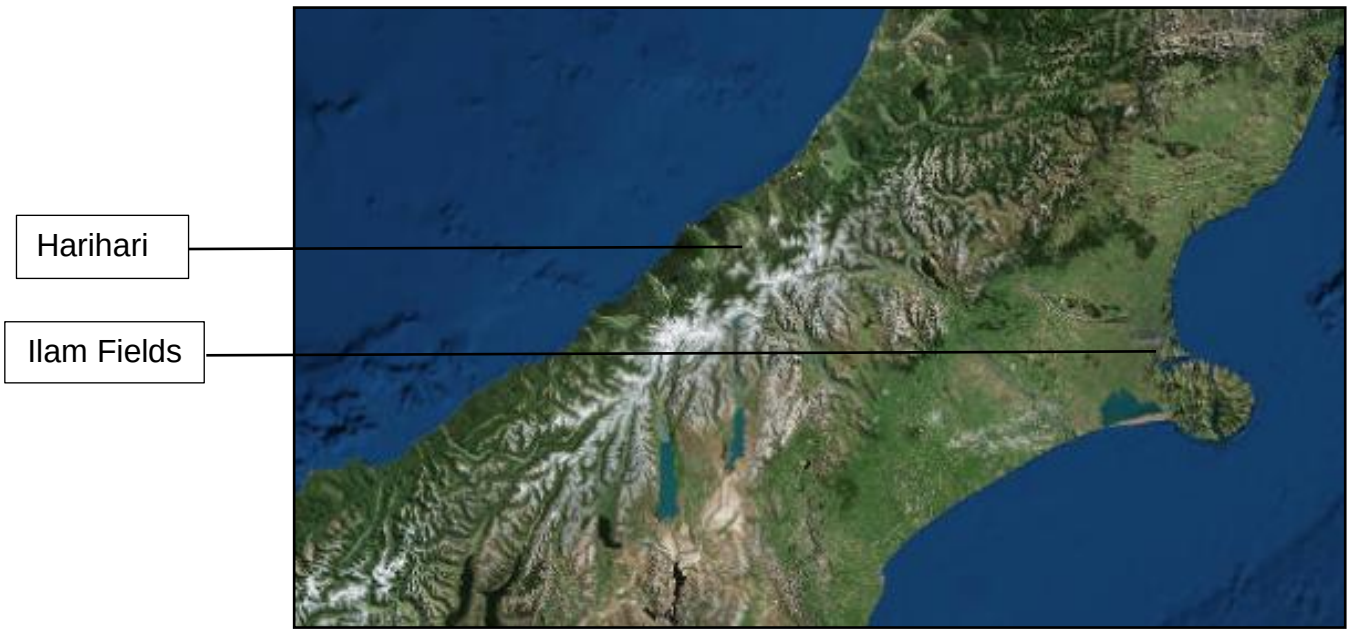

Figure 2.0: Map showing the location of both study sites

Geologic Setting Summary

Forty-two thermal hot springs are believed to be in the South Island, (Reyes, 2010) they are fuelled by the hydrothermal cycle of cold meteoric water penetrating down through the surface and then through the process of thermal upwelling is heated back up, expressed on the surface in the form of hot springs, fumaroles and rivers etc. The high permeability owes its existence through, not only porous rocks, but also the high level of rock fractures which act as conduits and reservoirs for fluid transfer through the crust.

Research Methods and Expected Goals

The environmental indicators that will be measured are Normalized Difference Vegetation Index (NDVI), thermal imaging, soil CO_2 flux and soil temperature at 20 cm and 50 cm deep. NDVI was introduced in 1970s by NASA when there was a requirement to numerically assess global land features from space. NDVI can calculate if an area is vegetation, water, bare soil etc. Furthermore, NDVI can distinguish between healthy and stressed vegetation and even lifecycle stage of the crop. It is based on the equation that [NDVI = (NIR – RED / NIR + RED)] where greater the infrared radiation reflected back, generally corresponds to a plant being healthier and vice versa.

To complement the infrared imaging, thermal imaging will run in tandem with the NDVI analysis that is conducted using UAVs. Through the processes of mapping and kriging, the polymerisation of these four indicators (NDVI, surface temperature, soil CO_2 and soil temperature) are expected to assist in answering if crustal fluid discharge can be detected using vegetation indices and will assist in attempting to develop new methodology in identifying blind geothermal activity. It is expected that where underlying geothermal activity is present, the soil directly above (if in contact) is to be affected as signified with spikes in the measured statistics mentioned above.

III. BACKGROUND LITERATURE

Geological Setting

It is estimated that in the South Island there are 60 mineral springs, of which approximately 42 are thermal (Reyes, A. G., and Britten, K., 2007). The majority of the thermal waters in the South Island discharge along the Alpine Fault, where subsurface temperatures are inferred to reach ~200 ^oC (Reyes, A.G., 2010) (Figure 3.02). The rest occurs around coastal Canterbury, Taieri Basin, West Coast, and Southland which when surveyed in 2010, showed surface discharges at temperatures of at least 16.7 to 66 ^oC (Reyes, 2010). The hot springs are caused by two main factors. First, the presence of anomalously high permeability in the uppermost 3-5 km of the crust due to the subsequent faults and fractures that arise during plate boundary deformation (Shi, et al., 1995). Though permeability in the Southern Alps is noted to be relatively porous, no relevant work has been published with information on the exact quantification of

the hydrologic properties of the fractured alpine schist (Cox and Sutherland et al., 2015). Hydraulic testing was done in the Wanganui River, near the Amethyst Stream 1.5km from the Alpine Fault, the rocks were found to be directly comparable with the Alpine schist at Copeland valley (Cox and Sutherland et al., 2015). The Alpine schist that formed the mountains around Copland valley are expected to have >10 m scale (intrinsic) fracture permeability of between 10^{-15} and 10^{-12} m^2 (Cox, et al., 2015).

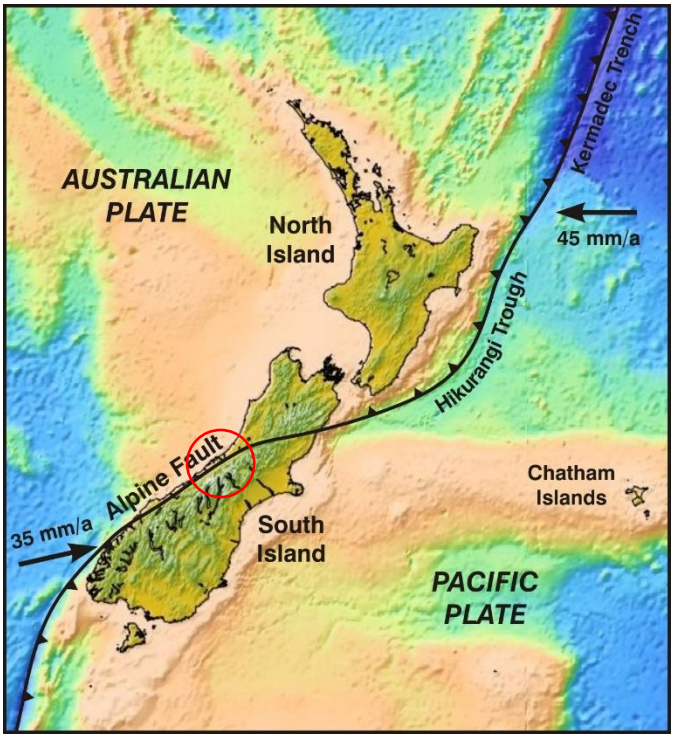

Figure 3.0: Map of New Zealand showing the tectonic plate boundary which is separated by the alpine fault (nationallibrary.govt.nz).Red circle represents the Wanganui catchment which is study site of interest.

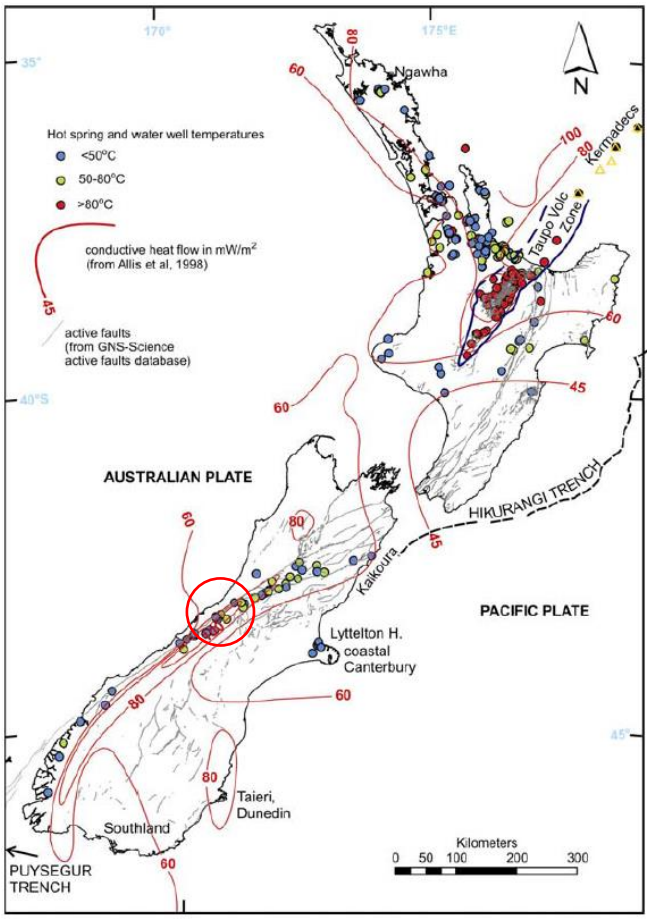

Figure 3.01: Map of New Zealand showing hydrothermal isotherms. The coloured circles represent hot springs and water well temperatures (Reyes, A.G., 2010).

The second factor being the occurrence of an abundance of available water and an unusual increase of heat along the Alpine Fault Zone, which is caused by rapid uplift of young metamorphic rocks on the eastern side of the plate boundary (Reyes, 2010). The Alpine Fault represents a point where continental collision is dominant throughout the southern landscape. As a result, it presents unique characteristics despite low seismicity, exhumation rate, conductive heat flow and displacement rates which are the highest along the deformation front (Wellman, 1979; Berryman et al., 1992; Allis, R.G., Shi, Y., 1995; Kohler and Eberhart-Phillips, 2003) (Figure 3.01). Mountain building processes during a continental collision and the exhumation of metamorphic rocks cause the geothermal gradient to rise (Koons and Craw 1991).

Southern Alps Hydrothermal System

In the South Island, heat transfer and the flow of hydrothermal fluids are affected by permeability of faults or fractures, topographic gradient and elevation (Reyes, 2010). The Marlborough Fault System allows inflow of cold meteoric water from the surface but also rapid ascent of hot solutions from depth (Reyes, 2010) (figure 3.02). High altitude and relief of the Southern Alps along with high rain fall on the western slopes of the mountains has caused topography-driven meteoric water penetration into the highly fractured metamorphic rocks (Koons and Craw 1991) (figure 3.03). Mineral waters from the Alpine fault are derived from the circulation of heated meteoric water gaining solutes from interacting with fault pulverised and metamorphic rock (Reyes, 2010) (figure 3.02). The subducted plates in the north-east and south-west of the South Island and metamorphic fluids at depth contribute to the flow of hydrothermal fluids (Koons and Craw et al., 1998).

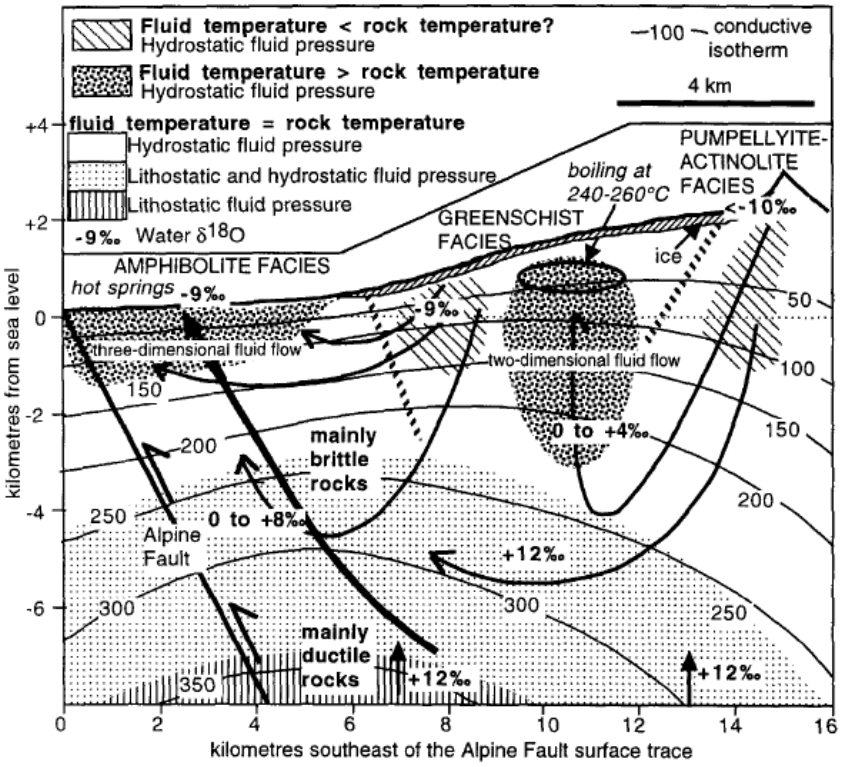

Figure 3.02: Cross-section through the western central Southern Alps tectonically induced conductive thermal anomaly and associated hydrothermal system. Fluid circulation paths and fluid temperature and pressure are speculative (Koons, 1987).

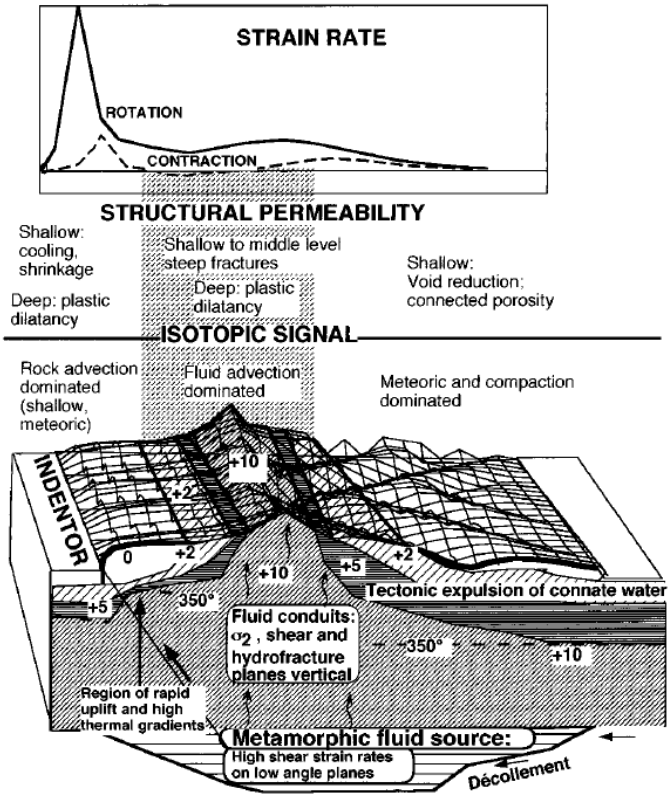

Figure 3.03: Basic diagram showing metamorphic fluid source and the correlation between mechanical and isotopic factors across an oblique collisional orogen (Alpine Fault). (Koons and Craw et al., 1998).

Carbon Dioxide Generation in Geothermal systems

The hot springs in the South Island of New Zealand release CO_2 through the oxidation of graphite and decarbonation of calcite at the greenschist-amphibolite facies boundary, and dissolution of rock mass calcite at shallower levels.

Diagram showing geothermal-terrace interaction

The simple diagram below compares the interaction between open and blind geothermal systems with the overlying terraces (figure 3.04). To the left of the diagram shows an open system where the hydrothermal fluids migrating upwards are reaching the surface compared to the blind system that also has upward migrating thermal fluids but is unable to reach the surface and remains at depth.

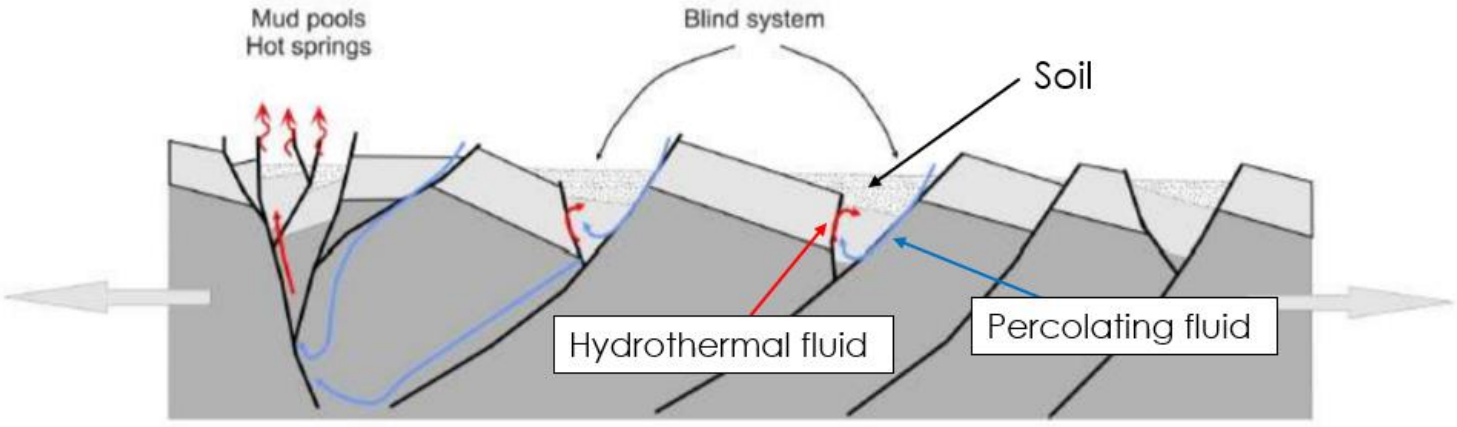

Figure 3.04: diagram that shows migrating fluids in open and blind geothermal systems.

Figure 3.05 displays an alternative depiction of what soil properties are affected when the migrating hydrothermal fluids interact with the overlying soil. The emphasis here is placed on the exact location of anomalous spikes.

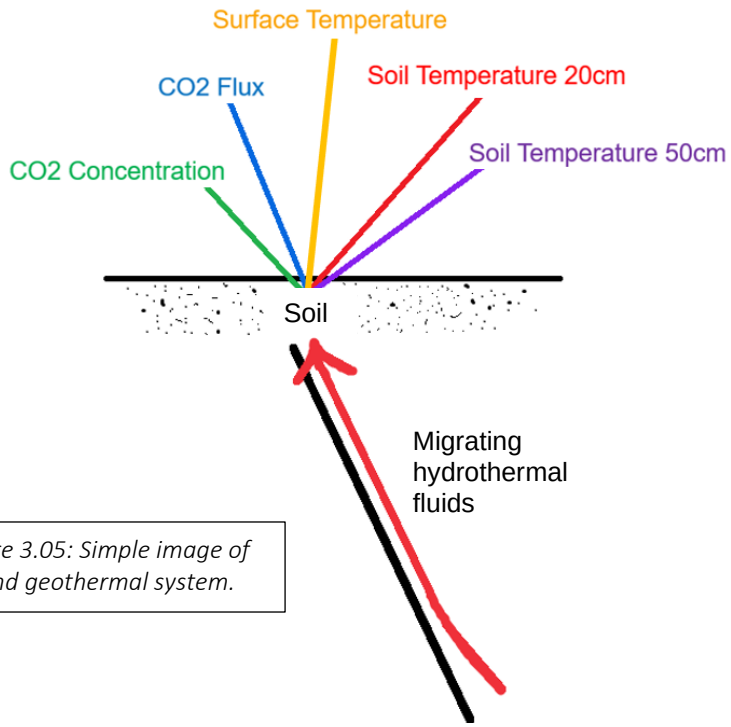

Figure 3.05: Simple image of a blind geothermal system.

Wanganui River

The Wanganui River is located in the West Coast of the South Island of New Zealand. The head waters are located north-west of the Southern Alps and flow for 55km where they exit into the Tasman Sea.

Study Site and Amethyst Hot Springs

During December 27th 2010 a significant flooding event lead to the uncovering of Amethyst hot springs. Located in the Wanganui River Valley 1.5 km upstream of the Wanganui River Bridge, ~5 km east of Harihari, Amethyst springs is, low enthalpy geothermal system which occurs in fault zones and permeable conduits (Hanson et al., 2015). The upper springs consist of seven outflows of elevated temperature (13.7-50.1 °C) and an additional three cold outflows (12.5 °C) which occur near the Amethyst Wanganui Convergence (Hanson et al., 2015).

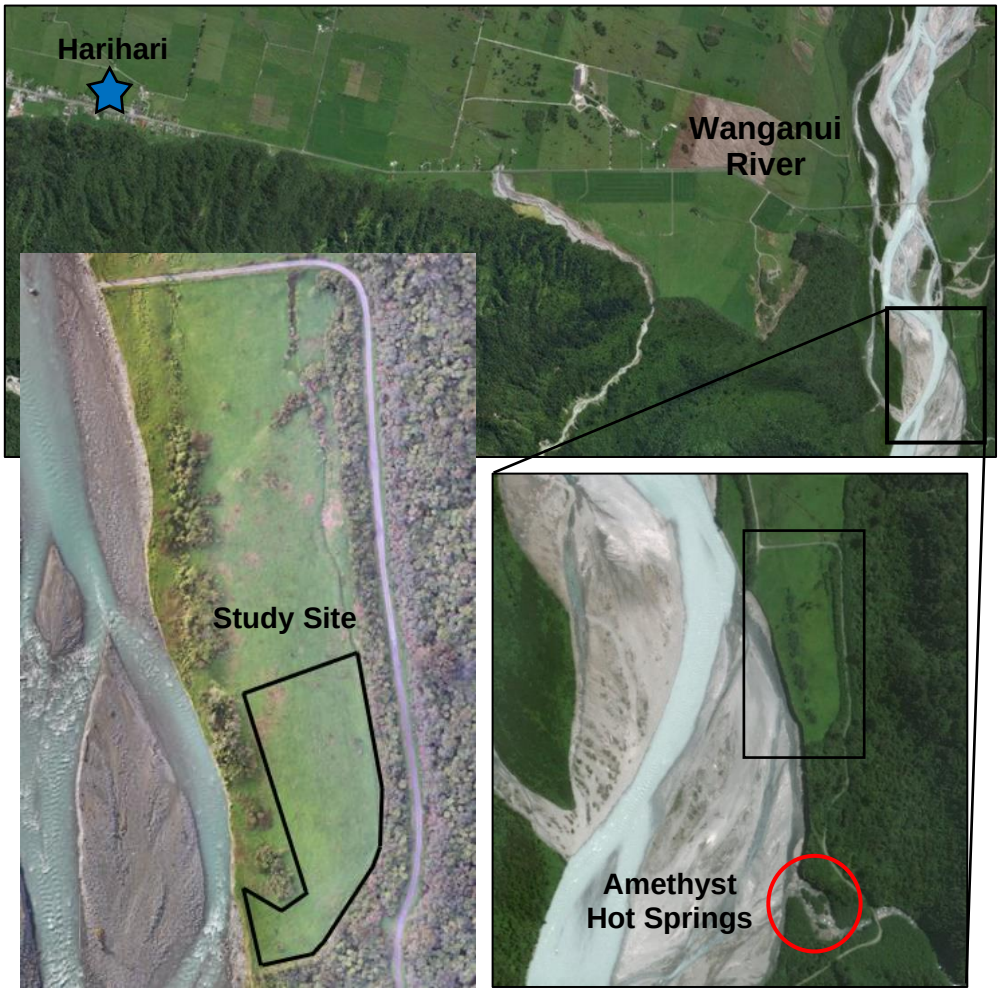

Figure 3.06: Maps showing location of the study site.

Sediment (fine sands to silts) make up the majority of ground cover on the river bank. The terrace above contains vegetation that consists of ryegrass, sorrel, docks, rushes and creeping buttercup, surrounded by native conifer-podocarp forest. The UAV and field surveys will be done on the terrace above the hot spring.

Additional Sites within the Wanganui River

While the field site in Harihari near Amethyst hot springs is the primary location of interest, there are three more springs within the Wanganui Valley that could be researched in the future; Hot Spring flat, Waitaha River hot springs and Smythe Hut.

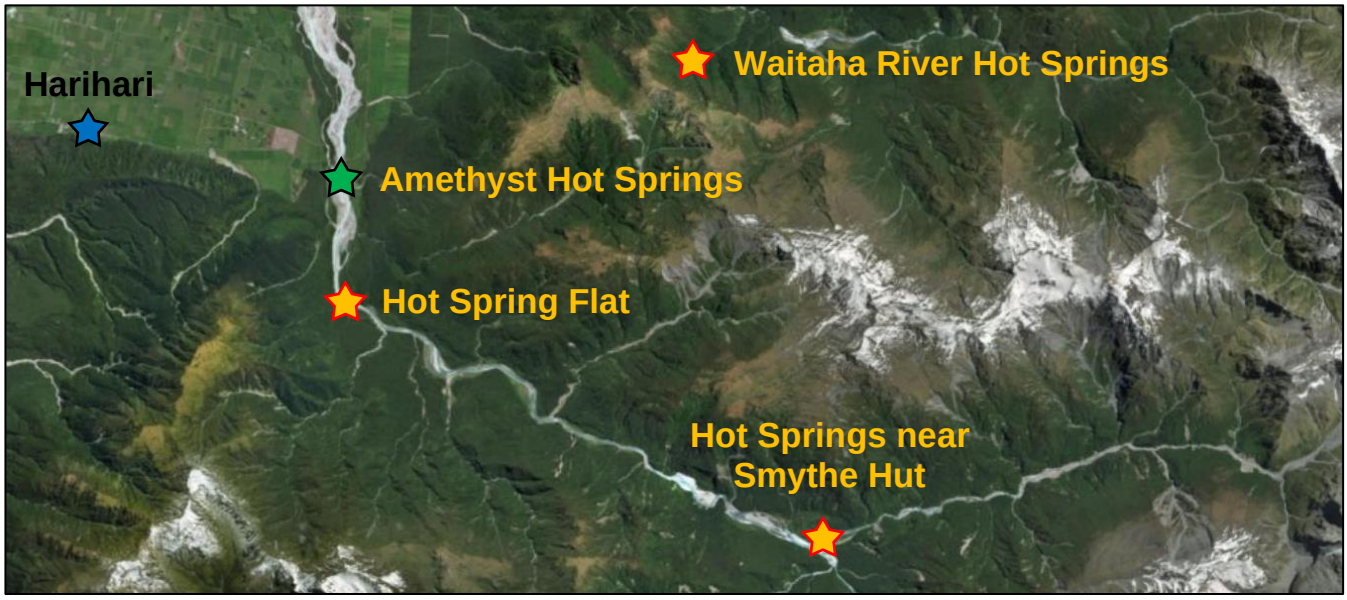

Figure 3.07: Extended view of the region west of Harihari displaying the locations of possible future areas for research.

Ilam Fields

Ilam fields in Christchurch will be used as the control site, to test and develop field methods and assess how vegetation with the absence of geothermal activity behaves.

Figure 3.08: Aerial view of Ilam fields In Christchurch, New Zealand.

Vegetation Indices

The practice of analysing infrared radiation is found to be valuable in a wide range of settings ranging from agricultural development to industrial applications. Vegetation is the Earth's natural linkage of soil, atmosphere and moisture, it displays obvious seasonal and annual changes (Cui, L.L., Shi, J., 2010; Zhang et al., 2011) and acts as a sensitive indicator of global climate changes (Schimel, D.S., et al., 2001; Weiss, J.L., et al., 2004). Continual development of multispectral sensory equipment has enabled researchers to evaluate vegetation properties using multispectral vegetation indices numerically. The main indices are listed below:

- Normalised Difference vegetation Index (NDVI).
- Soil-Adjusted Vegetation Index (SAVI).
- Enhanced Vegetation Index (EVI).

NDVI (Normalised Difference Vegetation Index)

The Normalised Difference Vegetation Index proposed by Rouse et al., (1974) is used to quantify vegetation cover using non-invasive methods. NDVI can be used to monitor local and global vegetation changes, which can indicate environmental changes brought by climate change (Qiu and Cao, 2011). NDVI has found uses in observing changes in crop production (Wardlow and Egbert, 2008), monitoring the effects of anthropogenic consequences in urban expansion (Fung and Siu, 2000), and was used to indicate climate changes by establishing relationship between climatic factors and NDVI (Nemani et al., 2003; Roerink et al., 2003). The use of the word reflectance refers to reflectance of infrared radiation unless otherwise stated.

The spectral reflectance of infrared in vegetation contrasts itself from other land features like rock, water, soil, ice and snow, clouds, and infrastructure (roads, buildings etc.), as unlike the aforementioned surface types, vegetation tends to absorb strongly the red wavelengths of sunlight and reflect in the near-infrared wavelengths (Chuai, X. W., et at. 2013). NDVI is calculated by measuring the differences in pigment absorption features in the red and near-infrared regions of the electromagnetic spectrum (Chuai, X. W., et at. 2013). Thus spectral reflectance profiles produced through NDVI being able to discriminate between vegetation and non-vegetation is based on calculated values. These values are collected from images produced from multispectral imaging.

$$\mathrm{NDVI} = \frac{\mathrm{NIR} - \mathrm{RED}}{\mathrm{NIR} + \mathrm{RED}}$$

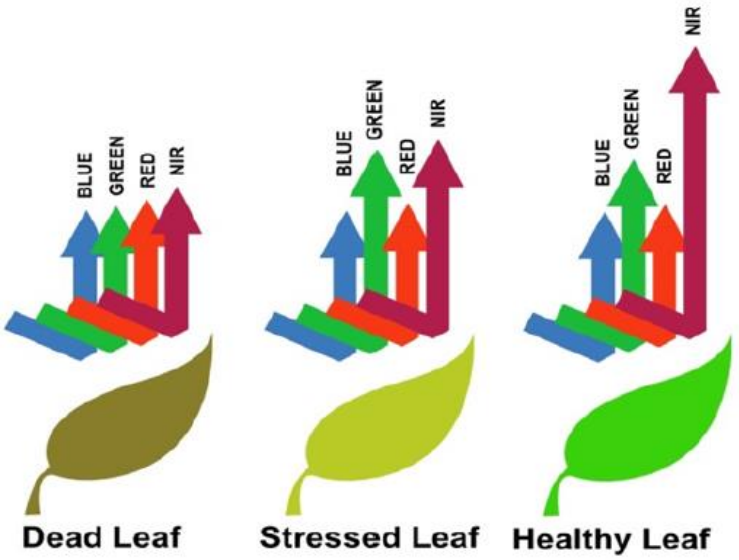

Figure 3.09: Cartoon graphic showing visible and NIR reflection between healthy and non-healthy vegetation (Gail Overton, 2014).

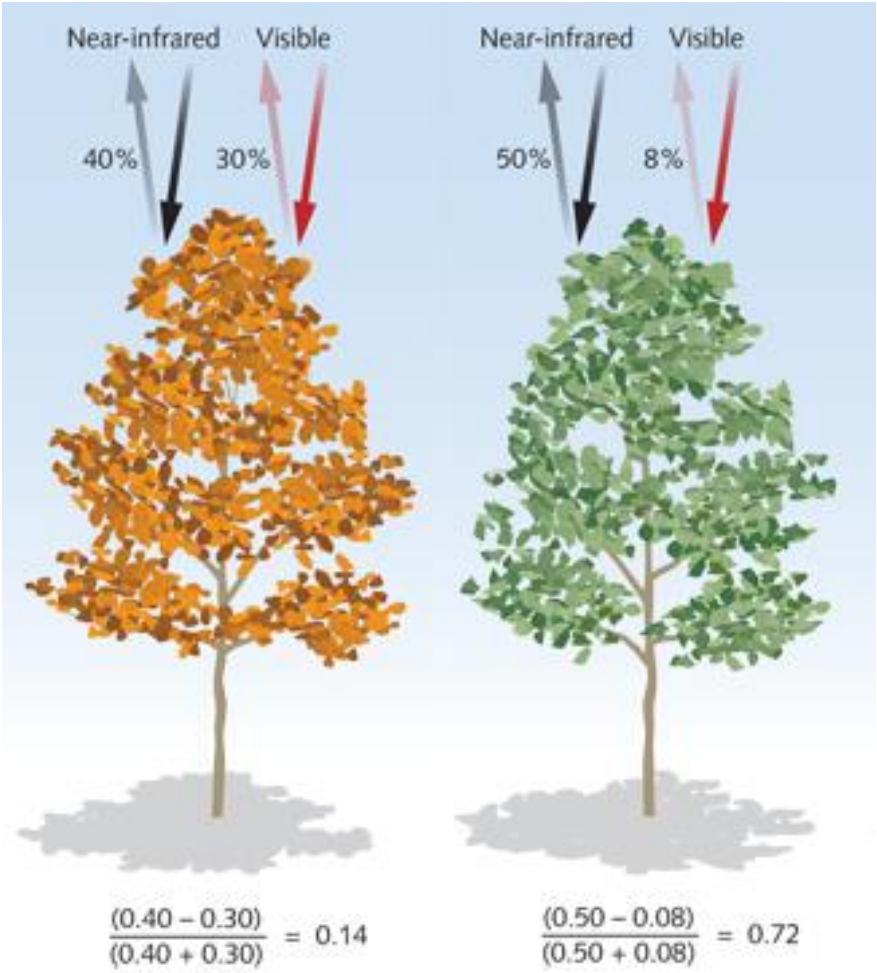

Figure 3.1: Simple cartoon showing what the expected spectral reflectance between dead, stressed and healthy leaves could be like (Weier and Herring, 2000).

NDVI values range from -1 to 1. Values of less than 0 indicate no vegetation, Very low values of NDVI (~0.1) typically link to arid regions of sand, rock and snow. Moderate values (0.2 – 0.3) correspond to shrub and grassland and high values (0.5 – 0.8) represent dense vegetation, temperate and tropical rainforests (Weier and Herring, 2000).

How Vegetation Affects NDVI

Photosynthesis is the process by which vegetation and other organisms use sunlight to synthesise nutrients from carbon dioxide and water. Photosynthesis in vegetation involves the green pigment chlorophyll that generates oxygen as a by-product.

The basic core components of photosynthesis that vegetation requires are:

- Sun Light: Electromagnetic radiation
- Water (H_2O)
- Carbon Dioxide (CO_2)

The water enters through the plant's stems and through chemical reactions using water to draw in nutrients from the soil and then evaporation (during day time), incoming photons within the visible spectrum reach plant leaves, the light absorbing chlorophyll pigment is energised where electrons are active (Pessarakli, M., 2016). This causes water to split into oxygen and hydrogen ions through this process creates more chlorophyll. Consequently, healthier plants will have more chlorophyll for light absorption compared to unhealthy plants which will have less chlorophyll pigments (Karnieli, A., et at., 2002). During transpiration, the process where water is replaced with carbon dioxide (CO_2), energy from incoming photon reactions convert carbon dioxide into glucose through a series of chemical reactions (Pessarakli, M., 2016).

The graph below shows a typical spectral reflectance graph between healthy and unhealthy vegetation and also soil (figure 3.11).

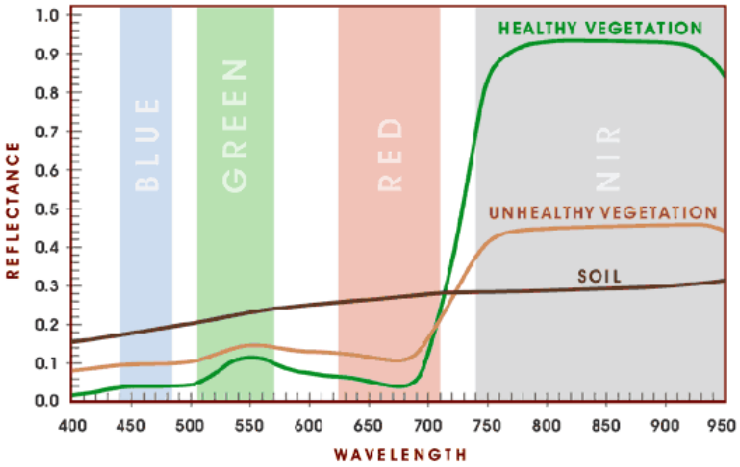

Figure 3.11: A graph showing the reflectance between healthy and non-healthy plants. (Aerial.crystalmark.co.uk)

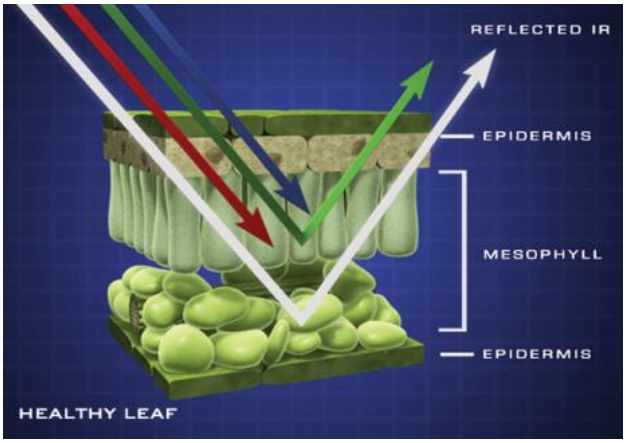

Figure 3.12: Graphic showing where electromagnetic radiation is being reflected (Charles Ichoku et at., 2002).

The same analysis can be done on different types of vegetation where unique patterns in spectral reflectance can be examined and can be used to identify plant types (figure 3.13). The graph below shows the spectral reflectance of corn, tulip popular trees and soybean under different wavelengths; visible, NIR, and shortwave infrared.

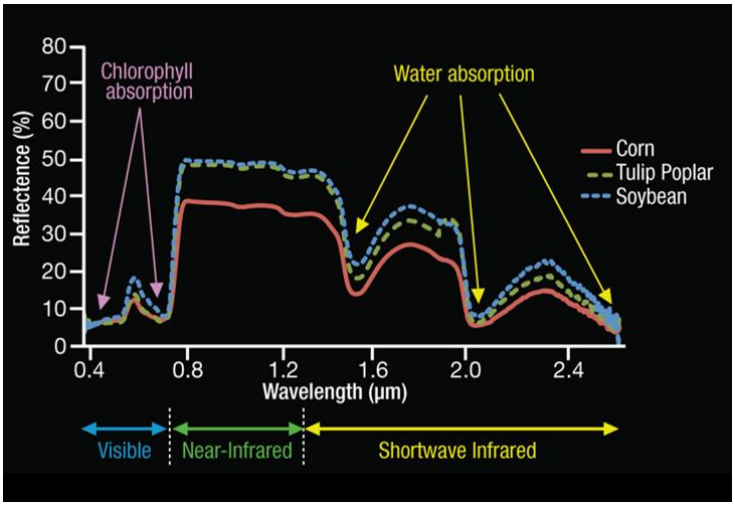

Figure 3.13: Graph showing spectral reflectance between different plant types (Karnieli, A. et at., 2002).

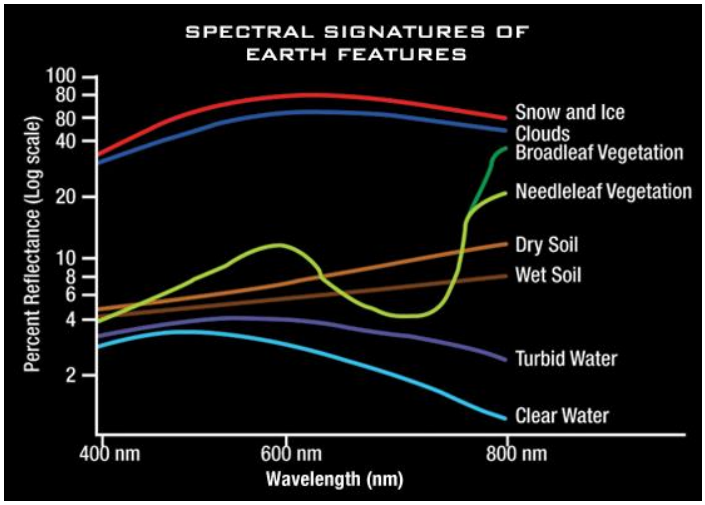

Figure 3.14: Spectral Reflectance from different sources (NASA, 2010).

UAS (Unmanned Aircraft Systems) Nomenclature

According to one of the specialized agencies of the UN, the International Civil Aviation Organization (ICAO), the term UAV refers to a pilotless aircraft that is remotely controlled. This can be done using a ground control station or the UAV can fly autonomously using a pre-planned flight route (ICAO, 2011). These two elements (ie; UAV and remote-control unit), are what is known as an Unmanned Aircraft System (UAS) (ICAO, 2011). In addition to the UAS being comprised of a platform (UAV) and a ground control station, UAVs are designed to carry what is known as a payload which is used to describe what the platform (UAV) is carrying. For example, in a scientific context the payload may refer to onboard multispectral sensory equipment (Gianluca Casagrande et al., 2018). Depending on the requirements, the use of UAV can be used across multiple applications such as aerial reconnaissance, agricultural monitoring, military surveillance and disaster management (Papa, U., 2018). Advancements in technology allowed UAS to be prominent choice in remote sensing due the advantages that UAS technology has offer, over other options like manned aircrafts which can be too costly, if the same level of accuracy can be achieved. Some benefits that UAS has offer include low cost, easier handling, and high flexibility. The ability to capture high quality aerial imagery at high resolution is possible with UAVs.

UAS (Platform) Classification

During recent decades, significant efforts have been made into the advances in UAV technology to better facilitate and cater to the requirements of users. For this reason, UAV design types have flexed out into a multitude of architypes, newly developed UAVs boast maneuverability and longer flight endurance (Angelov, P., et al., 2012).

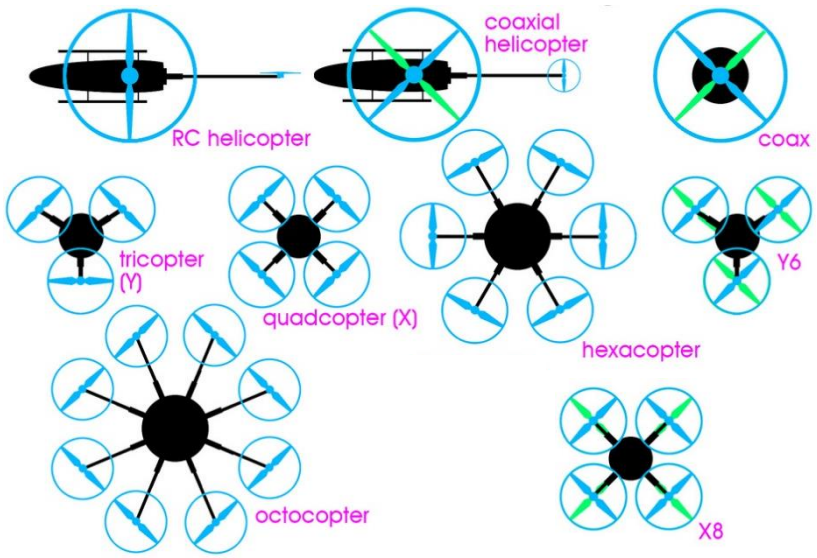

Figure 3.15: Diagram showing some examples of drone typology (Stephens, R., 2018).

The DJI Matrice Drone 210 will be used in the field for remote data survey (figure 3.16).

Figure 3.16: *DJI Matrice Drone 210 with Micasense Altum mounted.*

Multispectral Infrared Imaging

Multispectral imaging was first developed to remotely sense from space (Schowengerdt, R.A., 2007). Multispectral cameras record reflected, emitted or backscattered rays from an object or scene of interest in multiple bands of the electromagnetic spectrum including visible, infrared, near infrared and thermal, microwave and radio wave bands (Vollmer, M., and Möllmann, K.P., 2018) (figure 3.17).

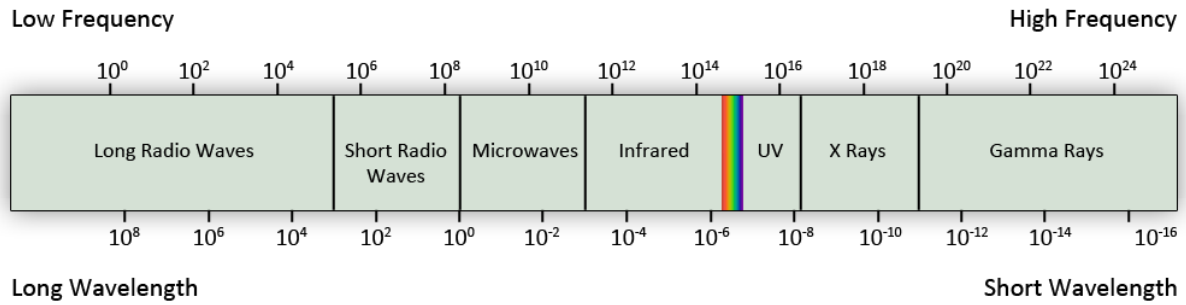

Figure 3.17: Graphic showing the electromagnetic spectrum (infinity-theory.com).

Infrared Radiation

Infrared technology has a wide array of uses in our daily lives, for example infrared lights can be found in wireless remote controls for household items like television and air conditioning units. DVD and CD players and other forms of optical media use infrared light to read and write information to physical media (discs). The use NIR (Near-Infrared) cameras find much of their use in range of settings, for example:

- Looking for defects in hot glass inspections
- Detection of scattering in skin, air in syringes, searching for blood vessels beneath skin within medical settings
- Night vision in military applications
- Residual light in atmosphere in surveillance/ security lights, crime scene imaging in forensic sciences and vision enhancement
- Measuring plastic absorption signatures in plastic sorting (recycling industry)
- Thermal radiation from high-temperature measurement in metal industry, coal/ metal furnaces
- Radiation emitting from stars/ dust etc. in astronomy using NIR sensors in telescopes
- NIR is used wafer inspections in microelectronics and solarcell industry
- Telecommunication equipment testing using scattered laser light

Figure 3.18: A list of possible uses for infrared radiation and their corresponding fields (Vollmer, M., and Möllmann, K.P., 2018).

Infrared imaging will primarily be used as the payload on UAV platforms. The exact ranges of the infrared (IR) spectrum are often disputed, for this reason of keeping definitions consistent, this thesis will use the Michael Vollmer and Klaus-Peter Möllmann definition of infrared from their book 'Infrared Thermal Imaging, Fundamental, Research and Applications, 2nd edition (2018)', which defines Infrared in (figure 3.19). IR is often referred to as a single spectral band, however there are three separate bands (four if thermal Infrared is included) that make-up the infrared spectrum:

- Near infrared (NIR) or Short-Wave Infrared (SWIR) ranges from 800 – 1,700 nm, is used primarily for imaging vegetation (NDVI) but has many uses in industrial/ commercial settings.

- Mid-infrared (MIR) operates from 1,550-5,000 nm, is typically used for imaging vegetation, soil moisture content, and forest fires.

- Far-infrared (FIR) or Long Wave Infrared (LWIR) ranges from 8,000-14,000 nm, is used for imaging soil, moisture, detecting geological features, silicates, clays, and fires.

- Thermal infrared, 800-14,000 nm, uses emitted instead of reflected radiation to image geological structures, thermal differences in water currents, fires, and for night studies. Radar and related technologies are useful for mapping terrain and for detecting various objects.

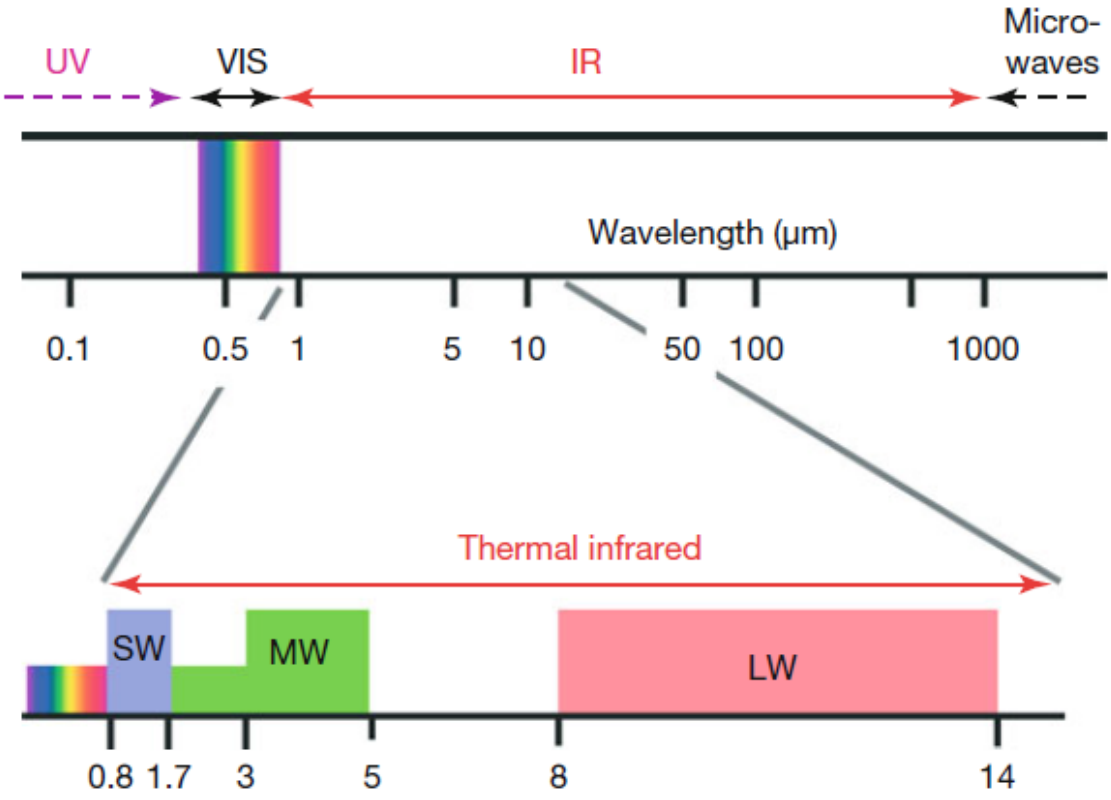

Figure 3.19: Diagram showing the constituents of the infrared spectrum (Vollmer, M., and Möllmann, K.P., 2018).

Infrared Camera Components

The diagram below shows the key components of an infrared (IR) camera illustrated in Michael Vollmer and Klaus-Peter Möllmann 'Infrared Thermal Imaging, Fundamental, Research and Applications, 2nd edition (2018)' (figure 3.2).

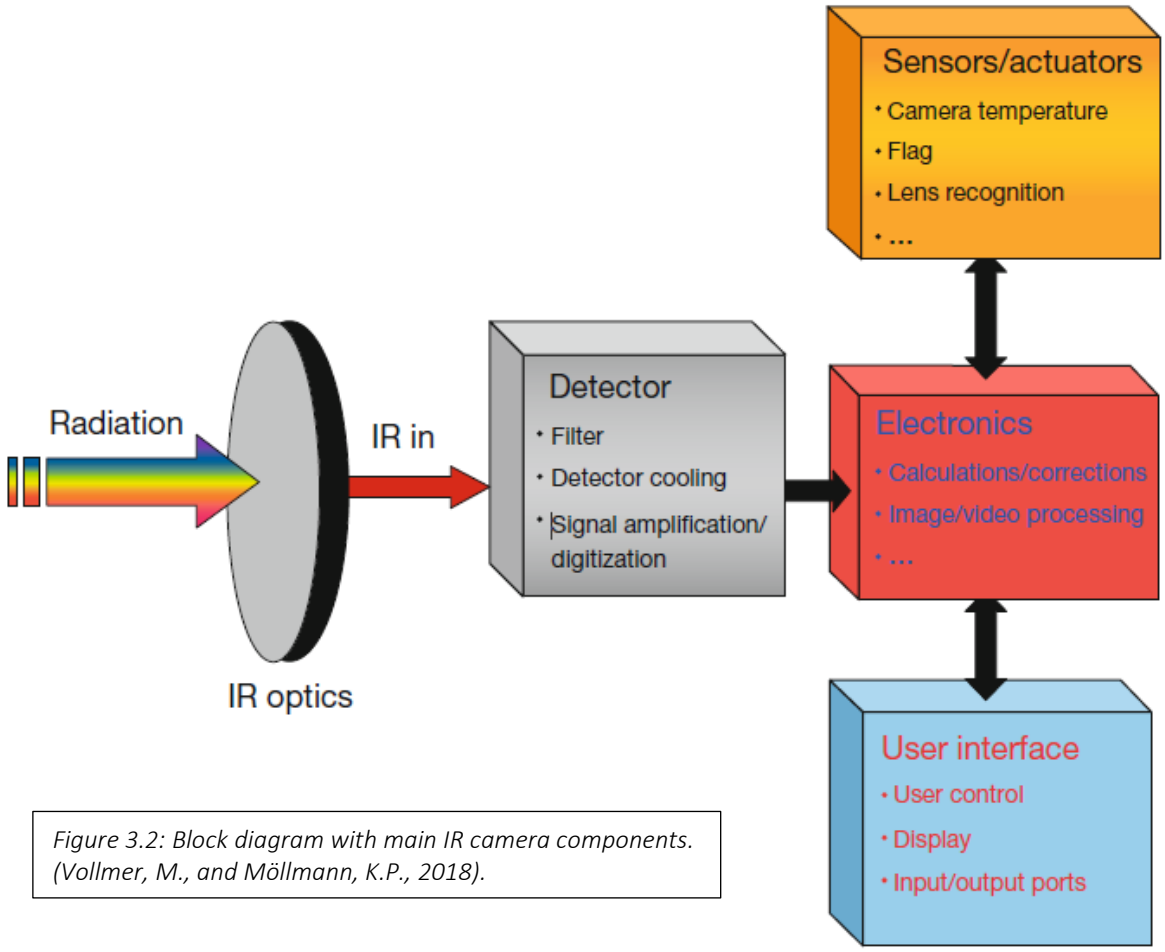

Figure 3.2: Block diagram with main IR camera components. (Vollmer, M., and Möllmann, K.P., 2018).

Infrared cameras capture incoming radiation, but with the use of an IR optic filter only infrared radiation gets through. IR radiation is detected using semiconductors made from specific chemical properties to detect incoming radiation and only allowing the desired wavelength energy through. The IR radiation is converted into a false colour image, where the visual image is used to represent the two-dimensional distribution of the IR radiation emitted by an object or a scene (Vollmer, M., and Möllmann, K.P., 2018). In thermal imaging, the image produced will show the temperature of an object or scene. The main components of an IR camera are the IR optics, detector, detector cooling and temperature stabilization unit which is used to increase image sensitivity, spatial resolution, spectral filtering and high-speed accuracy. Other key units in IR cameras include electronics that calibrate image quality and image processing, UI (User Interface), control ports and image display (Vollmer, M., and Möllmann, K.P., 2018).

Infrared Detector and Semiconductor Materials

A semiconductor is a continuous crystalline medium characterized by an energy band (Omnes, F., and Monroy, E., 2010) (figure 3.21). The material of the semiconductor dictates the wave threshold of energy that is detected. Due to the lattice structure of different metals, the band gap will change based on the chemical structure (i.e. valent electrons, net molecular charge etc.) which is heavily dependent on the energy requirements of electron transfer. This is because of the energy required to promote an electron from the lower energy valence band into the higher energy conduction band is controlled by the chemical structure of the semiconductor (Agba, E.H., et al., 2014) (figure 3.23). Special metals can function outside the wave bandwidth. The list below (Dahl, R., 2018) shows the bandwidth that materials typically operate in.

- Ultraviolet: 240 – 360 nm

  Gallium Nitride (GaN)

  Aluminum Gallium Nitride (AlGaN)

- aNear-UV to Blue: 395 – 530 nm

  Indium Gallium Nitride (InGaN)

- Yellow-green to Red: 565 – 645 nm

  Aluminum Gallium Indium Phosphide (AlGaInP)

- Near-Infrared: 800 – 1,700 nm

  Aluminum Gallium arsenide (AlGaAs)

  Gallium arsenide (GaAs)

  Lead(II) Sulphide (PbS)

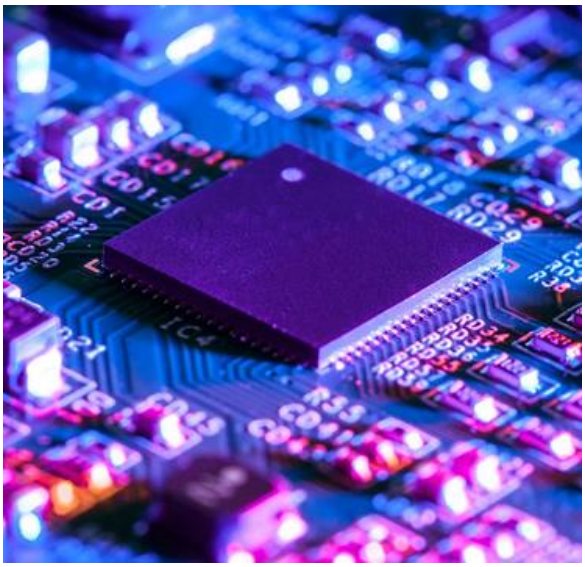

Figure 3.21: Semiconductor on circuit board (strath.ac.uk/electricalengineering).

- Medium-Infrared: 1,550 – 5,000 nm

  Indium Antimonide (InSb) / Indium arsenide (InAs)

  Mercury Cadmium Telluride (HgCdTe)

  Platinum Silicide (PtSi)

- Far-Infrared: 8,000 – 14,000 nm

  Mercury Cadmium Telluride (HgCdTe)

  Bolometers (metal layer made of an absorptive element sensitive to energy radiation)

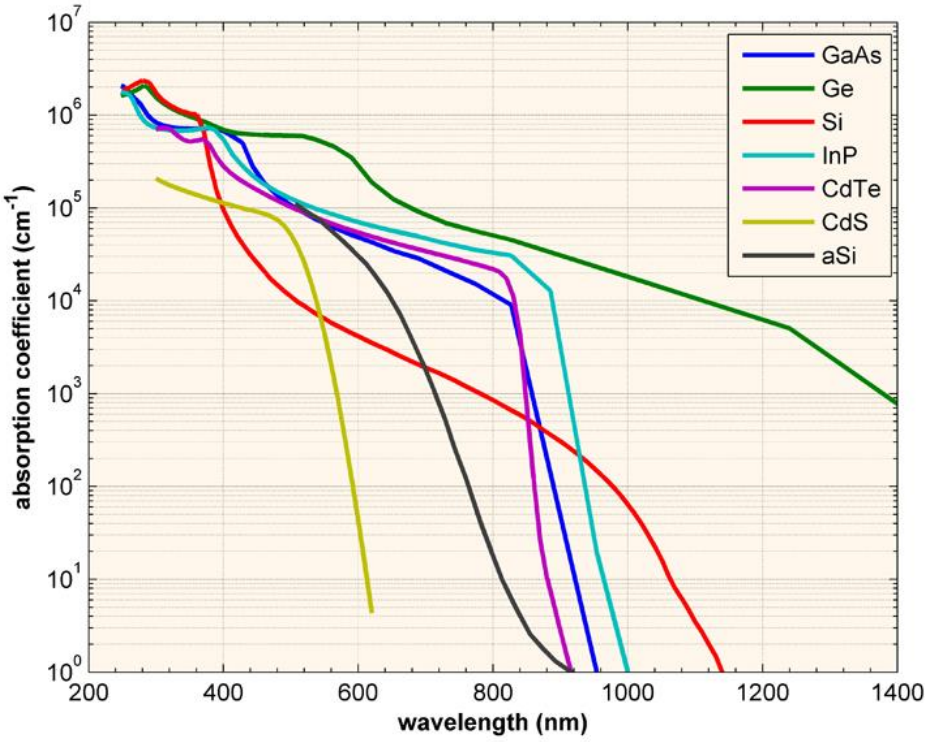

Figure 3.22: (Left) Graph that compares the absorption coefficient vs the wavelength different semiconductor materials are sensitive to (in a vacuum).

Absorption coefficient determines how far into a material, light of a particular wavelength can penetrate before it is absorbed (Rey, G., et al., 2017). The absorption coefficient depends on the material and also on the wavelength of light which is being absorbed. Semiconductor materials have a sharp edge in their absorption coefficient, since light which has energy below the band gap does not have sufficient energy to excite an electron into the conduction band from the valence band. Consequently, this light is not absorbed (Honsberg, C.B., and Bowden, S.G., 2019).

Semiconductors are sensitive to heat energy and need to be cooled at all times. As stated in Plank-Einstein's formula ($E = hf = hc/\lambda$), by increasing the energy, the band gap energy decreases and the emitted wavelength increases. Where E is photon energy, h is Planck's constant ($h = 6.62606957 \times 10^{-34}$ joules), c is the speed of light 299,792,458 ms^{-1}, λ is the wavelength of the photon (Sheng S. Li, 2006).

The formula states that wavelength and photon energy are inversely related, as one increases the other will decrease. This is important because wavelength of a photon dictates the energy, hence the energy requirements of the band gap (within a semiconductor) to move an electron from the valence band across the band gap and into the conductive band is restricted to certain wavelengths, that is, in very basic terms, how wavelengths of light is filtered during photon absorption by different materials semiconductor materials (figure 3.32).

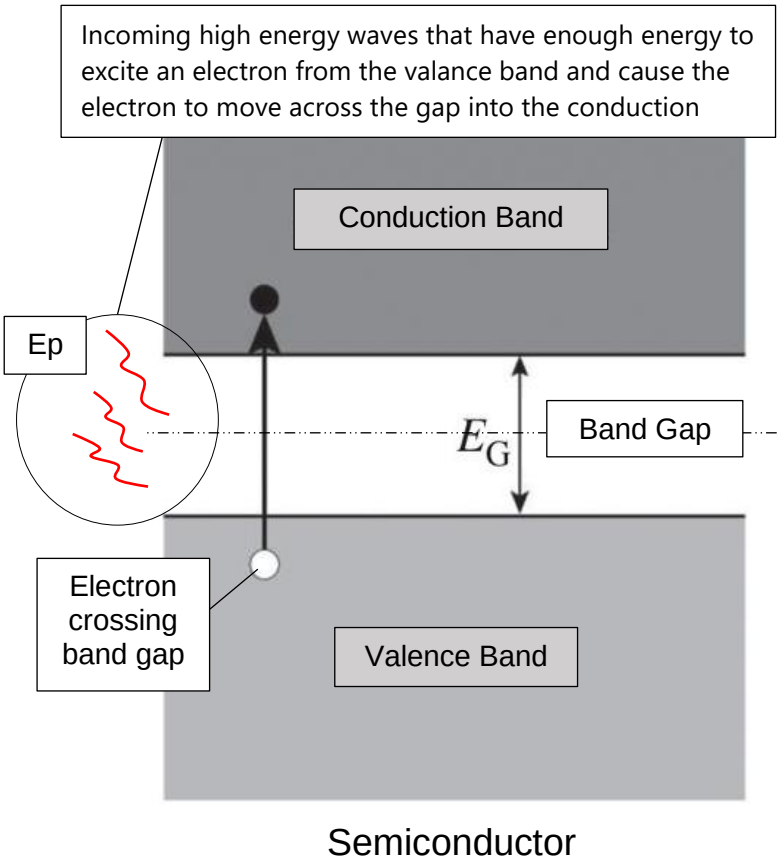

Figure 3.23: Very basic diagram, showing an electron moving across the band gap in a scenario where Ep (Photon Energy) > E.g. (Energy of Gap). Incoming light has enough energy to cause electrons to move. (Diagram made by this study)

Types Of Infrared Cameras

Some examples of IR cameras are listed below:

	Near Infrared	Medium Infrared	
			
Model	FLIR SC2600	FLIR SC6000	Agemema THV 550
Semiconductor	InGaAs (Indium Gallium arsenide)	InSb (Indium Antimonide)	PtSi (Platinum Silicide)
Wave Bandwidth	900 –1,700 nm	1,500–5,500 nm	3,000 – 5,500 nm
Resolution	640 × 512 pixels	640 × 512 pixels	320 × 240 pixels

	Far Infrared		
			
Model	FLIR T650sc	FLIR A35sc	FLIR SC2000
Semiconductor	Bolometer	Bolometer	Bolometer
Wave Bandwidth	7,500 – 14,000 nm	7,500 – 14,000 nm	7,500 – 14,000 nm
Resolution	640 × 480 pixels	320 × 240 pixels	320 × 240 pixels

Figure 3.24: list of IR cameras that range from NIR-MIR-FIR (Vollmer, M., and Möllmann, K.P., 2018).

Micasense Altum

The camera that will be used for the aerial surveys will be the MicaSense Altum and the Zenmuse XT2. The Altum has six onboard cameras. Blue, green, red, NIR, red-edge and thermal. The figures below show the technical specifications of the Altum.

Figure 3.25: (Left) Micasense Altum. (integraldrones.com.au)

Table 3.0: (Bottom Left) Table of Altum specifications.

Figure 3.26: (Bottom Right) Micasense Altum simple front view.

Table 3.01: (Bottom Right) Table of band-bandwidths.

	Multispectral	Thermal
Pixel size	3.45 µm	12 µm
Resolution	2064 x 1544 px (3.2 MP x 5 imagers)	160 x 120 px (0.01 K)
Aspect ratio	4 : 3	4 : 3
Sensor size	7.12 x 5.33 mm (8.9 mm diagonal)	1.92 x 1.44 mm
Focal length	8 mm	1.77 mm
Field of view (h x v)	48° x 36.8°	57° x 44.3°
Thermal sensitivity	n/a	< 50 mK
Thermal accuracy	n/a	+/- 5 K
Output bit depth	12-bit	14-bit
GSD @ 120 m (~400 ft)	5.2 cm	81 cm
GSD @ 60 m (~200 ft)	2.1 cm	41 cm

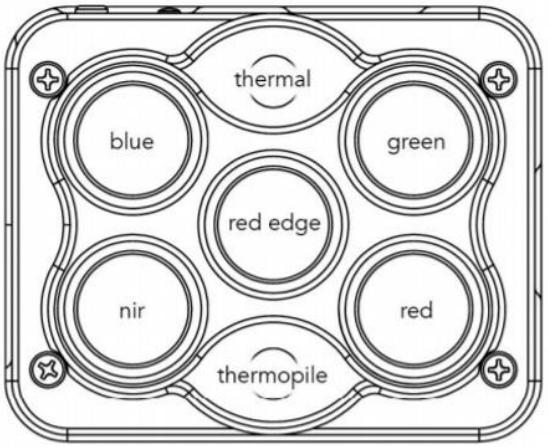

Name	Center	Bandwidth
Blue	475 nm	20 nm
Green	560 nm	20 nm
Red	668 nm	10 nm
Red edge	717 nm	10 nm
Near infrared	840 nm	40 nm
Thermal	11 µm	6 µm

Zenmuse XT2

The thermal camera Zenmuse XT2, below has the following technical specifications.

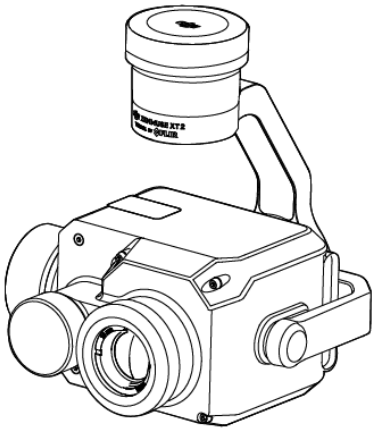

General	
Name	Zenmuse XT2
Max Controllable Speed	Tilt: 90°/s, Pan: 90°/s
Weight	629g
Camera (Thermal)	
Thermal Imager	Uncooled VOx Microbolometer
Digital Video Display Formats: Digital Zoom	640×512: 1x, 2x, 4x, 8x
Pixel Pitch	17 µm
Spectral band	7.5-13.5 µm
Exportable Frame Rates	<9Hz
Sensitivity (NEdT)	<50 mk @ f/1.0
Scene Range (High Gain)	640×512: -25° to 135 °C
Scene Range (Low Gain)	-40° to 550 °C
File Storage	microSD card
Photo Format	JPEG, TIFF, R-JPEG
Video Format	8 bit: MOV, MP4 14 bit: TIFF Sequence, SEQ
Camera (Visual)	
Sensor	CMOS, 1/1.7", Effective Pixels: 12 M
Lens	Prime lens: Focus at 8 mm, FOV 57.12°× 42.44°
Photo Format	JPEG
Video Format	MOV, MP4
Digital Zoom	1x, 2x, 4x, 8x
Video Resolutions	4K Ultra HD: 3840×2160 29.97p FHD 1290x1080 29.97p
Working Modes	Capture, Record, Playback Single Shot

Figure 3.27: (Top Left) Zenmuse XT2. (droneteck.ca)
Figure 3.28: (Top Right) Simplified image of Zenmuse XT2. (Zenmuse XT2 user manual).
Table 3.02: Specifications of the Zenmuse XT2.

Satellite Imagery and Radiometry

Courtesy of planet.com's multispectral imagery system, four-band (B, G, R, NIR) images of the surface of the South Island can be accessed. However most of the light that is reflected back from the surface is influenced by external atmospheric factors, such as rayleigh scattering (reflection and refraction), transmission and light energy absorption. These factors cause the image to be less representative of the surface, thus being less accurate for analysis. The reason for this discrepancy is caused by the constituents within the atmosphere (gases and aerosols) that affect the travel path of electromagnetic energy emitted from the sun to the surface.

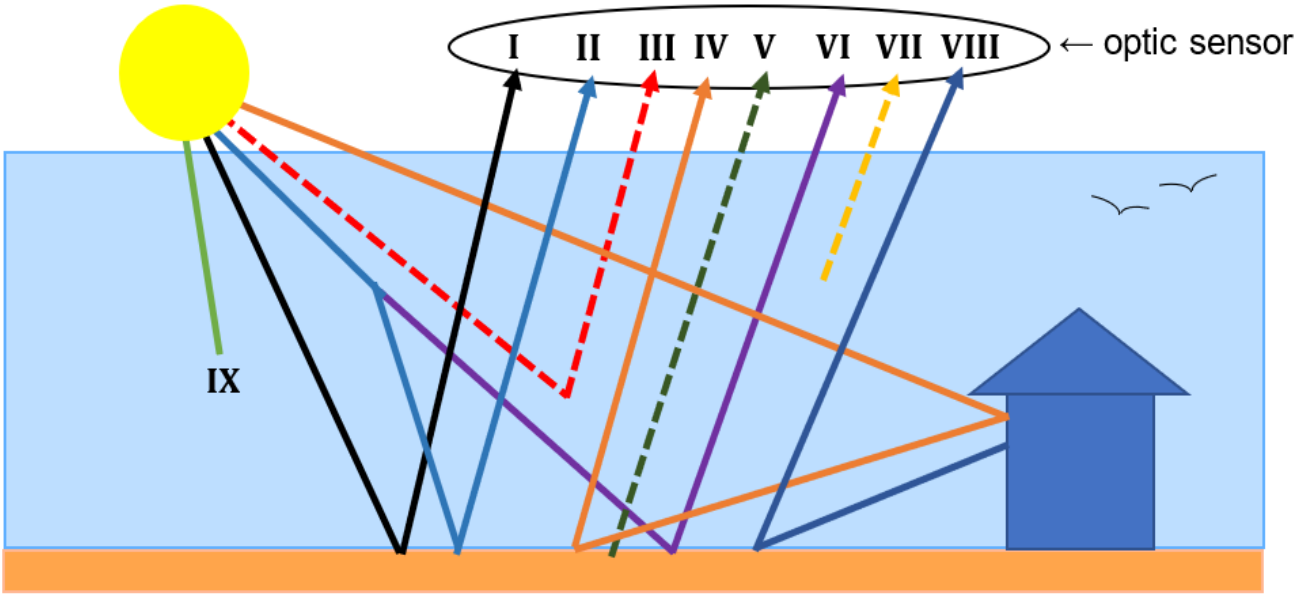

Figure 3.29: Graphic of the ways electromagnetic energy is influenced by the atmosphere and other objects.

I – (IR Reflectance) light travels down hits the surface and sensor. (This is the only one that is needed) II-IX is considered noise (radiance) as it disrupts the signal.

II – Refraction through a medium (gas or aerosol).

III – Rayleigh scattering caused by scattering of light off atmospheric gases or aerosols.

IV – Reflection off an object.

V – Mie scattering caused by dust, pollen, smoke, water droplets. Occurs when the particles causing the scattering are larger than the wavelengths of radiation in contact with them.

VI – Atmospheric transmission, energy passes through a medium (Grant, B.G., 2011).

VII – non-selective scattering Occurs in the lower portion of the atmosphere when the particles are much larger than the incident radiation. This type of scattering is not wavelength dependent and is the primary cause of haze at very long rangers (Grant, B.G., 2011).

VIII – Secondary object emitting its own light to the sensor.

IX – (Undetectable by sensor) caused by atmospheric gases, (water vapour, CO_2 and ozone O3) where the host absorbs the incident radiant energy, and is retained by a substance. The result is an irreversible transformation of radiation into another form of energy (Warren, R., et al., 2018).

Atmospheric Influence and Corrections

The atmosphere is made up of:

Atmospheric gases – Nitrogen, N_2 (78%), oxygen, O_2 (21%), argon, Ar (0.93%) small amounts of water vapor, H_2O, carbon dioxide CO_2 and ozone O_3 (Warren, R., et al., 2018).

Atmospheric Aerosols – Includes liquid and solid material suspended in air. The effects on remote sensing depends on size and shape distribution, particle shape, refractive index (Warren, R., et al., 2018).

This causes particle scattering with incident energy, the diagram (below) shows ways light is affected when coming into contact with atmospheric particles. Scattering is caused by small particles that are suspended in a medium of a different refraction index that diffuse a portion of the incident radiation in all directions. With scattering, there is no energy transformation, but a change in the spatial distribution of the energy. Scattering, along with absorption, causes attenuation problems with radar and other measuring devices (Warren, R., et al., 2018).

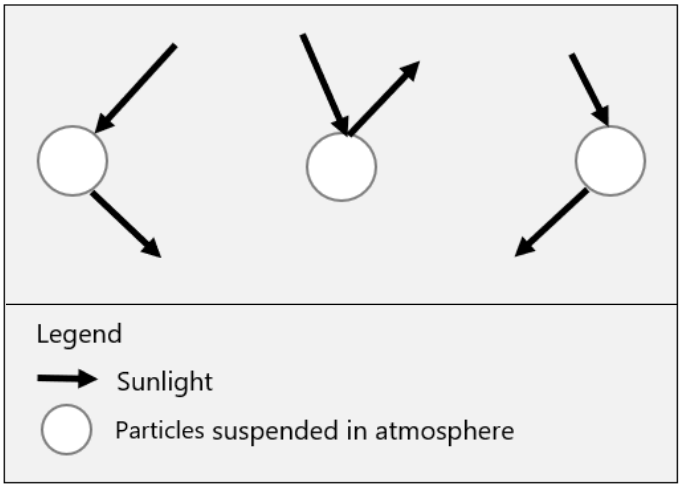

Figure 3.3: Diagram showing how sunlight interacts with particles suspended in the atmosphere. (Diagram made for this thesis).

Images taken from space for the purpose of mapping Earth's surface is limited by an absence scene fidelity. For example, the light that the sensor is able to record is known as radiance (amount of incoming radiation), but what is actually required is reflectance from the surface. This means that only through mathematical computational calibrations, an image can be taken from radiance (raw) to reflectance (calibrated). However because these images are being taken from above the atmosphere, they are known as Top Of Atmosphere radiance (TOA) and TOA reflectance.

TOA Radiance is the amount of radiation coming from a per unit solid angle per unit projected area in the form of radiation flux that was emitted, transmitted and reflected. This is the data stored as digital numbers (DN) and converted to radiance at the sensor.

TOA reflectance is the TOA radiance that has been corrected with solar zenith angle, sun distance and exo-atmospheric irradiance (intensity). This reflectance of radiation from the surface has been affected by gases, scattering and aerosols. Surface reflectance that has atmospheric influences minimized and corrected is an accurate representation of the surface. Derived from calibrated radiance images, surface reflectance is the final form of TOA radiance → TOA reflectance → Surface reflectance.

Image Accuracy

The images that are being produced are made up of what is known as pixels. High resolution images can have thousands of pixels, where low to medium resolution images typically have around 250-600. Each pixel typically holds data such as the atmospheric scattering or emitted radiation, followed by radiation reflectance and emission. This is where the actual radiometric calibrations take place by correcting the digital numbers stored in the pixel by applying radiometric calibrations to each number stored in every pixel, this process increases the accuracy of images.

This is especially important when sensors are observing the same scene through a time lapse over a day. For accurate radiometric calibrations, metadata included with the satellite imagery must include but not limited to atmospheric properties, aerosol distribution and sun angle and distance etc.

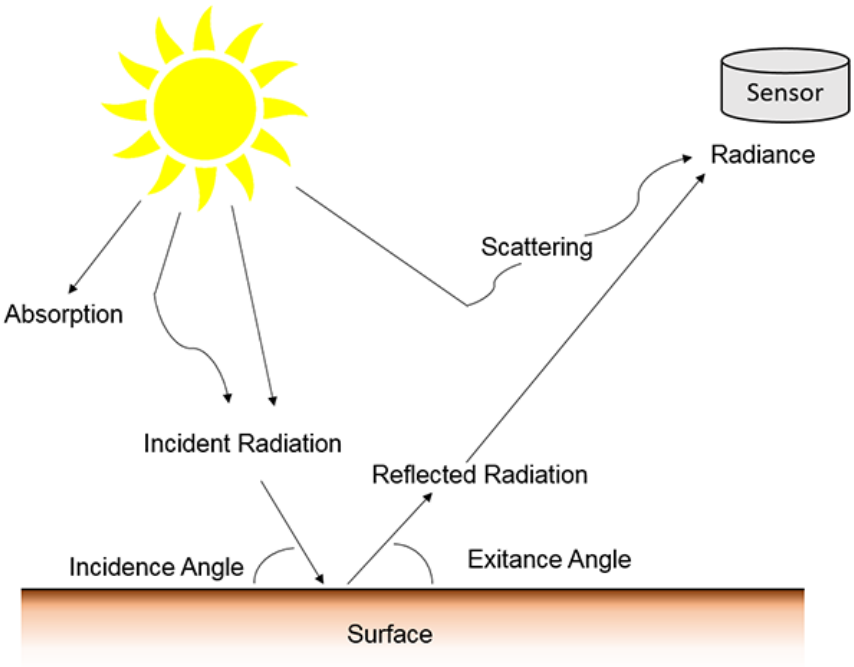

Figure 3.31: Alternative diagram showing a simplified depiction of how sunlight travels through the atmosphere (Humboldt University, 2019).

Radiometric Calibrations

The calibration of radiometric data follows three key steps (Planet API, 2019):

Step 1: The digital raw numbers are processed into Top Of Atmosphere (TOA) radiance. This is systematically done at the sensor before the data reaches the user.

Step 2: Converting TOA radiance to TOA reflectance. Requires earth sun distance, solar zenith angle, exo-atmospheric irradiance etc.

The first step involves converting the DN (Digital Numbers) from TOA radiance to TOA reflectance. An example of image with uncalibrated image radiance to calibrated TOA reflectance is shown below.

Figure 3.32: Satellite image of the United States Before and after radiometric calibrations (Planet.com, 2019).

As previously mentioned, the raw digital numbers (DN) are stored in each pixel of the image and must be calibrated for better accuracy. The equation for TOA reflectance rescales the DN based on specific variables in the metadata, on scientific principles of radiation previously discussed.

$$\rho\lambda = \frac{M_\rho Q_{cal} + A_\rho}{\cos(\theta_{SZ})}$$

$\rho\lambda$ = TOA reflectance
θ_{SE} = Local sun elevation angle provided in the metadata
θ_{SZ} = Local solar zenith angle; $\theta_{SZ} = 90° - \theta_{SE}$
M_ρ = Band-specific multiplicative rescaling factor from the metadata
A_ρ = Band-specific additive rescaling factor from the metadata
Q_{cal} = Quantized and calibrated standard product pixel values (DN)

Step 3: Convert TOA reflectance to Surface Reflectance

Mathematical corrections which involve using the variables stored in the metadata, that being of atmospheric conditions (weather), time of day etc. This step is required for NDVI calculation for satellite imagery.

Soil CO_2 Gas Flux Analyser

Measuring CO_2 flux from soil requires specialized equipment such as the West Systems flux meter. The West Systems CO_2 flux analyser requires the accumulation chamber to be placed on the ground where gas from the soil accumulates in the fixed volume chamber over time. The Juno hand-held is able to measure the change in gas concentrations rise over the accumulation period and the rate at which concentrations increase in the fixed volume accumulation chamber that is proportional to the soil gas flux rate.

The soil CO_2 fluxes reported are the slopes of the least-squares linear regression best-fit lines through the West System's CO_2 concentration (displayed on the juno handheld) versus time profiles at each survey site. A uniformly distributed transect survey was used to ensure the data was uniformly distributed with respect to space and to facilitate the potential preparation of cross-sectional profiles through the surveyed areas.

Normal Ranges of Measured Variables

This thesis reports NDVI, CO_2 flux, soil temperature and surface temperature. These variables will differ from location to location. The four paragraphs below show the normal ranges (of NDVI, CO_2 flux, soil temperature and surface temperature) from cited literature.

NDVI

Average NDVI value within the regional area (2km radius from centre of respective fields) derived from satellite NDVI that surrounds the study site in Harihari and Ilam fields is 0.517 and 0.380, with standard deviations of 0.167 and 0.213 respectively. These values were calculated using Planet.com's radiometric data and then using the fishnet function in arcMap to calculate the mean value of each point. Though it must be said these values are variable and just an indication of what the NDVI value is.

CO_2 Flux

The CO_2 flux to the atmosphere from degassing of hot springs (within the Alpine fault zone) is 1.9 to 3.2 $\times 10^8$mol/yr, which is 30–50% of the flux to the near surface environment (Menzies, C.D., et al., 2017). Carbon dioxide concentrations reported by Giggenbach and others (1993), along eight sample sites on the Alpine Fault ranged from 1 to 935 mmol/mol with an average of 267 mmol/mol. The method of recording CO_2 concentrations in the study were noted that 'all samples are free gases that were collected into lead glass bottles into evacuated 300ml pyrex flasks, that were later analysed by gas chromatography with H_2 as the carrier gas and an ultrasonic detector' (Giggenbach, W.F., et al., 1993).

Soil Temperature

Data sourced from NIWA (National Institute of Water and Atmospheric Research) indicate that average soil temperature in the region around Harihari at 20cm deep is '11.8 °C and 50cm and 13.1 °C in May of 2019' (The National Climate Database (NIWA), 2019). Regional Ilam soil temperature at '20cm and 50cm is 12.5 °C and 14.0 °C' respectively (The National Climate Database (NIWA), 2019).

Surface Temperature

NIWA datasets for mean surface temperature for the regional area around Harihari is '6.64 °C and 4.6 °C' for Ilam fields in May of 2019 (The National Climate Database (NIWA), 2019. These values along with soil temperature values were measured across several stations around Ilam and Harihari (The National Climate Database (NIWA), 2019).

Similar Studies

There are multiple new studies from Universities around the world which have looked at assessing geothermal presence with remote sensing and field work, three of which are summarised below.

In 2016 a paper out of the University of Auckland studied the heat loss over the Waikite Geothermal Area in New Zealand. The methods used for their study involved UAV flights over the geothermal area (Harvey, M.C., et al., 2016). They used Agisoft to create mosaics and photogrammetry DEM (Digital Elevation Models) of the field, that were calibrated with ground control points and thermal soil probes. 'The mean surface heat loss 43 +/- 12 MW is probably a minimum, as a small proportion of thermal water is not visible from above' (e.g. obscured by vegetation) (Harvey, M.C., et al., 2016).

However, the results from that study are likely to unreliable because measuring heat loss through different surface types (grass, trees, ground and water) the thermo-emissivity index of grass, trees, ground and water are all different yielding variable results. While approximate difference between surface types appear small (figure 3.12) when dealing with large surface areas such as the Waikite geothermal field (~2.2 km^2) the error margins can be greatly expanded in the final calculations. Thus, the estimated value is not likely indicative of the heat loss within the Waikite geothermal system.

The table below from Chen and others (2015) shows the average emissivity for two TIRS (Thermal Infrared Sensor) channels at different land covers of FROM-GLC (Finer Resolution Observation and Monitoring of Global Land Cover) (Chen, D., et al., 2015).

Emissivity Class	Mean	
	TIRS-10	TIRS-11
Cropland	0.971	0.968
Forest	0.995	0.996
Grasslands	0.970	0.971
Shrublands	0.969	0.970
Wetlands	0.992	0.998
Waterbodies	0.992	0.998
Tundra	0.980	0.984
Impervious	0.973	0.981
Barren Land	0.969	0.978
Snow and ice	0.992	0.998

Table 3.03: Surface types and their respective emissivity values. Note emissivity is a ratio from 0 to 1. (Table sourced from Chen, D., et al., 2015).

Another study by Kevin and others (2013) from the University of Pittsburgh which looked at using thermal infrared to detect minerals associated with geothermal activity. The geothermal fields that were studied included Davis–Schrimpf and Sandbar Geothermal Field in California, USA. The key minerals overserved were Anhydrite; Gypsum; Smectite; Epsomite; Microcline; Quartz. The minerals react differently to electromagnetic radiation because of their varied chemical composition, the spectral graphs produced were able to distinguish each mineral from each other.

The graph below from Kevin A.R., et al., 2013 shows the absorption spectrum of minerals found in geothermal environments.

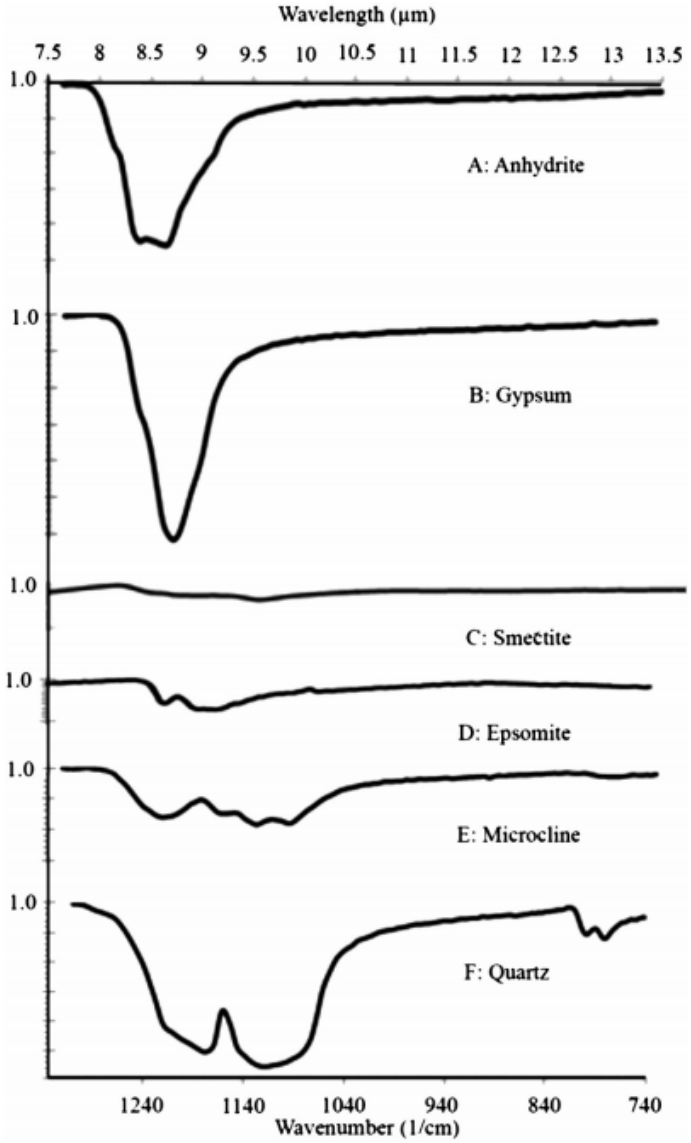

Figure 3.33 (left): Absorption spectrum of minerals found in geothermal environments (Kevin A.R., et al., 2013).

The study noted that the level of mineral representation is not 100% accurate 'Anhydrite ($CaSO_4$) appears to be underrepresented in these maps, which is likely due to the PPI end member spectrum containing some percentage of anhydrite in addition to the Mg-sulphate' (Kevin A.R., et al., 2013), other small inaccuracies through alteration are also noted by the study. The paper concludes with 'Thermal infrared spectroscopy and remote sensing have been shown to be useful tools for the detection of numerous common and less common rock-forming minerals and alteration products such as those found in this study' (Kevin A.R., et al., 2013). But suggests that increased spatial resolution would allow for greater detection accuracy. Like with most papers in this field, they all note that their studies are limited by the technology available, more specifically: the resolution of image data as this would increase analytical accuracy. This study is only relevant to study areas that have an absence of biological cover.

IV. METHODS

Field Methods: Study area and UAV

Collecting field data with many different pieces requires a meticulous approach. This chapter 4 focusses on methods of data collection from beginning to processing. The study area is set up through the flight planning software by maps made easy on IOS. The app allows the UAV flight path to be preset to ensure there is enough overlap by adjusting flight speed and height. This is done so that the 1000+ single images taken over the course of the flight can be aligned together as a single mosaic in the post-processing stage.

The UAV (DJI Matrice 210) flies over Ilam fields at 60m which is the maximum height allowed by the Christchurch International Airport. The flights are done with the Altum then Zenmuse XT 2. Before and after the flights, UAV gyroscope and reflective plate light intensity calibrations are required to adjust the overall scene brightness as the sun angle changes before and after flight. Flights can take up to 30 minutes with batteries being required to be switched over halfway. These corrections are required for accuracy.

Figure 4.0: Field crew preparing the DJI Matrice Drone flight plan in Harihari.

Infrared Camera – Altum

The MicaSense Altum is a six-lens camera that produces six images (blue, green, red, red-edge, NIR and thermal) per shot. The data is stored on the extractable SD card.

Figure 4.01: DJI Matrice with the Micasense Altum attached.

Thermal Camera – Zenmuse XT2

The Zenmuse thermal optics is able to record images in 640x512 radiometric JPG (.rjpg), 60fps 4K video (visible) and (640x512) thermal video 30fps.

Figure 4.02: DJI Matrice with the Zenmuse XT2 attached.

Image Processing

Altum – Infrared

All band 3 and band 5 images are taken into Agisoft pro using the following sequences:

Align Photos → Build Mesh → Build Orthomosaic → Export TIFF.

This will turn 2000+ images into large orthomosaics. The band 3 and band 5 images are taken into arcMap 10.4, using the tool 'map algebra' and the NDVI formula:

("Band5.tif"-"Band3.tif") / ("Band5.tif" + "Band3.tif")

Which calculates on a pixel by pixel basis the Normalized Difference Vegetation index.

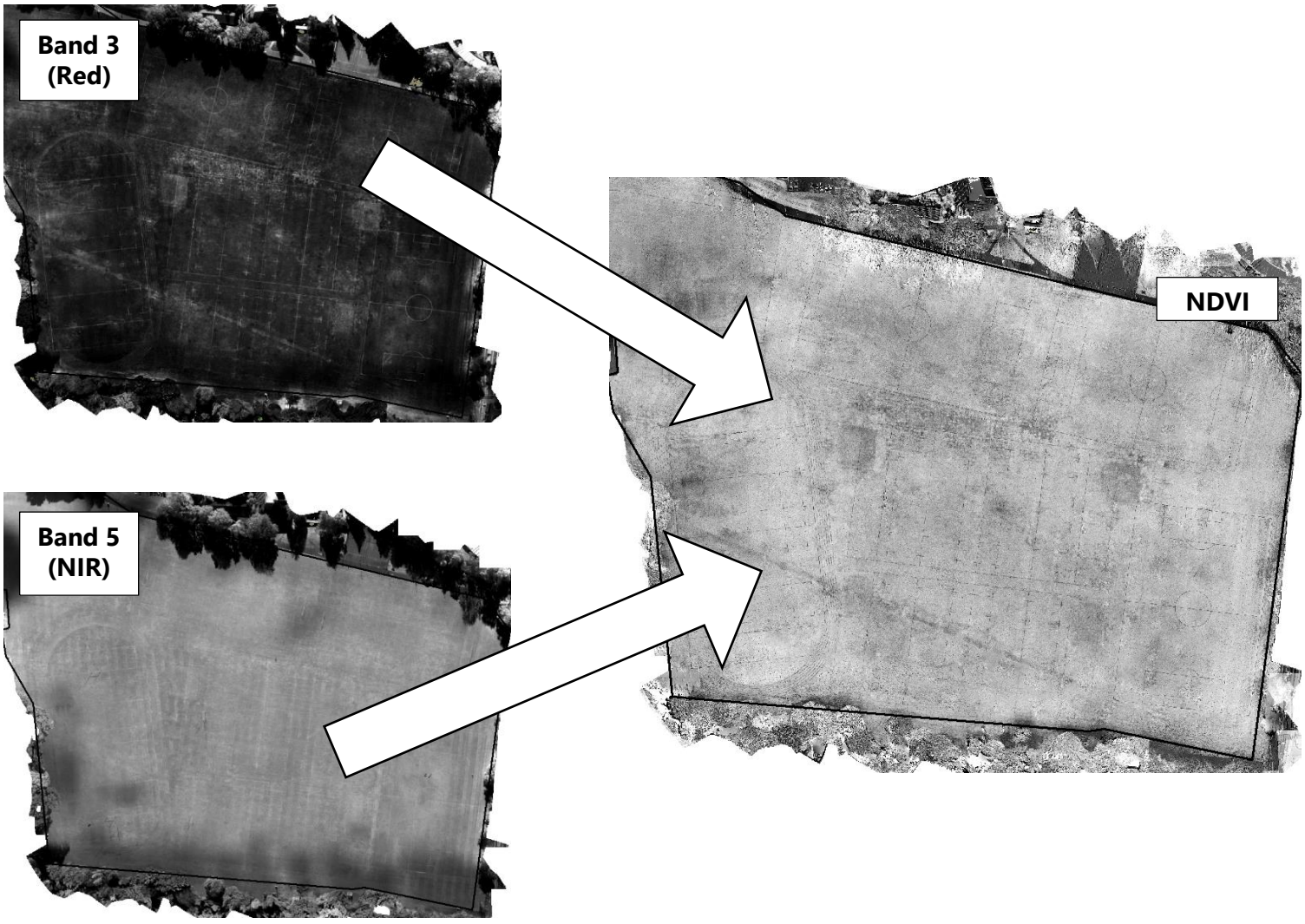

Figure 4.03: Map algebra in ArcMap with Band 3 and Band 5 producing an NDVI map

Zenmuse XT2-Thermal

The output file formats of the thermal images taken in radiometric JPEG's and SEQ (Video) files, that require proprietary software to access. In this case FLIR tools plus was used to process the images into a readable TIF format (figure 4.04).

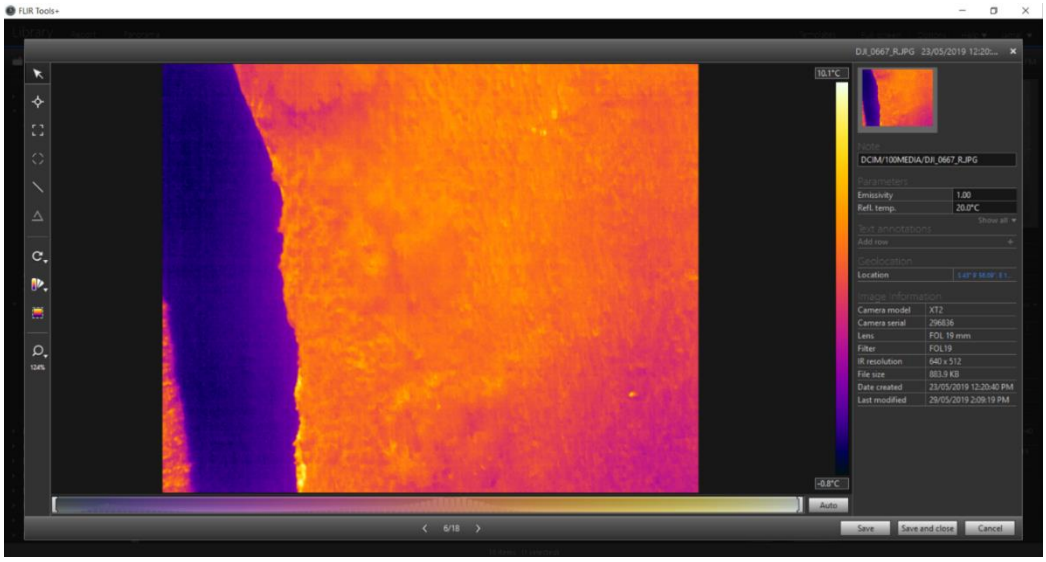

Figure 4.04: FLIR tools UI view thermal images.

As for the videos, FLIR tools does not offer a method to export the proprietary SEQ files into a more user friendly format (.MP4, .AVI etc.), so a more crude method was used, which involved using a screen cap to record the video in real-time and export the .MP4 file into Adobe Premiere Pro CC 2019. With the magic of video overlays, I was able to create videos showing both thermal and visible video synchronously (figure 4.05).

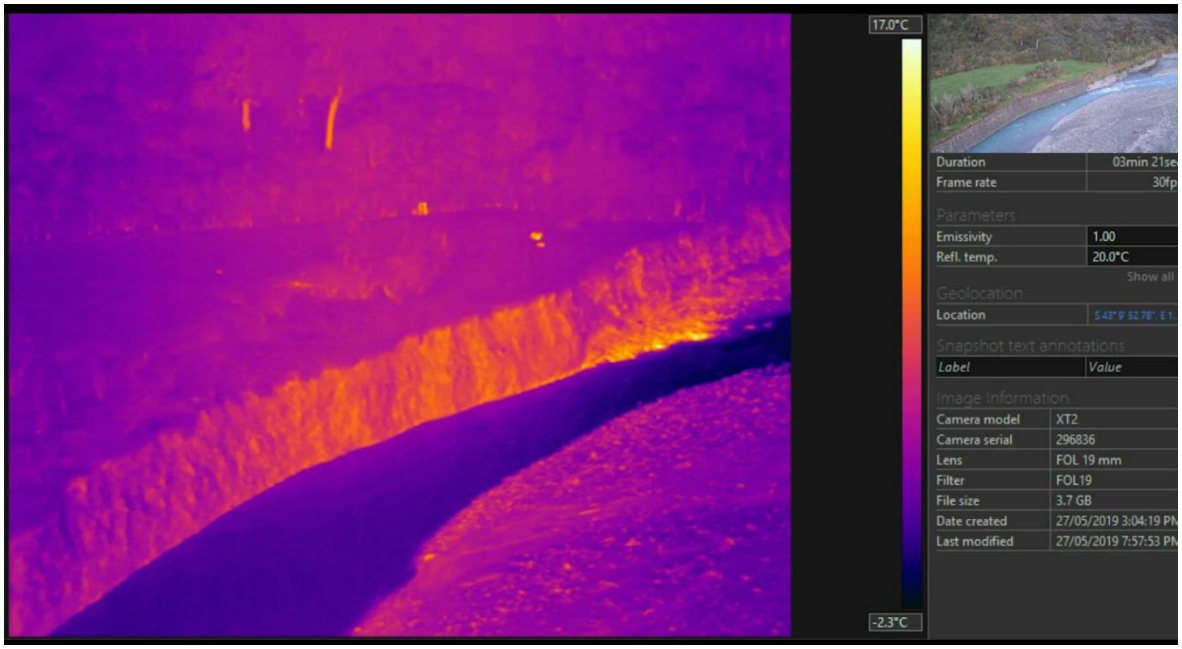

Figure 4.05: Screenshot of the video made for this research in Adobe Premier PRO 2019.

Before any soil analysis can be performed, a GNSS system must be active for field surveying (figure 4.06). First a stationary base station is placed in the middle of the paddock which will send and receive signals from the rover R8. The rovers are used to wander between points in the field.

Figure 4.06: R8 Trimble system. (Fertoing.com)

The R8 is able to record and display data in real time using RTK (Real Time Kinematic) correction (figure 4.07). This is achieved by using the rover and base station as the rover moves around collecting coordinate data, the base station receiver sends correction data to the rover (surveyor) in real time (Resource Supply LLC, 2008).

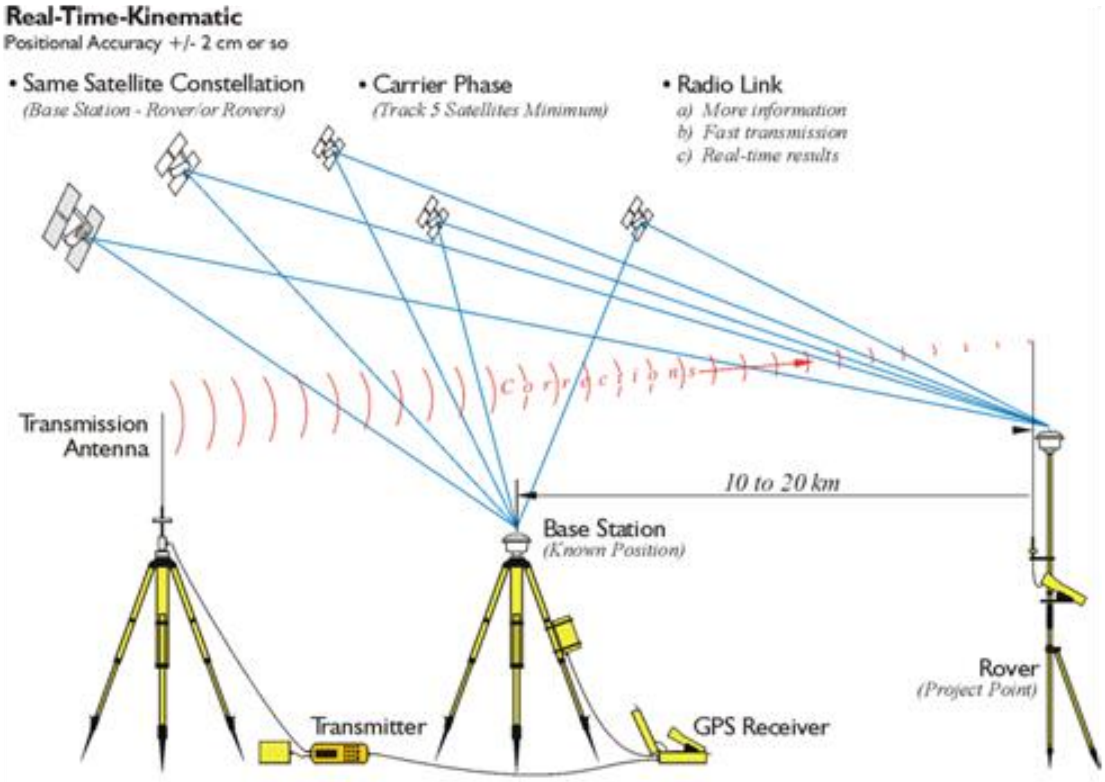

Figure 4.07: R8 Trimble RTK system set up diagram. (e-education.psu.edu).

Figure 4.08: The survey equipment set up in Ilam fields.

Originally the Trimble R8 was going to be used to record points in the field, but I decided to work backwards by creating the points in ArcMap and calculating the XY coordinates, then loading those points into the rover R, and using the rover to go from point to point.

Site	Northing	Easting
1	5181172	1565670
2	5181182	1565677
3	5181193	1565684
4	5181203	1565691
5	5181214	1565697
6	5181141	1565726
7	5181152	1565733
8	5181162	1565740
9	5181173	1565746
10	5181183	1565753
11	5181112	1565772
12	5181123	1565779
13	5181133	1565786
14	5181144	1565792
15	5181154	1565799
16	5181064	1565813
17	5181074	1565820
18	5181085	1565827
19	5181106	1565840
20	5181035	1565855
21	5181046	1565862
22	5181056	1565869
24	5181077	1565883
25	5181014	1565907

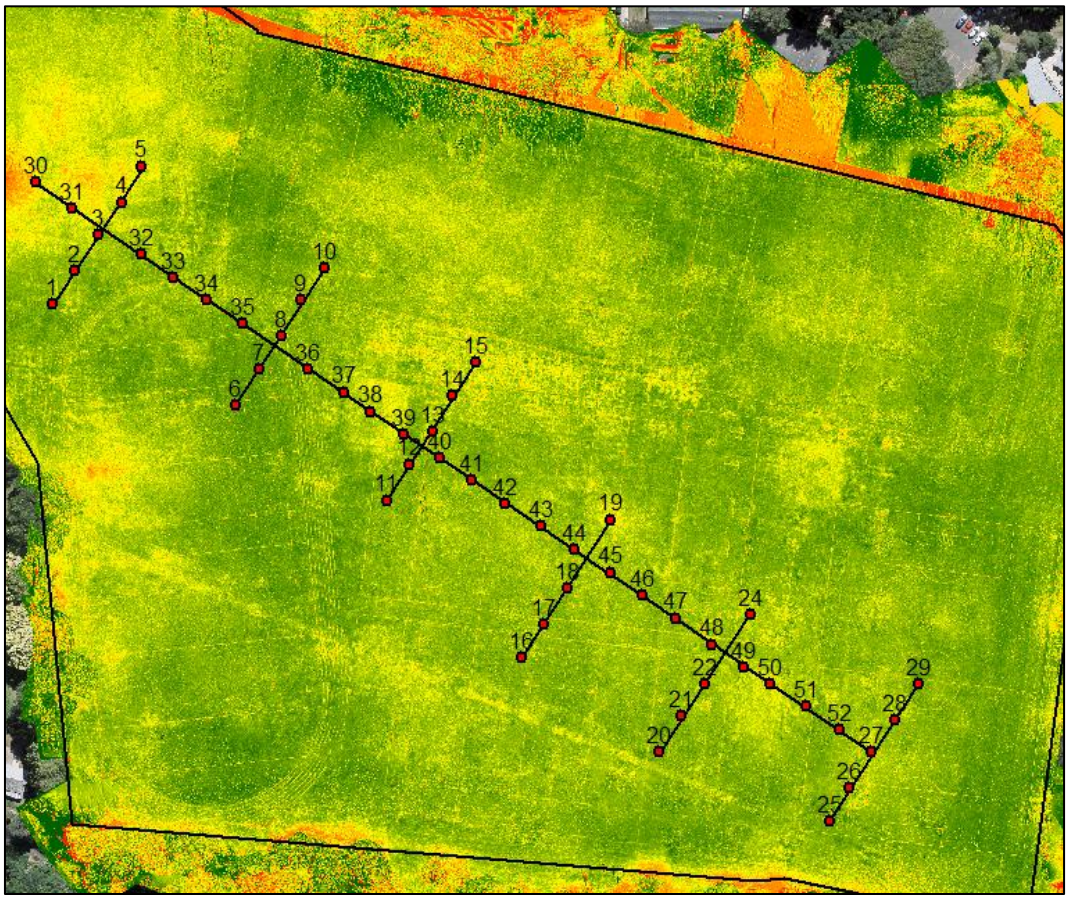

Figure 4.09: Field X Y points generated in ArcMap to be exported into Trimble R8.

Soil Analysis

Measuring CO_2 Flux

The CO_2 Li-COR LI-830 flux analyzer is placed on the ground using a good seal around the cup restricting external factors from affecting the chamber until an r value of > 0.9 is reached. The Trimble Juno handheld records, ppm, ppm/s and r^2 and can save data.

Figure 4.1: Portable CO_2 flux Analyzer Li-COR LI-830.

Calibration of the CO_2 Flux Meter

It is not clear when the University of Canterbury's WEST Systems flux meter was last calibrated. For the purposes of this thesis, the flux meter and basic training in its use was provided by University of Canterbury technical staff. No calibration was performed due to the fact that this thesis did not intend to accurately quantify the mass flux of soil gases being emitted from the ground. Rather, the primary goal of this thesis was to explore the potential utility of remote sensing methods on the identification of surface-blind geothermal discharges. Soil gas flux measurements were used to support this primary goal through the identification and comparative analysis of anomalous (i.e. relatively higher or lower) areas of soil gas emissions. This is an appropriate and rigorous approach for the specific purpose of this thesis as relatively wet areas characterized by liquid-phase geothermal discharges should have relatively low soil gas fluxes, whereas gas-phase dominated geothermal discharges should have relatively high soil gas fluxes.

For future researchers intending to quantify the mass flux of soil gas using a WEST systems flux meter, the calibration procedure is reported below. Flux Meter Calibration

from the (West Systems Handbook., 2012): CO_2 fluxes from soil are simulated by injecting a known flow of gas into the accumulation chamber. The interface between the accumulation chamber and the calibration table (fig 4.101) is built to minimize the gas leakage (West Systems Handbook., 2012). For fluxes between 0.5 and 300 moles/(m^2day) the injected flux is controlled and measured with a precision Mass Flow Controller (Fig. 4.101). This MFC, calibrated for CO_2, is electronically stabilized (Accuracy 1%) (West Systems Handbook., 2012).

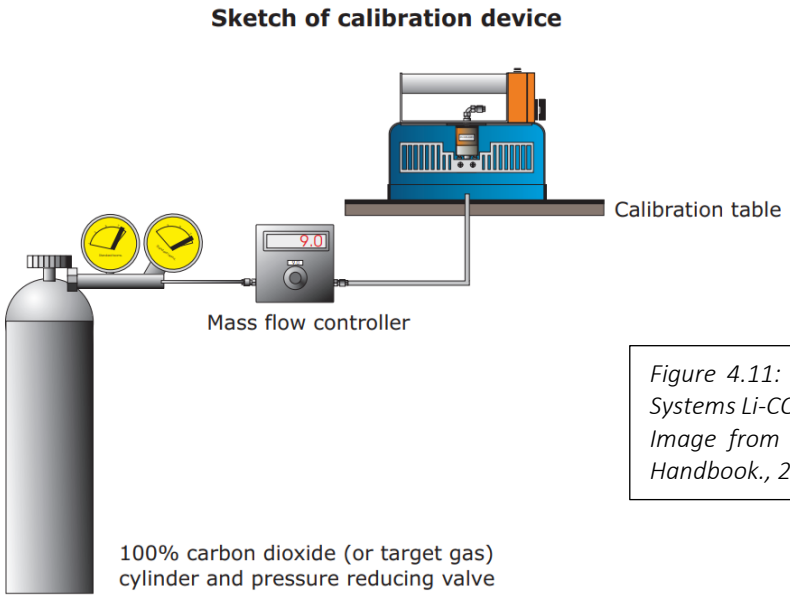

Figure 4.11: Figure shows West Systems Li-COR calibration setup. Image from the (West Systems Handbook., 2012).

For fluxes between 300 moles/(m^2day) and 700 moles/ (m^2day) the injected flux is controlled by means of a mechanical flow reducer and measured using a bubble flowmeter (Accuracy 3%) before and after the flux measurement with the accumulation chamber (West Systems Handbook., 2012).

Two series of measurements were performed for flux of 300 moles/(m^2day) to evaluate the coherence between the two different methods of flow measurement.
A thermometer and barometer were utilized to measure the barometric pressure and the air temperature during the experiment in order to select the correct accumulation chamber conversion factor (West Systems Handbook., 2012).

A flow meter is utilized to measure the pumping flow during the experiment. During all the measures a 100% CO_2 flow was utilized (West Systems Handbook., 2012). The same procedure was utilized to check the instrumental response to methane / Hydrogen Sulphide.

Magnesium Perchlorate ($Mg(ClO_4)_2$) was used to trap moisture in the tube from the gas stream in the field.

Soil Temperature

The Sinsui dual input thermometer supports two output probes, one 20 cm long and the other 50 cm to measure the soil temperature. Two holes must be drilled into the ground at each site using the Dynamic Cone Penetration (DCP). With the Sinsui Dual Input K-Type thermometer the sensor is only active at the very tip of the probe, so the probe tip is held firmly inside the soil matter to measure soil temperature and not air temperature.

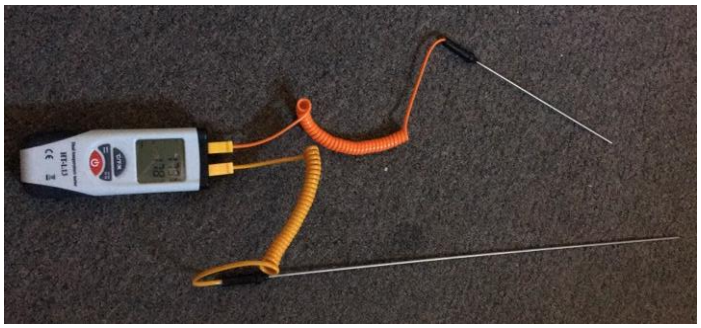

Figure 4.12: Sinsui dual input K-Type Soil temperature probes.

Dynamic Cone Penetration (DCP)

Following the soil gas flux measurements, holes are drilled in using the DCP in exactly the same spots as where the soil CO_2 flux measurements were taken. The 9kg weight (drop hammer) is lifted and dropped where it hits the 'anvil' subsequently pushing the driving rod through the soil. This is done twice, one 20 cm deep and then 50 cm deep.

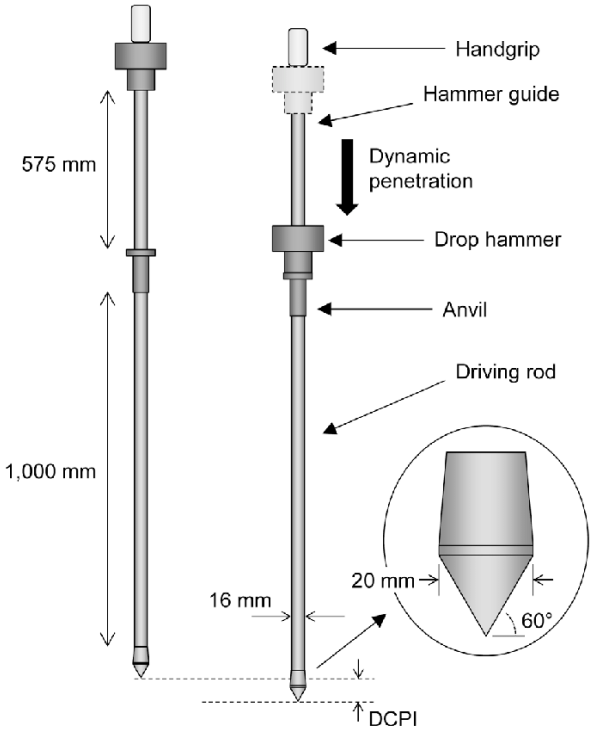

Figure 4.13: Image of the DCP used to drill the hole into the ground for soil temperature sampling (Won-Taek & Kang et., al. 2016).

Field Plan

Along the transit tape CO_2 flux, two holes made using the DCP at 12.5m intervals defined by premade map (figure 4.13). After every temperature probe use, a cloth is used to clean it and then used in the next hole.

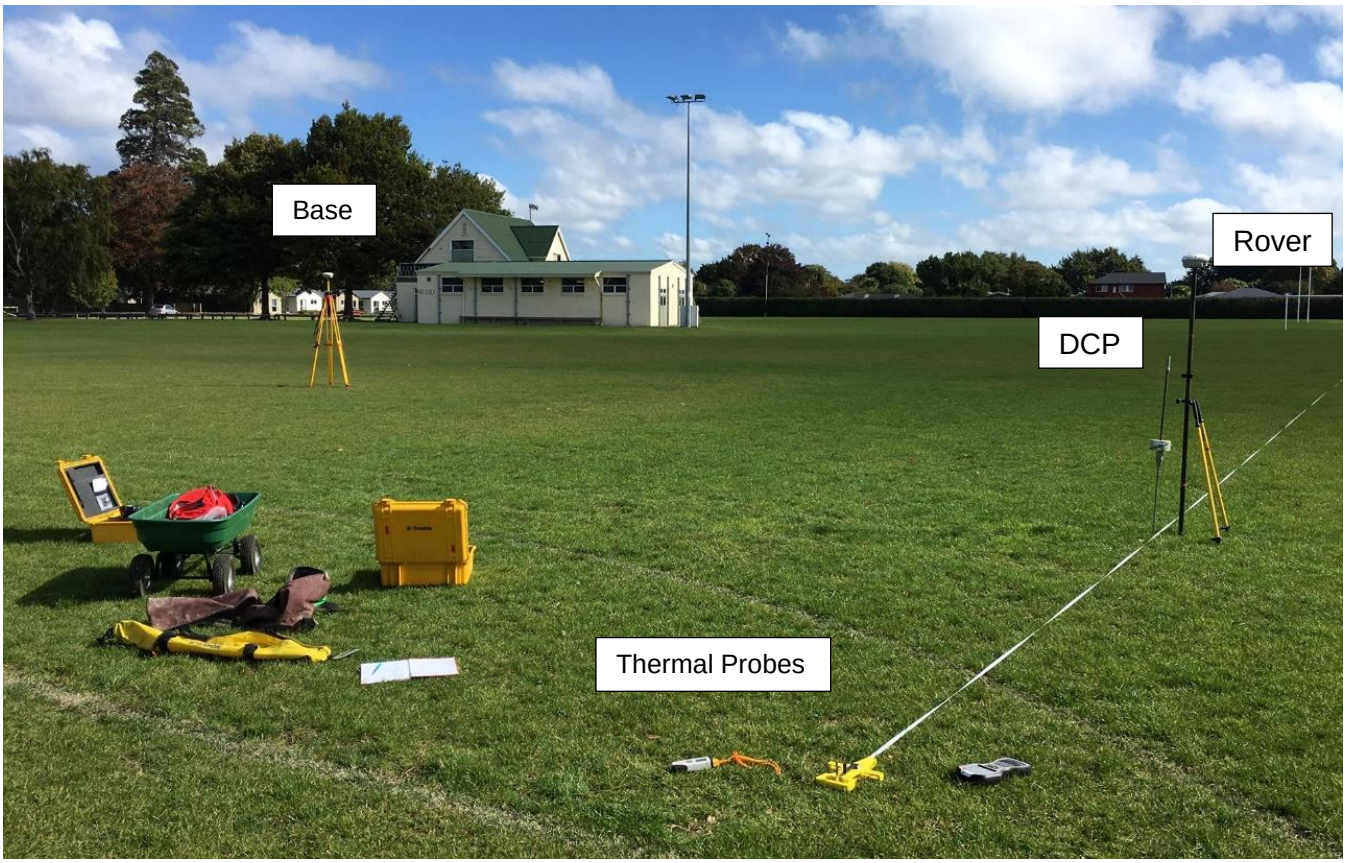

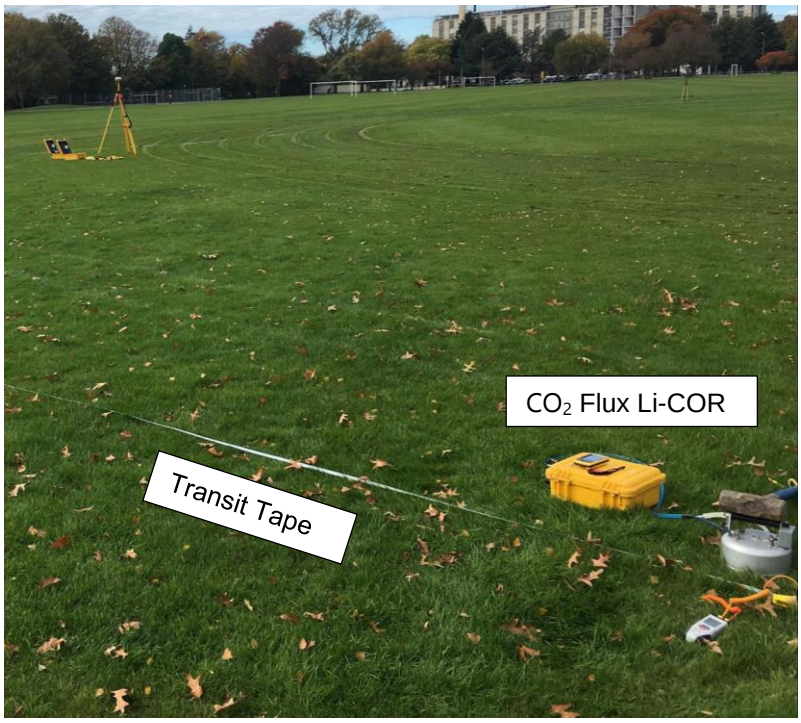

Figure 4.14: (Above and Left) Photo of field setup in Ilam Fields with Transit tape, Trolley, Rover, Base, DCP, Thermal probes and Flux LI-COR.

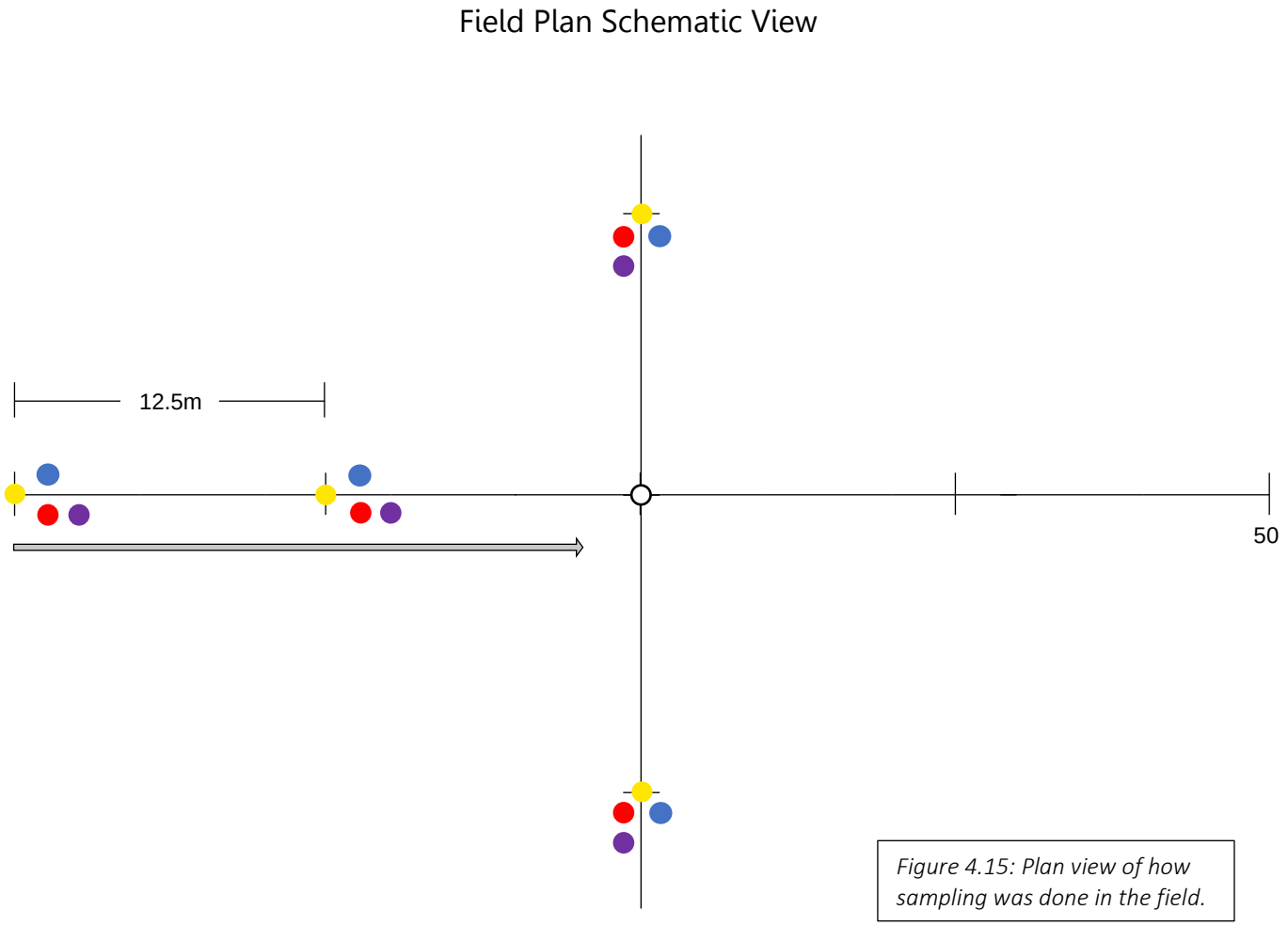

Figure 4.15: Plan view of how sampling was done in the field.

Figure 4.16: Panoramic image of Harihari field site, featuring thesis supervisor, Travis Horton.

Developing The Analytical Model

At the time of assessing the data for analysis the geospatial analytical program ENVI was not available so an alternative more complicated method was used. The data was put through ENVI near the end of the thesis submission and delivered the same results.

In order to analyse the raw field data into something more useful a series of steps must be taken to synthesize the field data. Starting with image processing (as previously explained) the images are aligned in an orthomosaic in Agisoft and then map algebra is performed to turn the multiple inputs into an NDVI map. Once this is done, the field points are attributed the field data (CO_2 flux and Soil temperature 20 and 50 cm) through table join data. Kriging analysis is then performed to interpolate data across an area.

The steps taken is as follows:

A – Outline the field area (field extent)

B - Kriging analysis

This is used to create a data map that will interpolate data based on sample points using the formula:

$$\hat{Z}(s_0) = \sum_{i=1}^{N} \lambda_i Z(s_i)$$

where:

$Z(s_i)$ = the measured value at the *ith* location

λ_i = an unknown weight for the measured value at the *ith* location

S_0 = the prediction location

N = the number of measured values

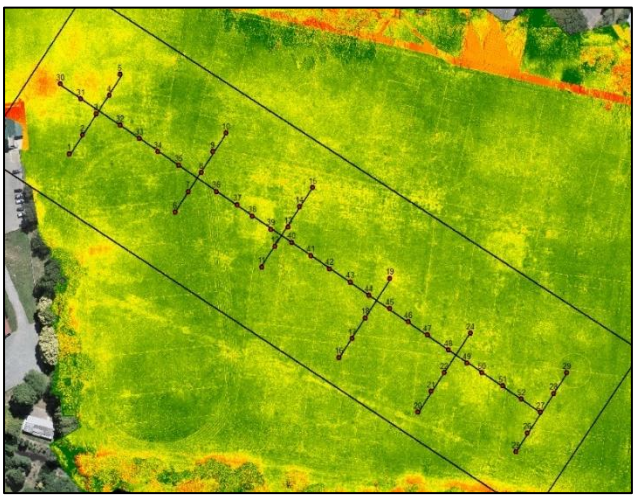

Figure 4.17: Image of Ilam Field data in ArcMap.

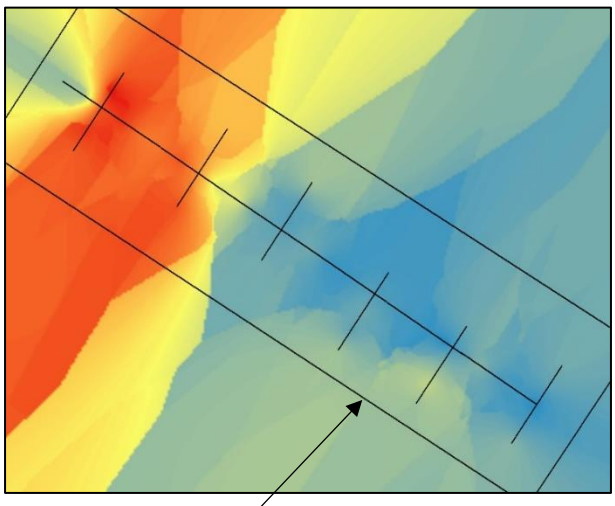

Figure 4.18: Field extent.

C – Fishnet

The function will create points in a grid over the data maps.

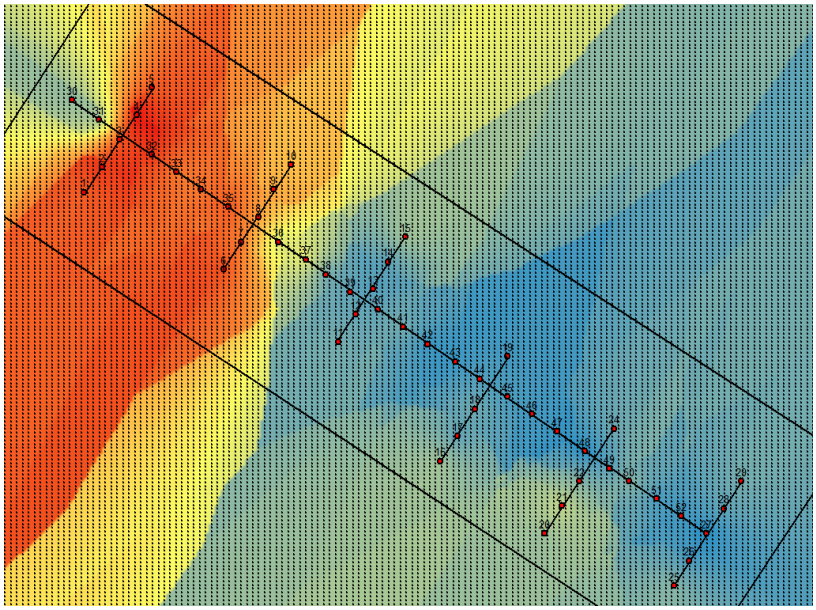

Figure 4.19: Fishnet cast over the full data set

D – Filter

The irregular angle of the rectangular field extent makes it tedious to remove the points out of bounds and so the surplus points must be removed to increase accuracy in subsequent analysis.

There are multiple ways to do this, but I used a polygon to cover the areas outside the study site and gave that polygon a field value 50 (can be any number), then convert that polygon into a raster that displays the value of 50. Extract values to points, so the points with the value of 50 are flagged as outside the field extent.

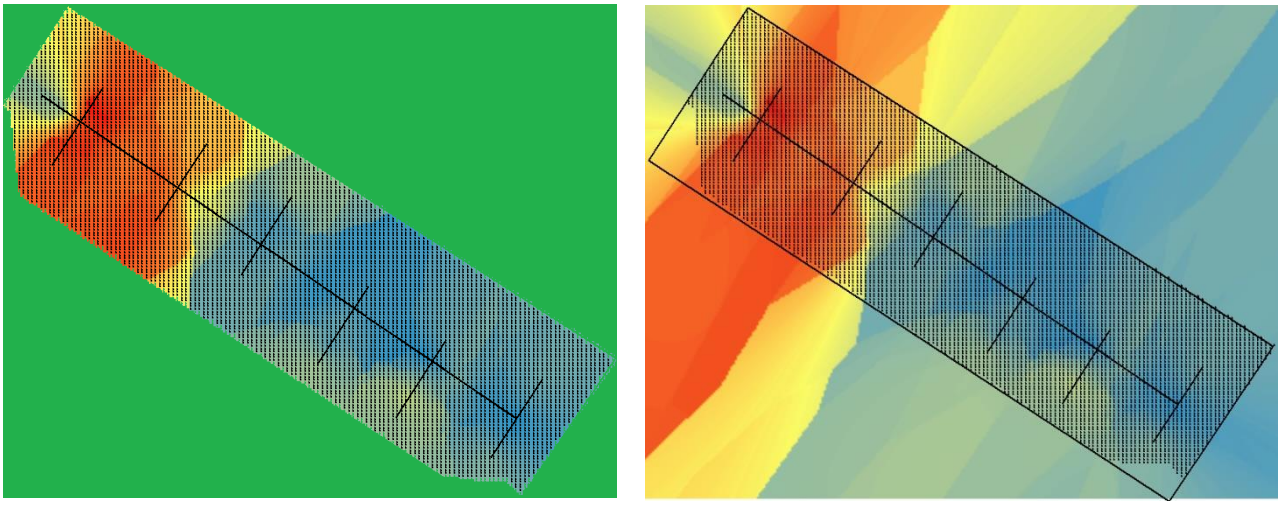

Figure 4.2: The use of a polygon filter, used to take out points away from the field extent

E - Extract multi values to Points

The raster values are extracted to the filtered points so each point has a value in the following fields: NDVI, CO_2 flux (ppm/s), Soil temperature 20 cm, Soil temperature 50 cm, Surface temperature and the filter value of 50. Only the points with the filter value of 50.

F - Table to Excel

The attribute table is extracted into an excel spread sheet.

Site	Northing	Easting	Vertical	ppm	ppm/s	r2	ST20	ST50	NDVI	Surface Temperature
1	5181172	1565670	27	400	0.45	0.945	13.5	13.8	0.606	9.6
2	5181182	1565677	27	398	0.454	0.912	13.5	13.8	0.503	10.2
3	5181193	1565684	27	385	0.375	0.996	13.3	13.9	0.311	9.7
4	5181203	1565691	27	386	0.36	0.966	12.1	13.3	0.329	10.6
5	5181214	1565697	27	387	0.345	0.935	12.7	13.5	0.144	9.6
6	5181141	1565726	27	405	0.486	0.935	14.2	15.6	0.564	9.8
7	5181152	1565733	27	393	0.512	0.943	13.9	15.6	0.517	9.1
8	5181162	1565740	27	405	0.556	0.962	14.2	15.2	0.548	8.5
9	5181173	1565746	27	416	0.6	0.98	13.9	15.3	0.555	8.3
10	5181183	1565753	27	415	0.6	0.977	14.3	15.3	0.282	8
11	5181112	1565772	27	414	0.599	0.974	16.9	17.9	0.508	4.5
12	5181123	1565779	27	397	0.571	0.98	15.6	16.6	0.431	4.3
13	5181133	1565786	27	380	0.543	0.985	14.5	12.8	0.325	4
14	5181144	1565792	27	390	0.604	0.988	15	15.2	0.016	4.1
15	5181154	1565799	27	400	0.664	0.99	15.4	16.2	0.397	5.3
16	5181064	1565813	27	355	0.17	0.575	13.7	15.1	0.424	5.3
17	5181074	1565820	27	363	0.23	0.742	14.1	14.9	0.326	4.2
18	5181085	1565827	27	370	0.29	0.909	15.7	16.6	0.493	4.4
19	5181106	1565840	27	385	0.753	0.952	16.8	15.6	0.066	3.8
20	5181035	1565855	27	400	1.216	0.995	15.2	16.6	0.483	5.2

	A	B	C	D	E	F
1	CO2 ppm	CO2 Flux	ST50	ST20	Surface Temp	NDVI
2	401	0.466	14.40	13.78	9.66	0.370
3	400	0.477	15.00	13.84	9.76	0.369
4	400	0.478	15.00	13.85	9.76	0.226
5	400	0.478	15.00	13.86	9.76	0.335
6	403	0.503	15.50	14.02	9.70	0.376
7	403	0.503	15.50	14.02	9.71	0.531
8	412	0.590	15.57	14.20	9.87	0.439
9	412	0.588	15.57	14.20	9.86	0.478
10	412	0.586	15.57	14.20	9.86	0.254
11	412	0.584	15.57	14.20	9.85	0.468
12	412	0.582	15.57	14.19	9.85	0.334
13	412	0.580	15.57	14.19	9.84	0.399
14	412	0.577	15.57	14.19	9.84	0.563
15	411	0.575	15.57	14.19	9.83	0.522

Figure 4.21: (Above) Raw field data embedded in the sample points with raw field data formatted in Excel

G - Excel to CSV

The newly created excel spread sheet is reformatted with new labels and removing fields such as object ID, shape type and filter leaving only NDVI, CO_2 flux (ppm/s), Soil temperature 20 cm, Soil temperature 50 cm and Surface Temp. Then is converted into CSV (comma separated variable) file format (figure 4.22).

Ilam Sample Points - Notepad

File Edit Format View Help

```
CO2 ppm,CO2 Flux,ST20,ST50,Surface Temp,NDVI
401,0.466,13.78,14.40,9.66,0.370
400,0.477,13.84,15.00,9.76,0.369
400,0.478,13.85,15.00,9.76,0.226
400,0.478,13.86,15.00,9.76,0.335
403,0.503,14.02,15.50,9.70,0.376
403,0.503,14.02,15.50,9.71,0.531
412,0.590,14.20,15.57,9.87,0.439
412,0.588,14.20,15.57,9.86,0.478
412,0.586,14.20,15.57,9.86,0.254
412,0.584,14.20,15.57,9.85,0.468
412,0.582,14.19,15.57,9.85,0.334
412,0.580,14.19,15.57,9.84,0.399
412,0.577,14.19,15.57,9.84,0.563
411,0.575,14.19,15.57,9.83,0.522
411,0.573,14.19,15.57,9.83,0.574
408,0.546,14.03,15.60,9.72,0.584
408,0.547,14.03,15.60,9.65,0.354
408,0.549,14.03,15.60,9.55,0.222
408,0.552,14.02,15.60,9.41,0.664
408,0.555,14.02,15.60,9.24,0.669
408,0.560,14.02,15.60,9.05,0.590
409,0.564,14.01,15.60,8.84,0.475
409,0.568,14.01,15.60,8.62,0.589
409,0.573,14.01,15.60,8.40,0.480
416,0.594,13.75,14.83,8.10,0.609
416,0.597,13.73,14.83,7.89,0.672
417,0.639,13.73,14.47,5.90,0.512
417,0.637,13.73,14.47,5.82,0.422
417,0.635,13.73,14.47,5.73,0.588
417,0.632,13.74,14.47,5.61,0.339
417,0.631,13.74,14.47,5.53,0.531
407,0.585,13.44,14.20,5.31,0.505
407,0.585,13.45,14.20,5.09,0.433
407,0.584,13.45,14.20,4.85,0.350
```

Figure 4.22: Field data in CSV format

Python Data Analysis Script Break Down

The software library known as pandas written by Wes McKinney in 2008 was used as the preferred method to perform statistical analysis in python because of the simplicity and wealth of available methods that the pandas library offers.

(note that only the green text represents actual code and the purple text will attempt to explain the key methods used)

H - CSV into Python

> Import the required packages used for reading .csv, pandas the statistical library and numeric python the mathematical python library

```
import csv
import pandas as pd
import numpy as np
```

> Adjust the pandas data frame output

```
pd.set_option('display.height', 1000)
pd.set_option('display.max_rows', 500)
pd.set_option('display.max_columns', 500)
pd.set_option('display.width', 1000)
```

> Function is set on auto-run on execute, self runs the uploaded csv into the definition, where the delimiter is set as a comma ',' this is done so pandas knows where to split each cell

```
if __name__ == "__main__":
    def Hari (self):
        with open(self):
            Hari = pd.read_csv(self, delimiter=',')
            HDF = pd.DataFrame(Hari, columns=(['NDVI','Surface Temp','CO2 Flux','CO2
ppm','ST20','ST50']))
```

> Describe method is used display the mean, std, min, 25%, 50%, 75%, max and count of all the values in the data frame. This is especially useful when you have well over 1,000 values. Count refers to the number of rows not cells.

```
HD = HDF.describe()
HD = round(HD, 3)
Print(HD)
```

	NDVI	Surface Temp	CO2 Flux	CO2 ppm	ST20	ST50
count	9633.000	9633.000	9633.000	9633.000	9633.000	9633.000
mean	0.382	5.708	0.808	479.735	12.211	13.215
std	0.189	0.467	0.386	21.765	0.356	0.453
min	-0.579	4.200	0.148	422.000	11.360	12.400
25%	0.276	5.430	0.548	464.000	11.980	12.770
50%	0.402	5.830	0.683	482.000	12.220	13.160
75%	0.508	6.030	1.037	496.000	12.450	13.500
max	0.929	6.370	2.018	543.000	13.150	14.460

Figure 4.23: Data output in Python

> Creating 4 filters based on the quartile ranges of NDVI. This will separate all values into 4 groups

```
I = HDF[(HDF['NDVI'] >= -0.579) and (HDF['NDVI'] <= 0.2759)]
II = HDF[(HDF['NDVI'] >= 0.276) and (HDF['NDVI'] <= 0.4019)]
III = HDF[(HDF['NDVI'] >= 0.402) and (HDF['NDVI'] <= 0.5079)]
IV = HDF[(HDF['NDVI'] >= 0.508) and (HDF['NDVI'] <= 0.929)]
```

I - Python back to CSV

> The 4 groups are analysed further again and rounded by 3 decimal places

```
F1 = I.describe()
F1 = round(F1, 3)
F2 = II.describe()
F2 = round(F2, 3)
F3 = III.describe()
F3 = round(F3, 3)
```

```
F4 = IV.describe()
F4 = round(F4, 3)
```

> Open method is used to create an output file and write is used to write the data as strings in the csv file. Close method gives the computer back it's memory.

```
IA = open('HariHariResult.csv', 'w+')
IA.write(str(F1))
IA.write(str(F2))
IA.write(str(F3))
IA.write(str(F4))
IA.write(str(HD))
IA.close()
```

J - CSV to Excel to be Refined

The product of the pandas code is taken back into excel and reformatted again and transposed to switch the X / Y axis.

NDVI Range I	-0.439 - 0.3689 [Min - Low]						
Stats	CO2 ppm	CO2 Flux	ST20	ST50	Surface Temp	NDVI	count
mean	401.37	0.571	14.217	14.744	6.119	0.241	2402
std	18.31	0.195	0.914	0.94	2.073	0.119	
min	362	0.213	12.66	11.93	3.52	-0.439	
25%	391	0.387	13.46	14.1	4.36	0.188	
50%	395	0.591	14.15	14.73	5.25	0.277	
75%	407	0.668	14.97	15.53	7.89	0.328	
max	472	1.147	16.62	16.5	10.54	0.368	

Figure 4.24: (Above) Formatted CSV field data into excel
Figure 4.25: (Below) Reformatted and transposed axis' (X and Y switched) data in Excel

NDVI Range I	**-0.439 - 0.3689 [Min - Low]**						
Stats	Mean	Std	Min	25%	50%	75%	Max
CO2 ppm	401	18	362	391	395	407	472
CO2 Flux	0.571	0.195	0.213	0.387	0.591	0.668	1.147
ST20	14.22	0.91	12.66	13.46	14.15	14.97	16.62
ST50	14.74	0.94	11.93	14.10	14.73	15.53	16.50
Surface Temp	6.12	2.07	3.52	4.36	5.25	7.89	10.54
NDVI	0.241	0.119	-0.439	0.188	0.277	0.328	0.368
Count	2402						

Multispectral Satellite Imagery and Script Walkthrough

Using Planet.com imagery and python scripting to calculate pixel NDVI and the subsequent reflectance values:

Download a four-band image from Planet.com

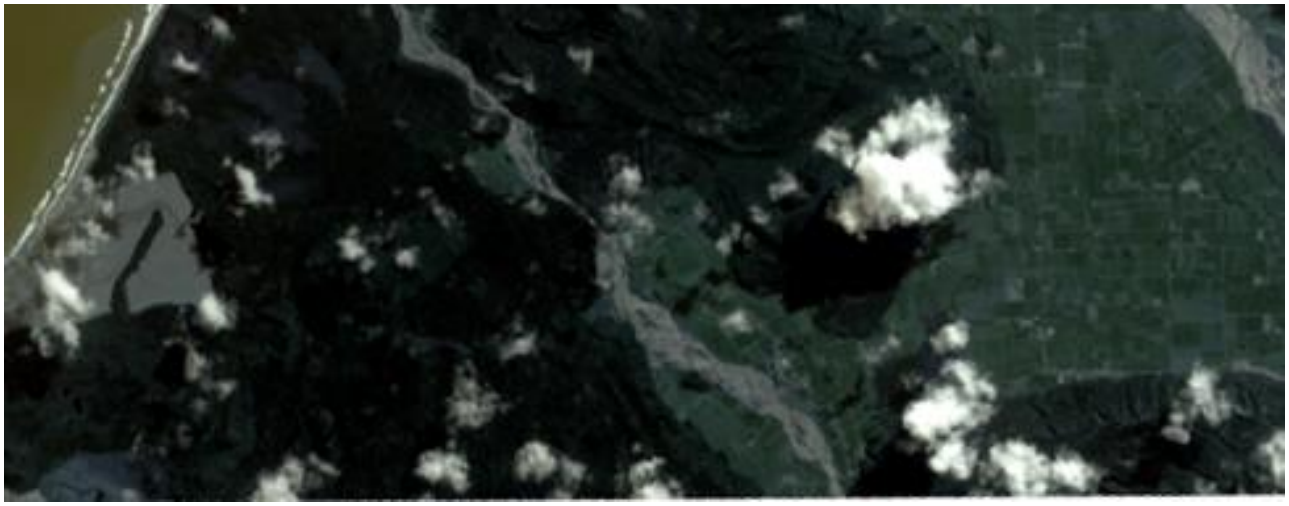

Figure 4.26: Multispectral image of a regional view over Harihari (West Coast) taken from planet.com aerial photos

Load the downloaded image (from Planet.com) into Python and Extract the visible red and NIR bands

(Please note that only the green text represents actual code and the purple text will attempt to explain the key methods used for atmospheric calibrations and NDVI calculations)

>Import the required libraries to complete the calculation of NDVI, rasterio, numpy (Number Python) as np for short and xml.dom (XML document parser).

```
import rasterio
import numpy as np
import xml.dom


if __name__ == '__main__':
def NDVI(self):
        image_file_test = (self)
```

> Load red and NIR bands-Planetscope 4-bands are ordered BGRN:

```
    with rasterio.open(image_file_test) as src:
            band_red = src.read(3)
    with rasterio.open(image_file_test) as scr:
                    band_nir = scr.read(4)
```

Radiometric corrections

> Radiometric corrections: Normalize to Top Of Atmosphere Reflectance:

```
from xml.dom import minidom
xmldoc = minidom.parse('test_ms_md.xml')
nodes = xmldoc.getElementsByTagName('ps:bandSpecifi cmetadata')
```

This set of code coverts pixel values to Top Of Atmosphere Reflectance which makes analysis more accurate and can be compared more fairly with other scenes.
TOA Reflectance coefficients are loaded in from the XML metadata sheet.

> Separate the bands by numbers 1-4 into parsable units as specified in the XML metadata file:

```
coeffs = {}
    for node in nodes:
        bn = node.getElementsByTagName("ps:bandNumber")[0].firstChild.data
        if bn in ['1', '2', '3', '4']:
            i = int(bn)
            value =
node.getElementsByTagName("ps:reflectanceCoefficient")[0].firstChild.data
            coeffs[i] = float(value)
```

> Multiply the band values by the corresponding TOA Reflectance coefficients:

```
band_red1 = band_red * coeffs[3]
band_nir1 = band_nir * coeffs[4]
```

> Perform the NDVI calculation:

The input files are in TIFF format (raster) each pixel has a designated value, NDVI calculation needs to be able to analyse each pixel value through subtraction and division (see NDVI calculation formula).

The number python (np) library does NDVI calculations, in cases where the code meets a mathematical error i.e. having to divide by zero and resulting in the code crashing mid calculation, the code must allow division by zero so we tell it to ignore this error.

```
np.seterr(divide='ignore', invalid='ignore')
```

> Calculate NDVI:

```
ndvi = (band_nir.astype(float)-band_red.astype(float)) / (band_nir + band_red)
```

> Produce output NDVI image in TIFF format so that it can be later used in other mapping software such as arcMap. The new file will have calibrated band-4 (NIR) pixel values, and will be adjusted to mirror the GeoTIFF spatial metadata provided by Planet.com.

> Set spatial characteristics of the output object to mirror the input:

```
kwargs = src.meta
kwargs.update(
   dtype=rasterio.float32,
   count = 1)
```

> Create the output file called ‘NDVI’ with the file extension .tif and ‘w’ means to create and write the data to a file named ‘NDVI.tif’ and **kwargs to take an arbitrary number of KeyWord ARGuments:

```
with rasterio.open('NDVI.tif', 'w', **kwargs) as dst:
    dst.write_band(1, ndvi.astype(rasterio.float32))
```

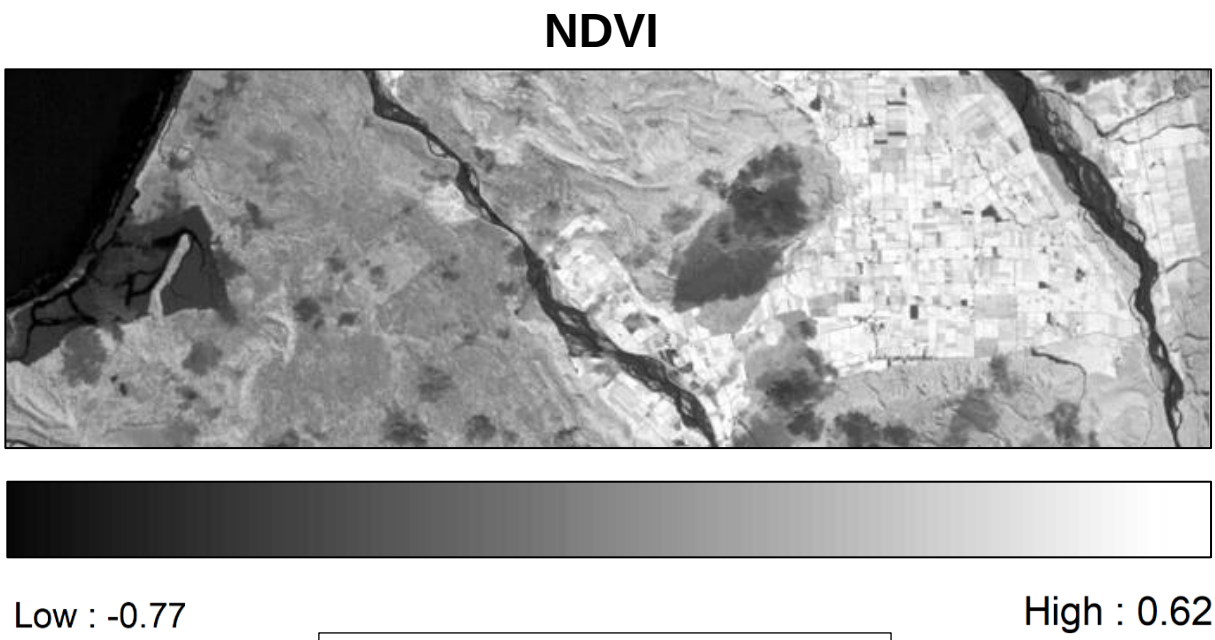

Figure 4.27: Product of NDVI calculation in Python

> Now That the NDVI raster file has been made we will benefit from taking that same newly created NDVI.tif file and performing another calculation in creating a reflectance map to see where the most energy reflection is occurring.

> This method splits each band into its own object which is later used separately 1: Blue, 2: Green, 3: Red, 4: Near Infrared (NIR).

```
with rasterio.open(image_file_test) as src2:
        band_blue_radiance = src2.read(1)
with rasterio.open(image_file_test) as src2:
        band_green_radiance = src2.read(2)
with rasterio.open(image_file_test) as src2:
        band_red_radiance = src2.read(3)
with rasterio.open(image_file_test) as src2:
        band_nir_radiance = src2.read(4)
```

> Extract the Coefficients, before conversion to reflectance can be done the coefficients must be extracted from the same XML file as above. Separate the bands by numbers 1-4 into parsable units as specified in the XML metadata file:

```
coeffs = {}
        for node in nodes:
            bn = node.getElementsByTagName("ps:bandNumber")[0].firstChild.data
            if bn in ['1', '2', '3', '4']:
                i = int(bn)
                value =
node.getElementsByTagName("ps:reflectanceCoefficient")[0].firstChild.data
                coeffs[i] = float(value)
print("Conversion coefficients:" , coeffs)
```

The Conversion coefficients:

Coeffs[1]: 1.92992290459e-05

Coeffs[2]: 2.0401521894e-05

Coeffs[3]: 2.2723104298e-05

Coeffs[4]: 3.35095412863e-05

> Convert Radiance to Reflectance:

The conversion is performed as a simple per-band scalar multiplication: Radiance is measured in SI units: W/m^2. Reflectance is a ratio from 0 to 1.

> Multiply the Digital Number (DN) values in each band by the TOA reflectance coefficients:

```
        band_blue_reflectance = band_blue_radiance * coeffs[1]
        band_green_reflectance = band_green_radiance * coeffs[2]
        band_red_reflectance = band_red_radiance * coeffs[3]
        band_nir_reflectance = band_nir_radiance * coeffs[4]
```

```
        print ("Red band radiance is from {} to {}".format(np.amin(band_red_radiance),
np.amax(band_red_radiance)))

        print ("Red band reflectance is from {} to
{}".format(np.amin(band_red_reflectance), np.amax(band_red_reflectance)))
```

> Set spatial characteristics of the output object to mirror the input

```
        kwargs = src.meta
        kwargs.update(
            dtype=rasterio.uint16,
            count = 4)

        print ("Before Scaling, red band reflectance is from {} to
{}".format(np.amin(band_red_reflectance), np.amax(band_red_reflectance)))
```

> Included is a fixed scaling factor that adjusts output image:

```
        scale = 10000
        blue_ref_scaled = scale * band_blue_reflectance
        green_ref_scaled = scale * band_green_reflectance
        red_ref_scaled = scale * band_red_reflectance
        nir_ref_scaled = scale * band_nir_reflectance

        print ("After Scaling, red band reflectance is from {} to
{}".format(np.amin(red_ref_scaled), np.amax(red_ref_scaled)))
```

> Write band calculations to a new raster file

```
with rasterio.open('Reflectance.tif', 'w', **kwargs) as dst:
        dst.write_band(1, band_blue_reflectance.astype(rasterio.uint16))
        dst.write_band(2, band_green_reflectance.astype(rasterio.uint16))
        dst.write_band(3, band_red_reflectance.astype(rasterio.uint16))
        dst.write_band(4, band_nir_reflectance.astype(rasterio.uint16))
```

> Before Scaling, red band reflectance is from 0.0 to 0.568986531622

> After Scaling, red band reflectance is from 0.0 to 5689.86531622

> Apply a Color Scheme to Visualize the Reflectance Values on the Image:

```
class MidpointNormalize(colors.Normalize):
    def __init__(self, vmin=None, vmax=None, midpoint=None, clip=False):
        self.midpoint = midpoint
        colors.Normalize.__init__(self, vmin, vmax, clip)

    def __call__(self, value, clip=None):
        x, y = [self.vmin, self.midpoint, self.vmax], [0, 0.5, 1]
        return np.ma.masked_array(np.interp(value, x, y), np.isnan(value))
```

> Set min/max values from reflectance range for image (excluding NAN)

```
min=np.nanmin(band_nir_reflectance)
max=np.nanmax(band_nir_reflectance)
mid=0.20
fig = plt.figure(figsize=(20,10))
ax = fig.add_subplot(111)
```

```
        cmap = plt. cm.get_ cmap('RdGy_r')

cax = ax.imshow(band_nir_reflectance,  cmap= cmap, clim=(min, max),
norm=MidpointNormalize(midpoint=mid,vmin=min, vmax=max))

        ax.axis('off')
        ax.set_title('NIR Reflectance', fontsize=18, fontweight='bold')


        cbar= fig.colorbar(cax, orientation='horizontal', shrink=0.65)


        fig.savefig("ref-fig.png", dpi=200, bbox_inches='tight', pad_inches=0.7)
```

> Show reflectance map

```
        plt.show()
```

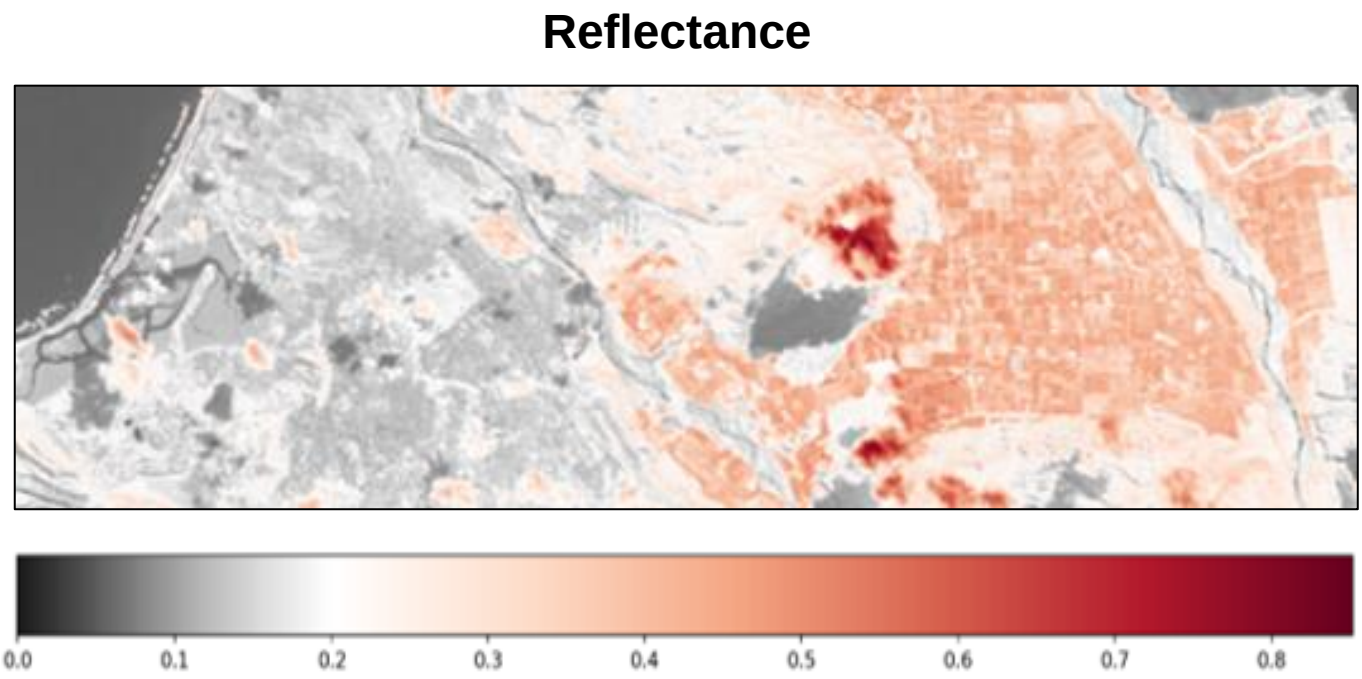

Figure 4.28: Reflectance map shows vegetation reflecting NIR back 0 = Absorbed, 1 = Full Reflection

Credit goes to the Planet Team for giving me the resources to put this code together. Planet Application Program Interface: In Space for Life on Earth. San Francisco, CA.

V. RESULTS

The NDVI data does a great job displaying the variation of plant health within Ilam and Harihari found in figure 5.01; figure 5.03; figure 5.19. On average Harihari displayed consistently higher values than compared to Ilam fields. This is most likely due to the wetter climate that exists on the West Coast as opposed to Ilam which is drier. Ilam fields and the Harihari field site were sampled within a week span under similar weather conditions. The field sampling involved measuring soil temperature at 20 cm and 50 cm deep and CO_2 flux along with the aerial spectral surveys of Infrared/NDVI (Micasense) and thermal (Zenmuse XT2).

In Ilam fields the data does appear to follow a gradual trend, CO_2 flux, Soil temperature 20 and 50 cm increase as NDVI Increases, however surface temperature does not follow suit. The results in Harihari displays similar trends where as NDVI increased so did the values of CO_2 flux and soil temperature at 20 cm, however soil temperature at 50 cm does not seem to be change very much. In Ilam there is no overlap with highest points of soil temperature and CO_2 flux. However in Harihari there are two locations that have of soil and surface temperature and CO_2 flux which suggest geothermal activity present.

Ilam Fields Observations

The vegetation was made up of mostly bladed grass (~3 cm long). The Ilam fields are managed for the use of recreational activities; rugby, football, athletics and also for research (figure 5.0). The sampling was conducted by myself and Du Chen through one 350m long transect with six 50m transects at selected locations. Sampling was done consistent with Harihari.

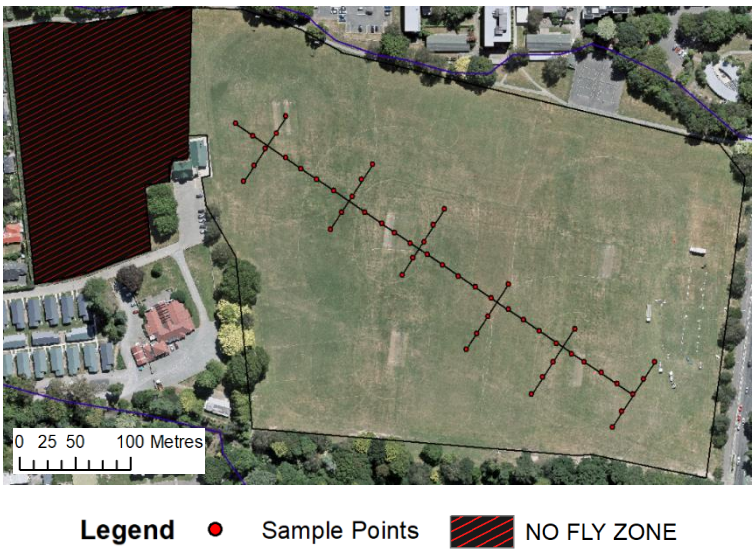

Figure 5.0: Overview of Ilam field study site.

NDVI

The overall NDVI distribution is show in the map below along with the exact points that were sampled. No fly zone is a band of UAVs within 5km of the Christchurch Airport.

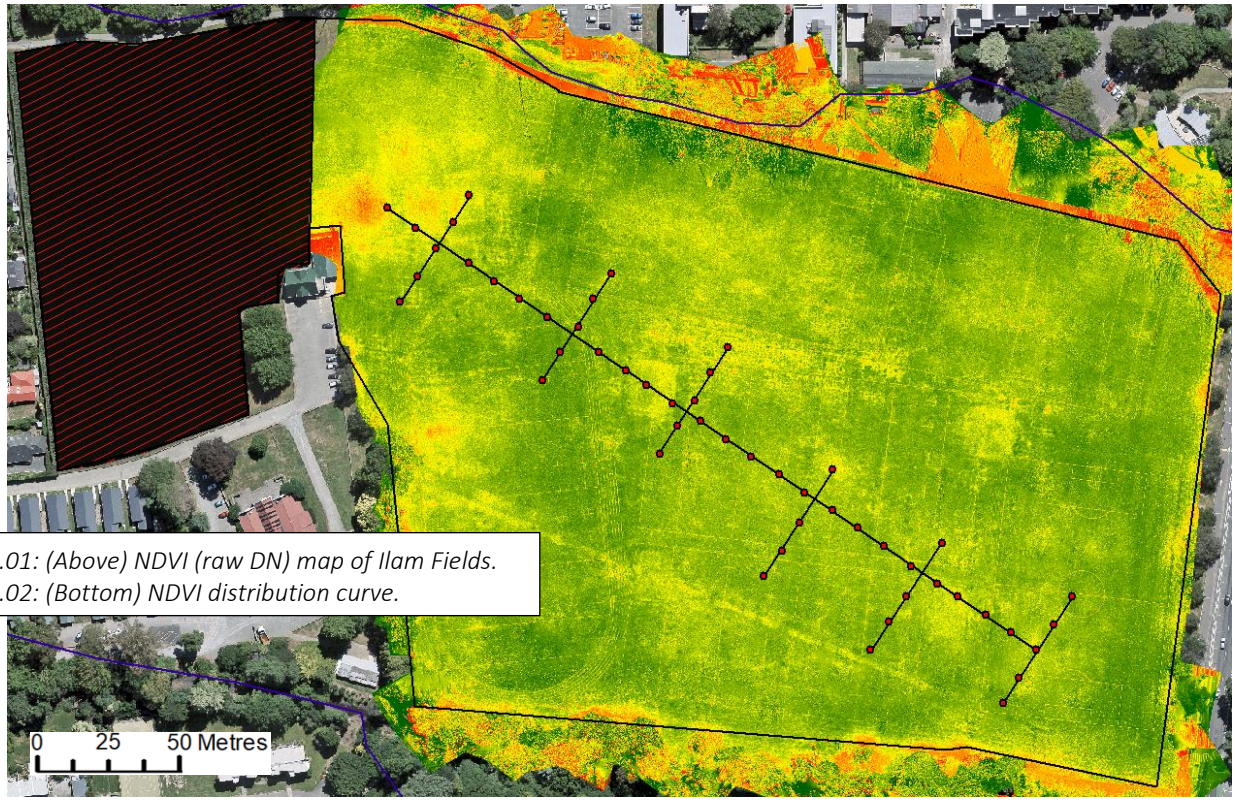

Figure 5.01: (Above) NDVI (raw DN) map of Ilam Fields.
Figure 5.02: (Bottom) NDVI distribution curve.

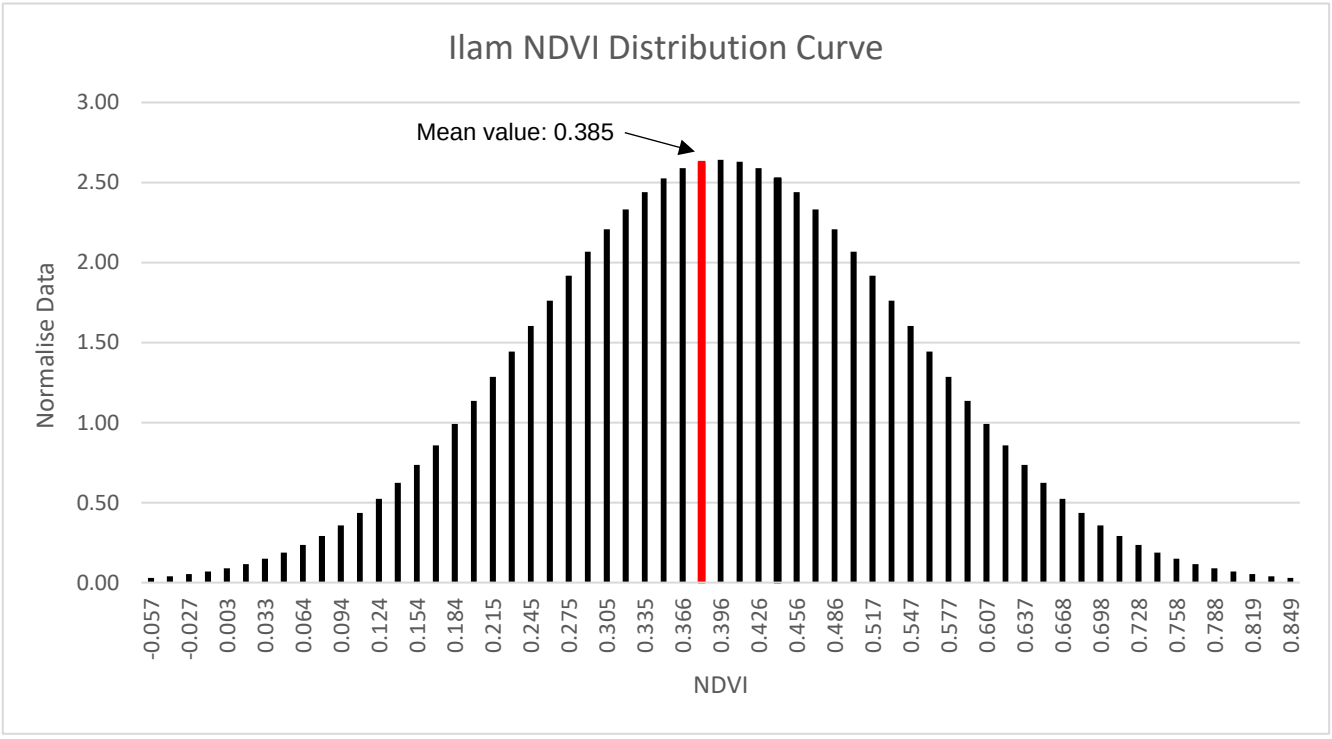

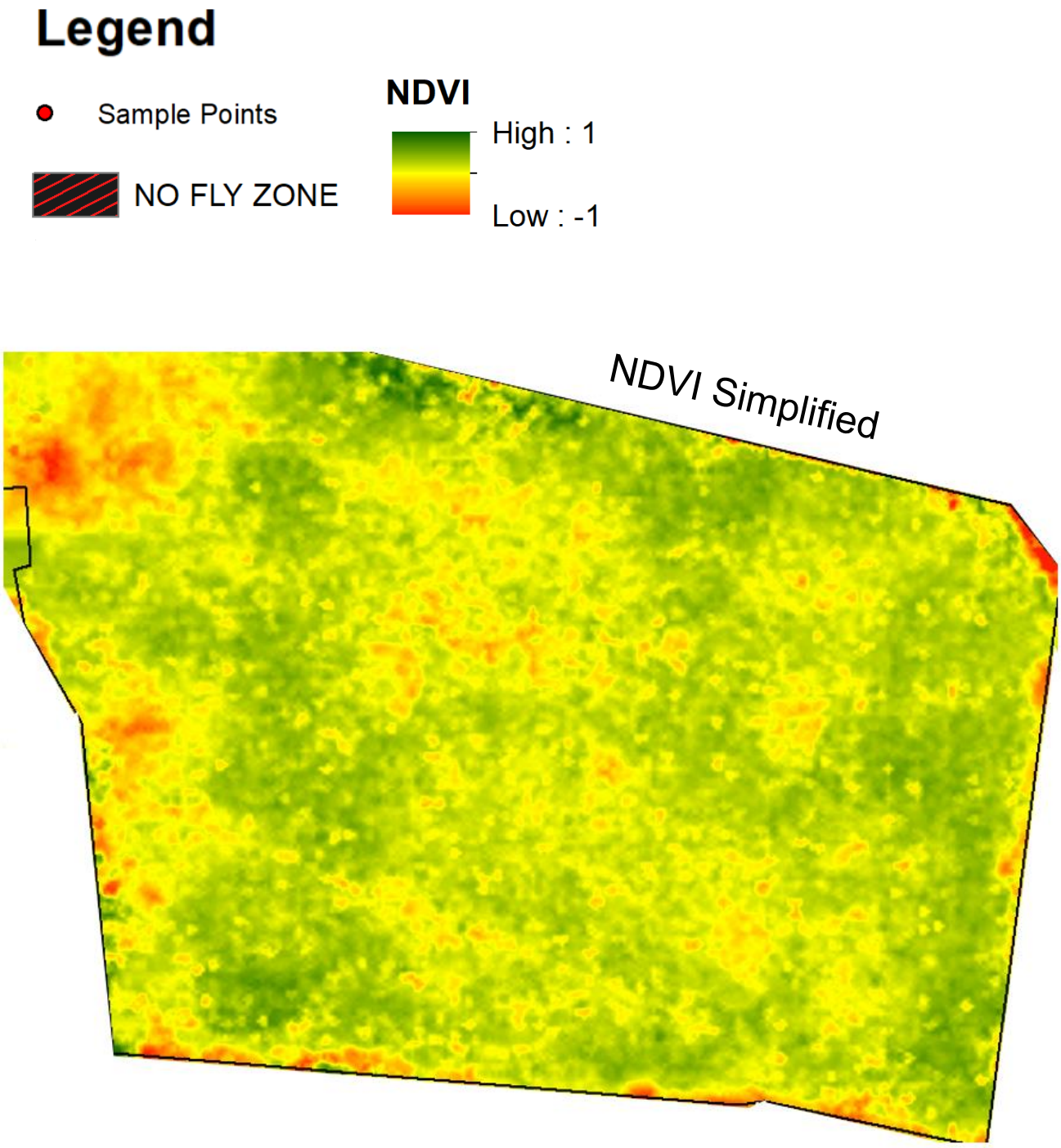

Stats	Mean	Std	Min	25%	50%	75%	Max	Range
NDVI	0.385	0.189	-0.057	0.184	0.372	0.612	0.849	-1-1

Figure 5.03: (Bottom Right) NDVI (Simplified) map of Ilam Fields.
Table 5.0: (Bottom) NDVI Table Ilam Fields.

Satellite Imagery

The image below shows the NDVI (figure 5.04) and infrared reflectance (figure 5.05) distribution from the Planet's Satellite imagery. These images were created in python using Planet's API (Application Programming Interface).

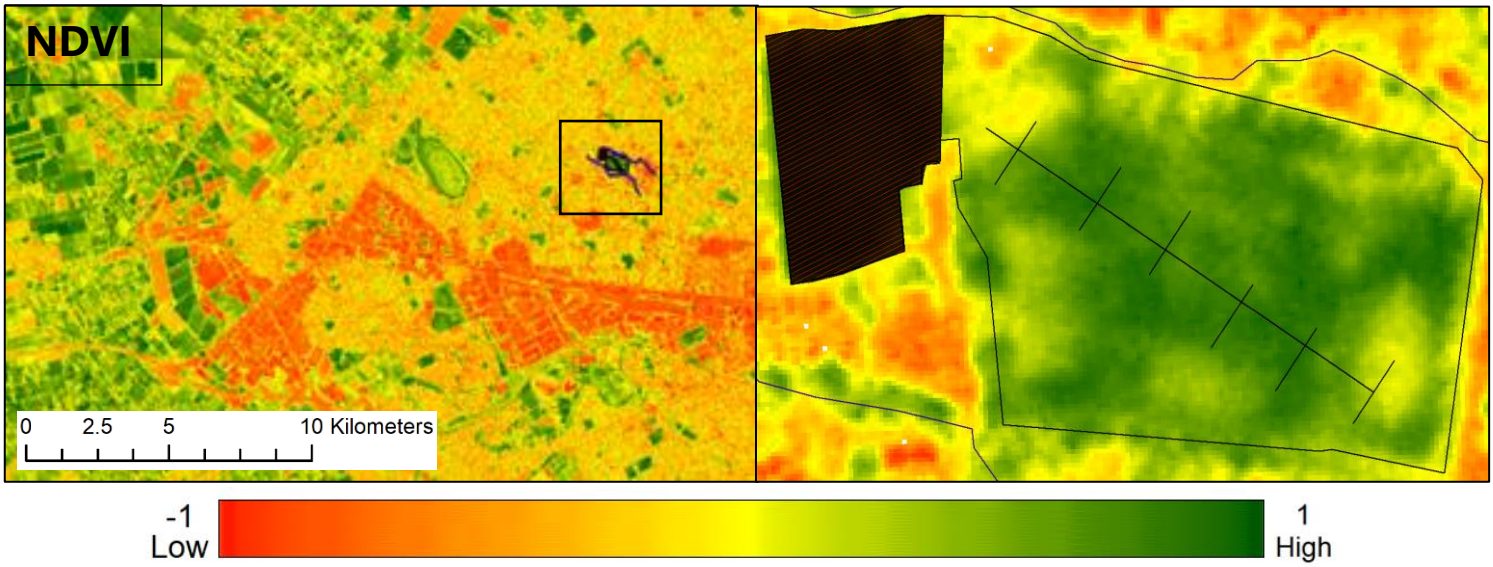

Figure 5.04: Satellite NDVI image of Ilam/ Central Christchurch region.

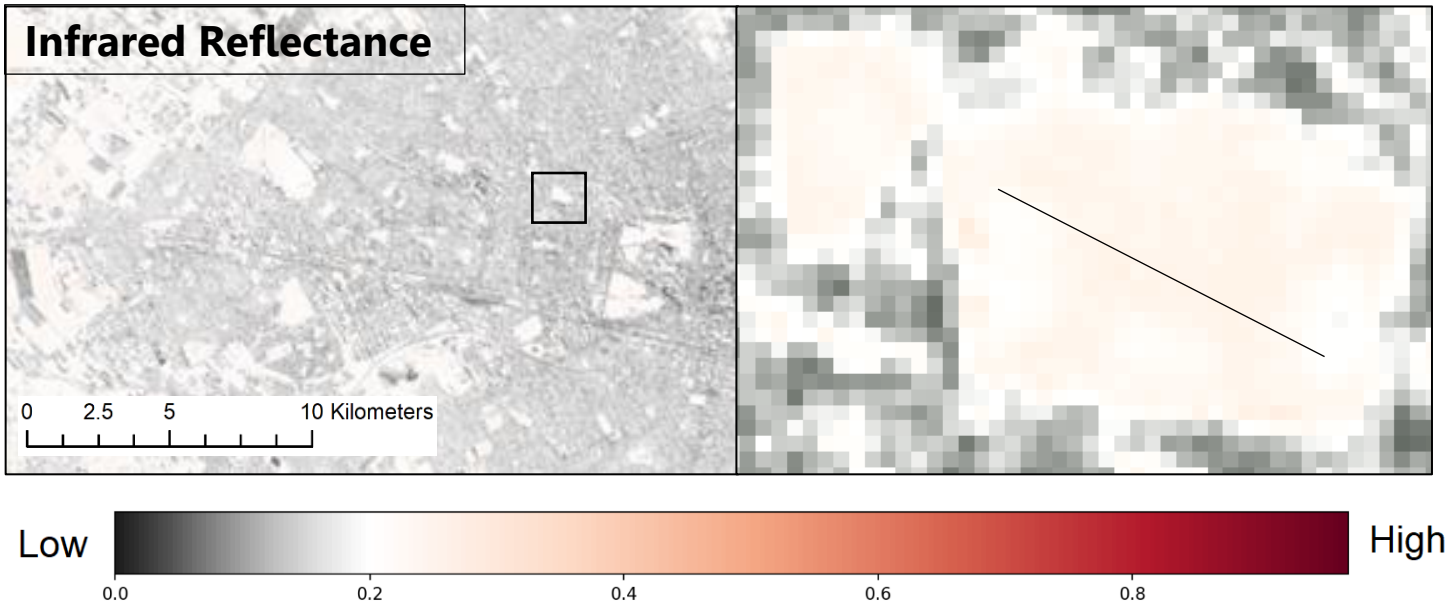

Figure 5.05: Satellite image of Infrared Reflectance in Ilam/ Central Christchurch region.

Soil Carbon Dioxide Flux

The CO_2 flux ranges from 0.21 to 1.15 ppm/s. The soil respiration rate of CO_2 increases towards the south-east.

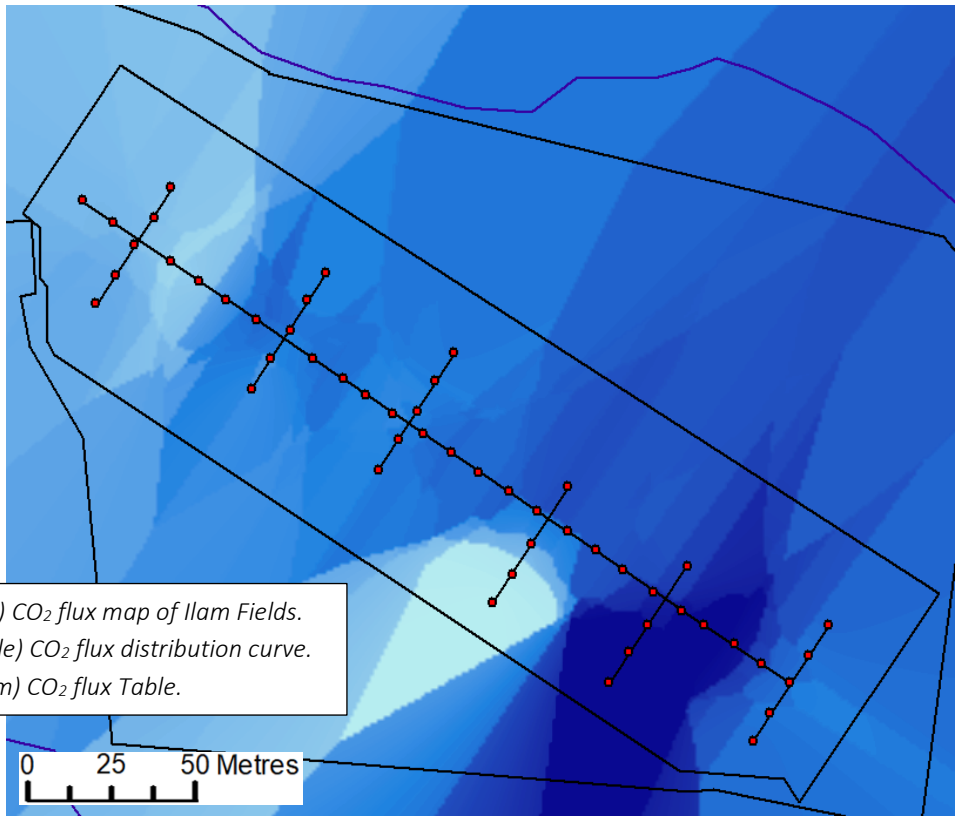

Figure 5.06: (Right) CO_2 flux map of Ilam Fields.
Figure 5.07: (Middle) CO_2 flux distribution curve.
Table 5.01: (Bottom) CO_2 flux Table.

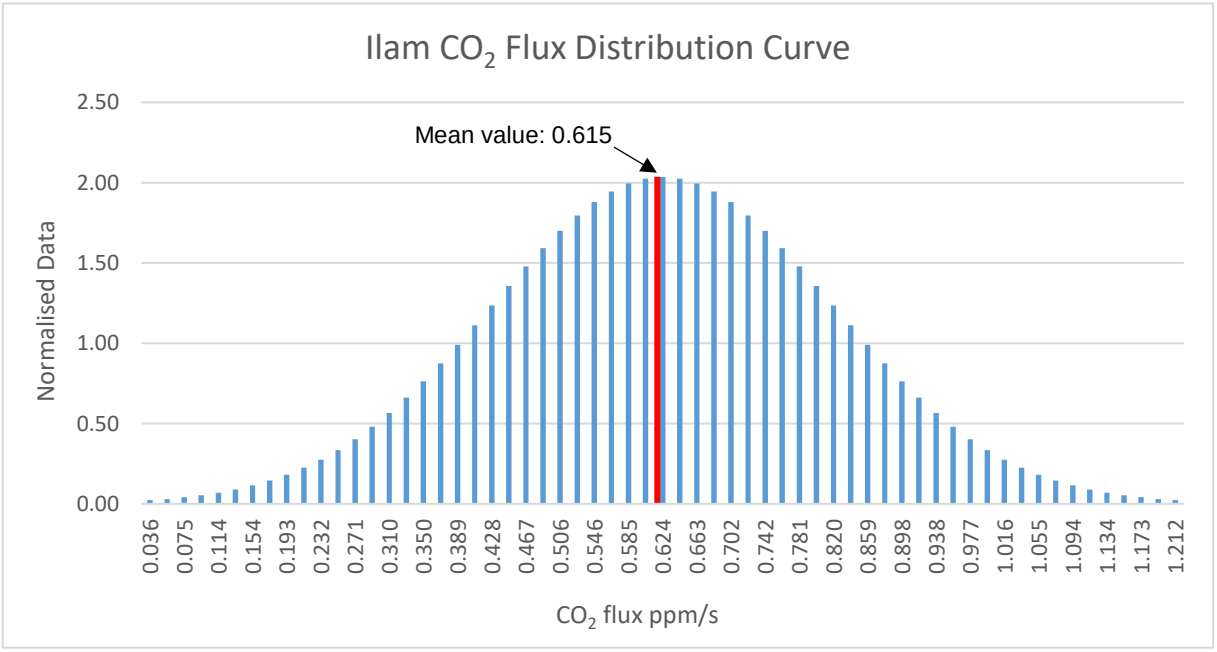

Stats	Mean	Std	Min	25%	50%	75%	Max	Range
CO_2 Flux	0.615	0.196	0.213	0.493	0.624	0.727	1.212	0.213-1.212

Soil Temperature at 20 cm Deep

The map below shows spatial distribution of the soil temperature at 20 cm deep within the Ilam field area. Soil temperature tends to build towards the center of the field compared to the north-west and south-east.

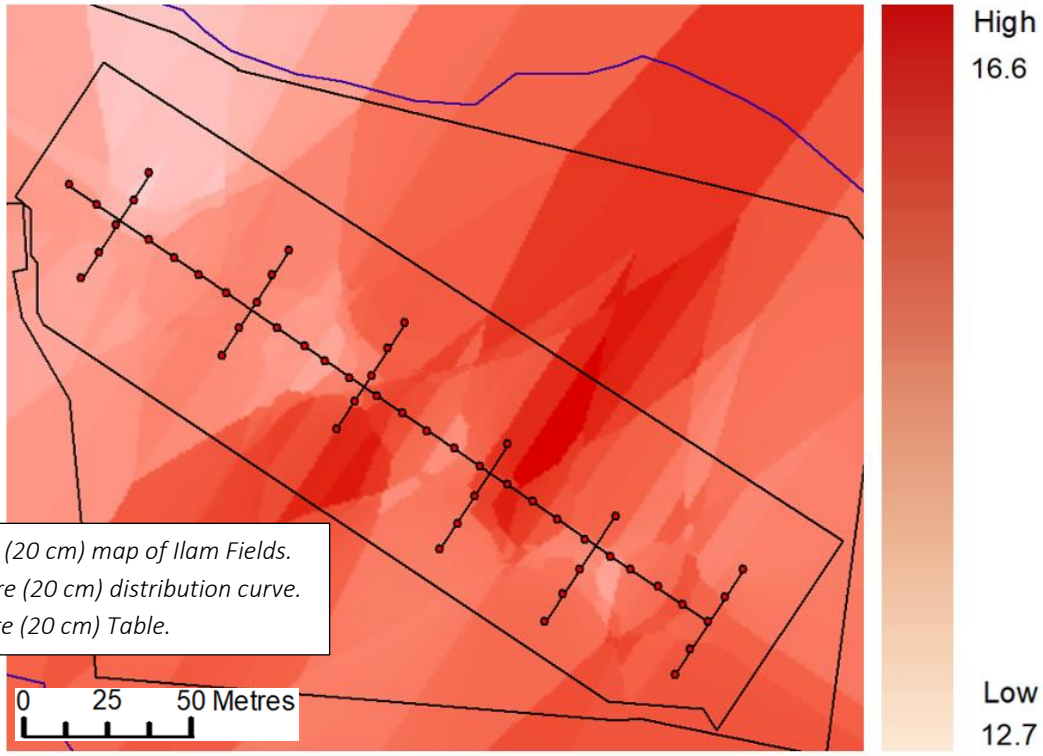

Figure 5.08: (Right) Soil Temperature (20 cm) map of Ilam Fields.
Figure 5.09: (Middle) Soil Temperature (20 cm) distribution curve.
Table 5.02: (Bottom) Soil Temperature (20 cm) Table.

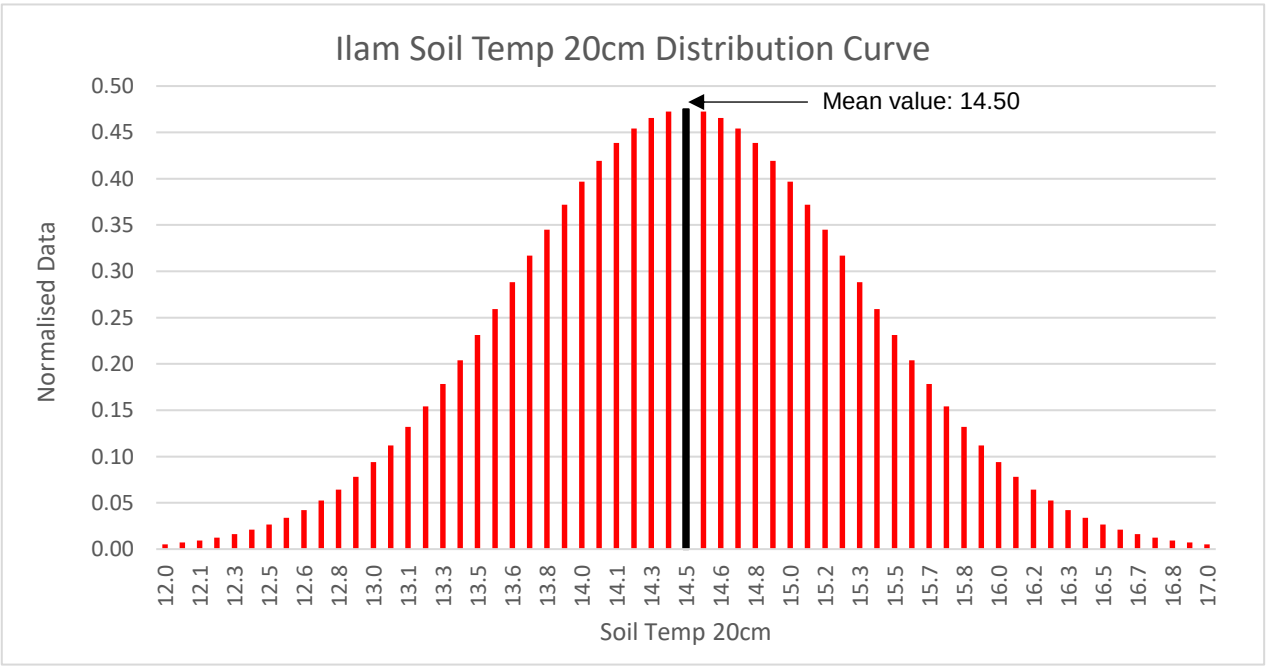

Stats	Mean	Std	Min	25%	50%	75%	Max	Range
ST20	14.50	0.84	12.66	13.99	14.43	15.03	16.92	12.66-16.92

Soil Temperature at 50 cm Deep

The 20 and 50 cm soil temperature profiles follow similar patterns and is consistently within ~0.5 degree warmer than the 20 cm map and in the same areas.

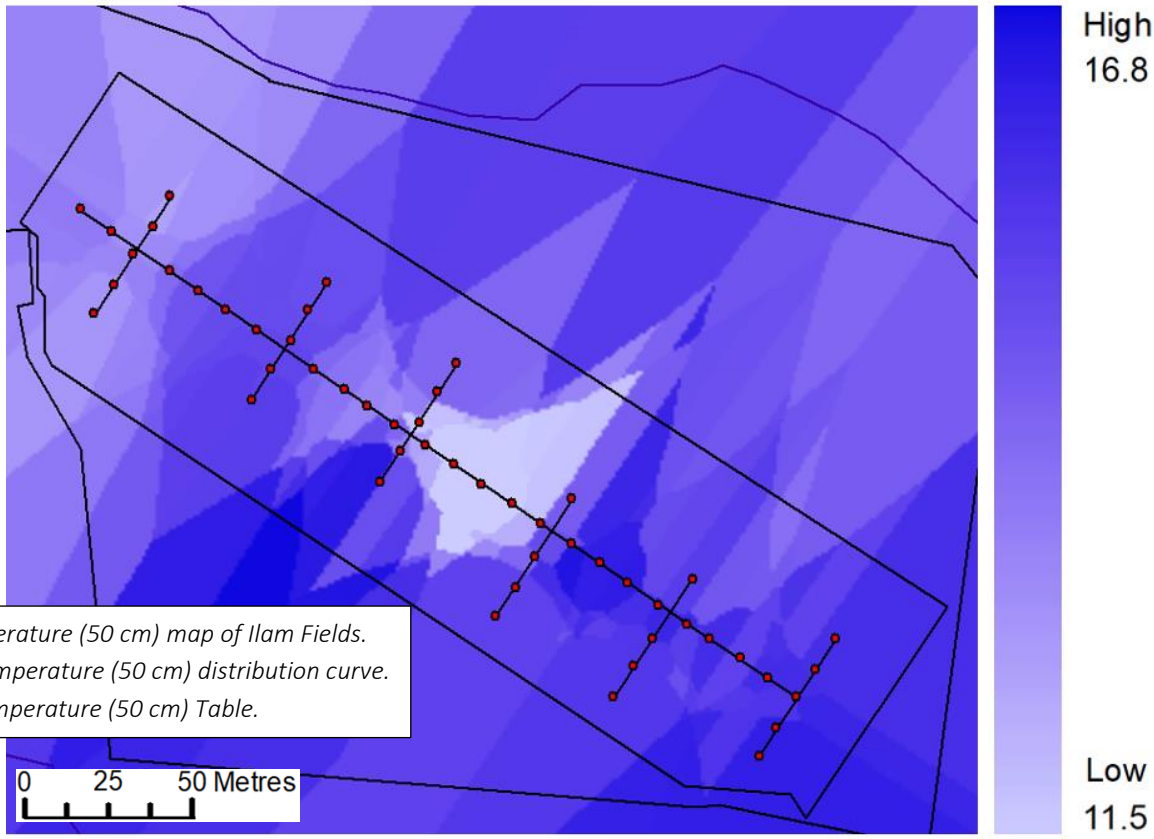

Figure 5.1: (Right) Soil Temperature (50 cm) map of Ilam Fields.
Figure 5.11: (Middle) Soil Temperature (50 cm) distribution curve.
Table 5.03: (Bottom) Soil Temperature (50 cm) Table.

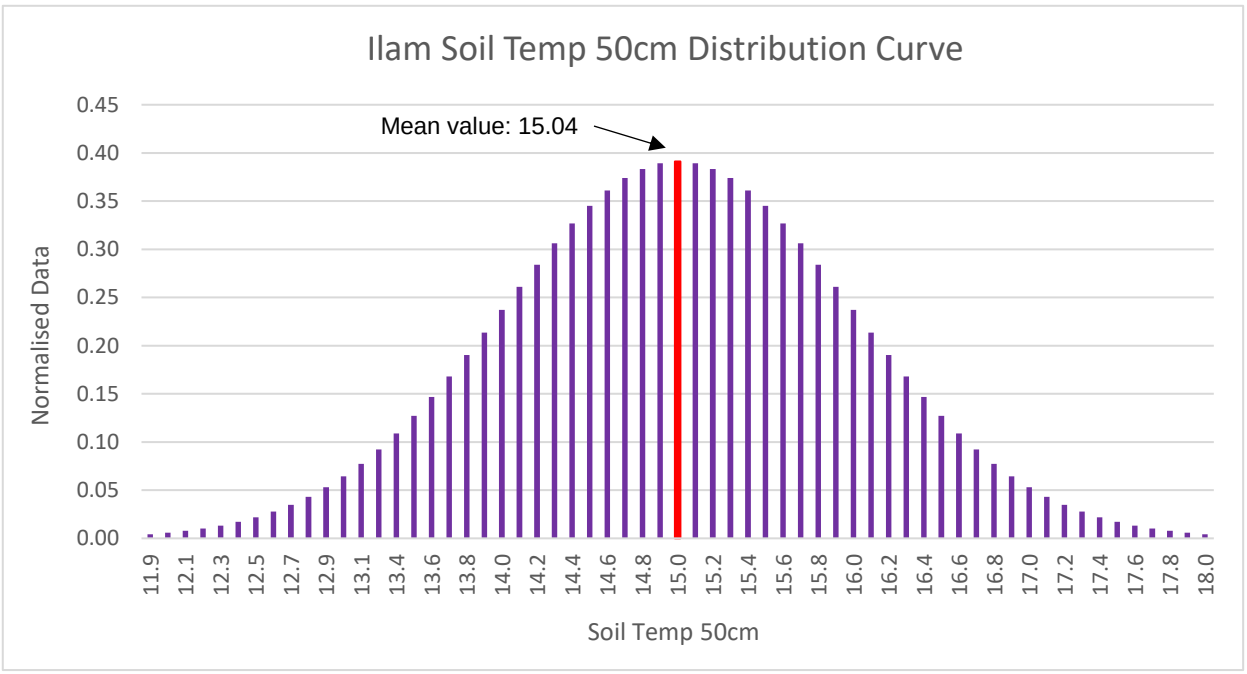

Stats	Mean	Std	Min	25%	50%	75%	Max	Range
ST50	15.04	1.02	11.54	14.33	15.30	15.77	16.80	11.54-16.80

Surface Temperature

The surface temperature recorded by the Zenmuse XT2 was used to create this map. On the surface, the north-west displays higher surface temperature versus the south-east.

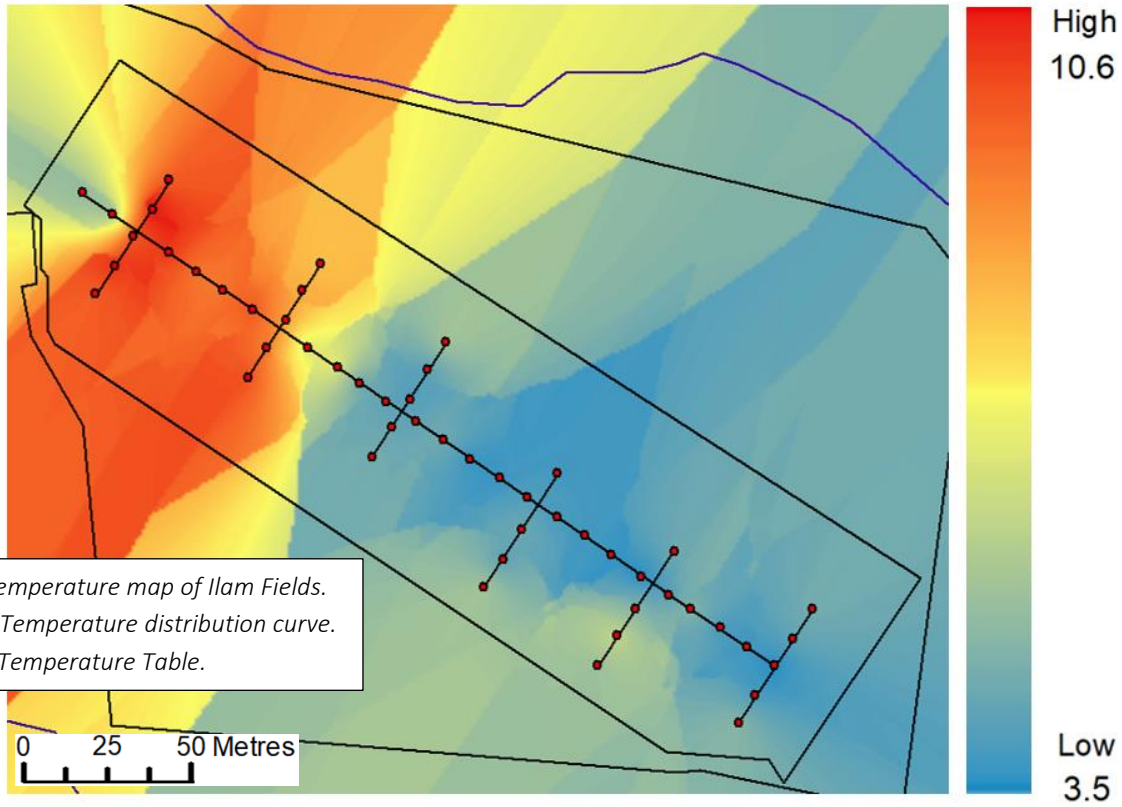

Figure 5.12: (Right) Surface Temperature map of Ilam Fields.
Figure 5.13: (Middle) Surface Temperature distribution curve.
Table 5.04: (Bottom) Surface Temperature Table.

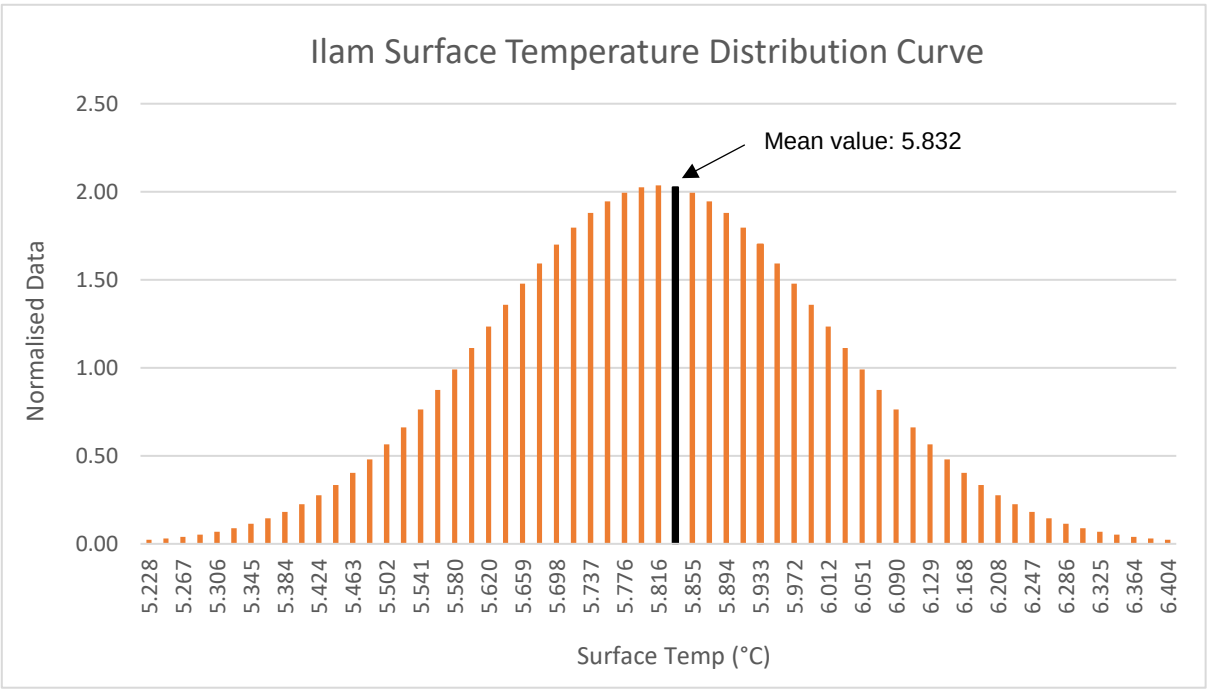

Stats	Mean	Std	Min	25%	50%	75%	Max	Range
Surface Temp	5.832	2.17	3.51	4.25	5.80	8.057	10.54	3.50-10.54

Harihari Field Site

The bottom half of the Harihari field (figure 5.14) was used for the field sampling and remote sampling. As previously mentioned in chapter III the field sampling was done every 12.5 meters totaling for 37 sample sites.

Figure 5.14: (Above) Aerial view of Harihari field site.
Figure 5.15: (Below) Oblique view of the Harihari field site.

The sampling was completed by myself, Travis H. and Du Chen, of which commenced at 10:45am and was completed by 1:30pm. The grass was relatively wet as a result of the morning dew as it had not rained in the prior 30+ hours, and the soil was partially dry in places other than the swamp. The land at the cliff edge was above active hydrothermal fluids as seen in the thermal optics. Surface temperature conditions ~5.9 °C.

However, on Wednesday 26 March 2019, during a period of 48hrs torrential rain delivered approximately 20 – 30mm/hr, which is the highest level on record. The flooding eroded a significant volume of land from the study site that is estimated to be ~68,000 m^3.

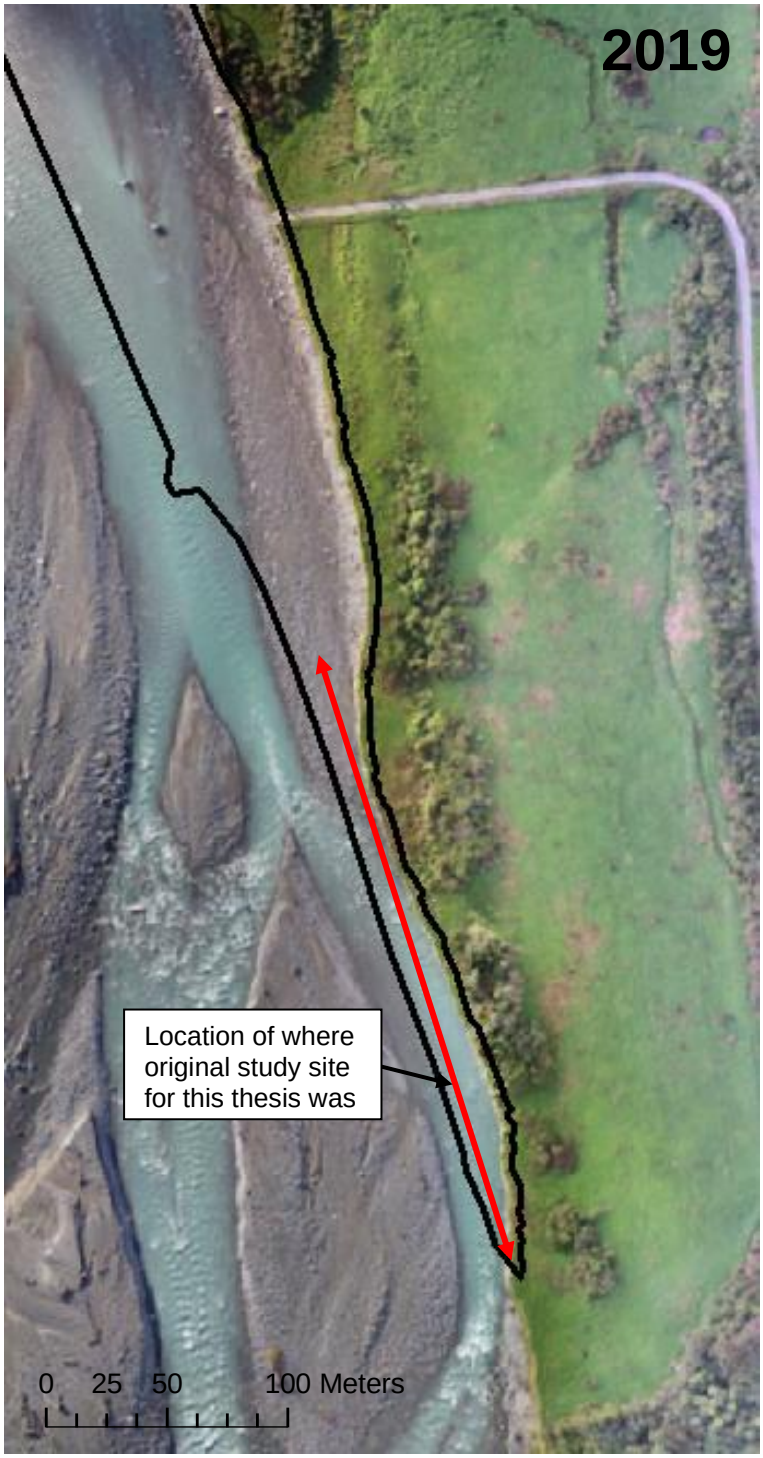

Figure 5.16: (Above Left) Aerial view of Harihari field site March 2011.
Figure 5.17: (Above Right) Aerial view of Harihari field site April 2019.
The two maps above show the amount of land erosion to the study site caused by the 2019 flooding event.

Harihari Field Observations

The vegetation found in the field was made up of mostly bladed grass (2 cm – 8 cm long), creeping buttercup, docks, sorrel and rushes. This brings added complexity to the infrared images when dealing with NDVI distribution because unlike Ilam, Harihari has more than one type vegetation present in the field. The range of plant species are expected to all respond slightly differently to infrared radiation.

The circle below indicates the location of the wet and swampy spot. The field site as a whole appeared to be unused for some time as there were no signs of human or animal interaction present, no visible tracks in the field other than our own. There was a port-a-loo towards the Southern part of the field, but looked like many years had passed since its last use. The sampling was conducted in three transects, the first two is 125 metres long and the third is 165 metres with each point done in 12.5m intervals.

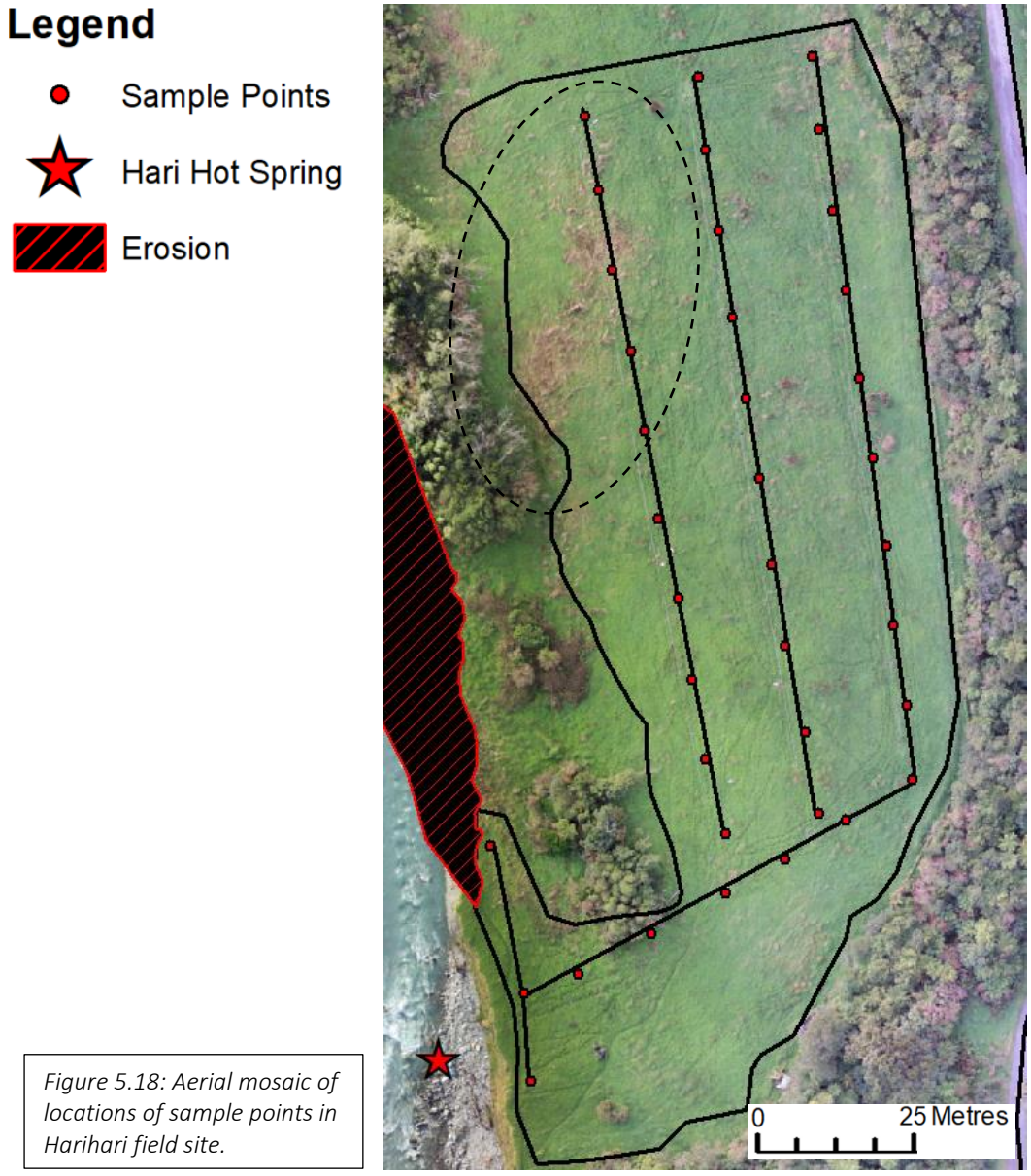

Figure 5.18: Aerial mosaic of locations of sample points in Harihari field site.

NDVI

The overall NDVI distribution is shown in the map below along with the exact points that were sampled. The NDVI map on the left uses the raw digital numbers while the map on the right uses a simplified version (average value at lower resolution) that highlights lower NDVI features.

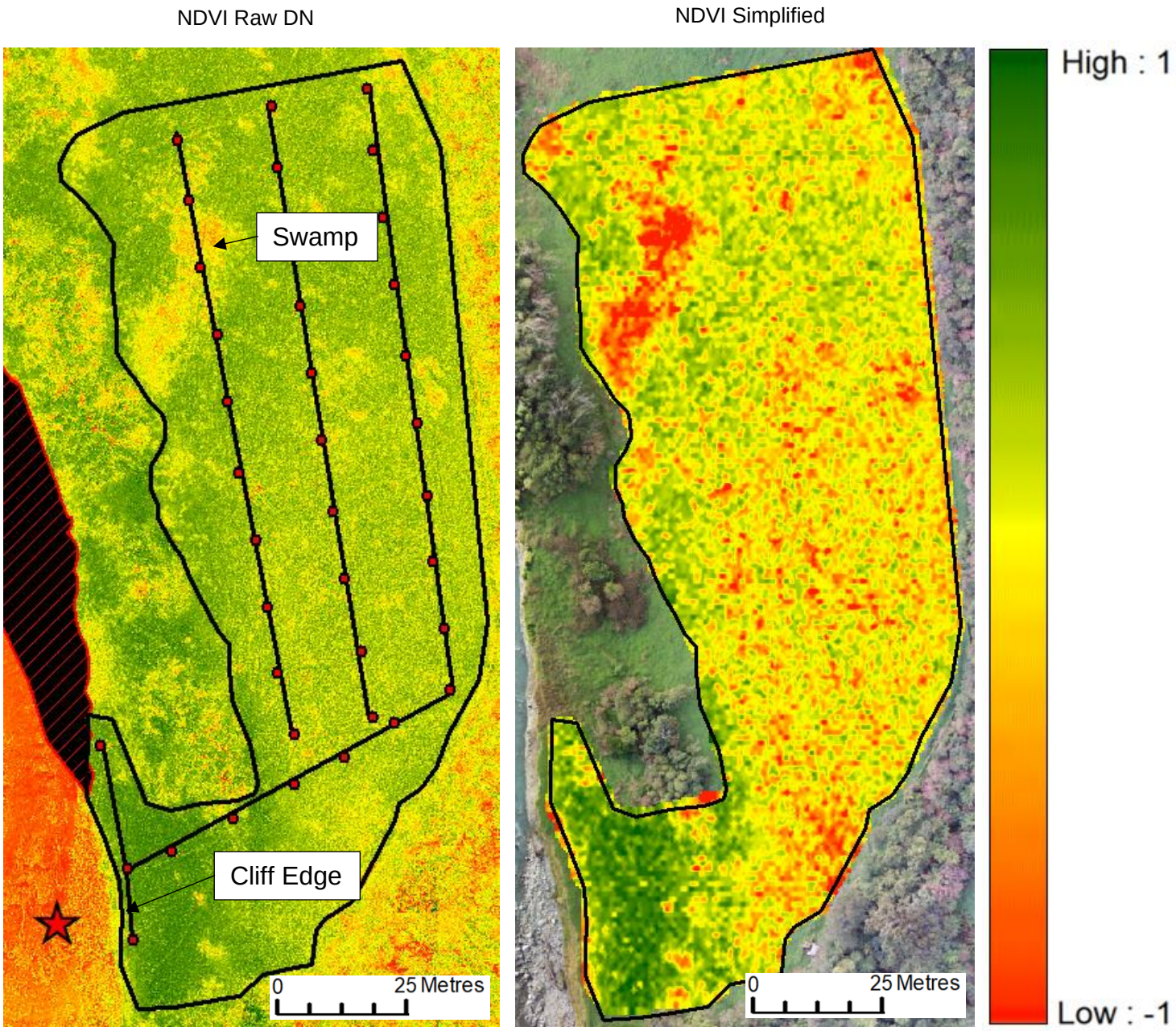

Figure 5.19: NDVI (raw DN) map of Harihari Field and NDVI simplified map

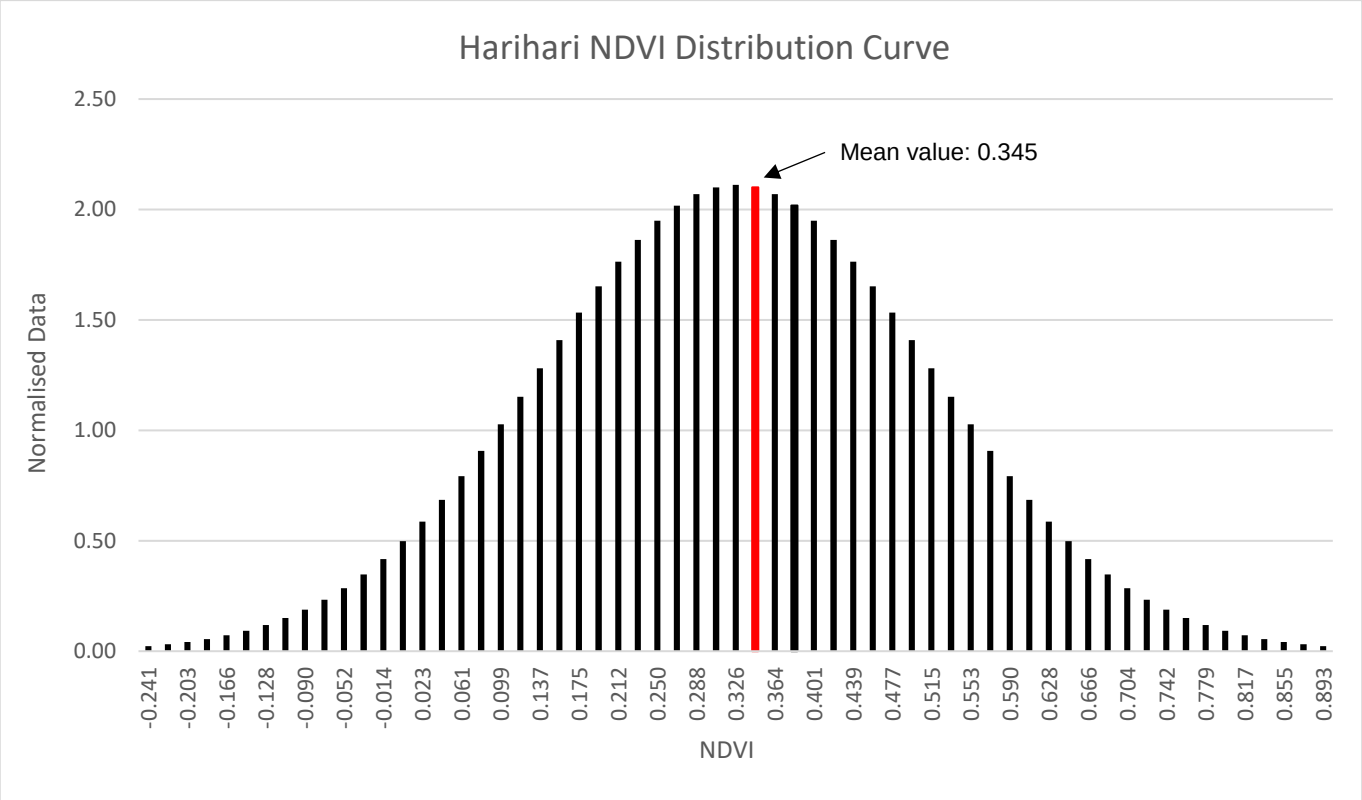

Figure 5.2: (Above) Harihari NDVI distribution Curve
Table 5.05: (Bottom) NDVI Table.

Stat	Mean	Std	Min	25%	50%	75%	Max	Range
NDVI	0.345	0.189	-0.241	0.117	0.326	0.534	0.893	-1-1

Satellite Imagery

The image below shows the NDVI (figure 5.21) and infrared reflectance (5.22) distribution from the Planet's Satellite imagery. These images were created in python using Planet's API (Application Programming Interface).

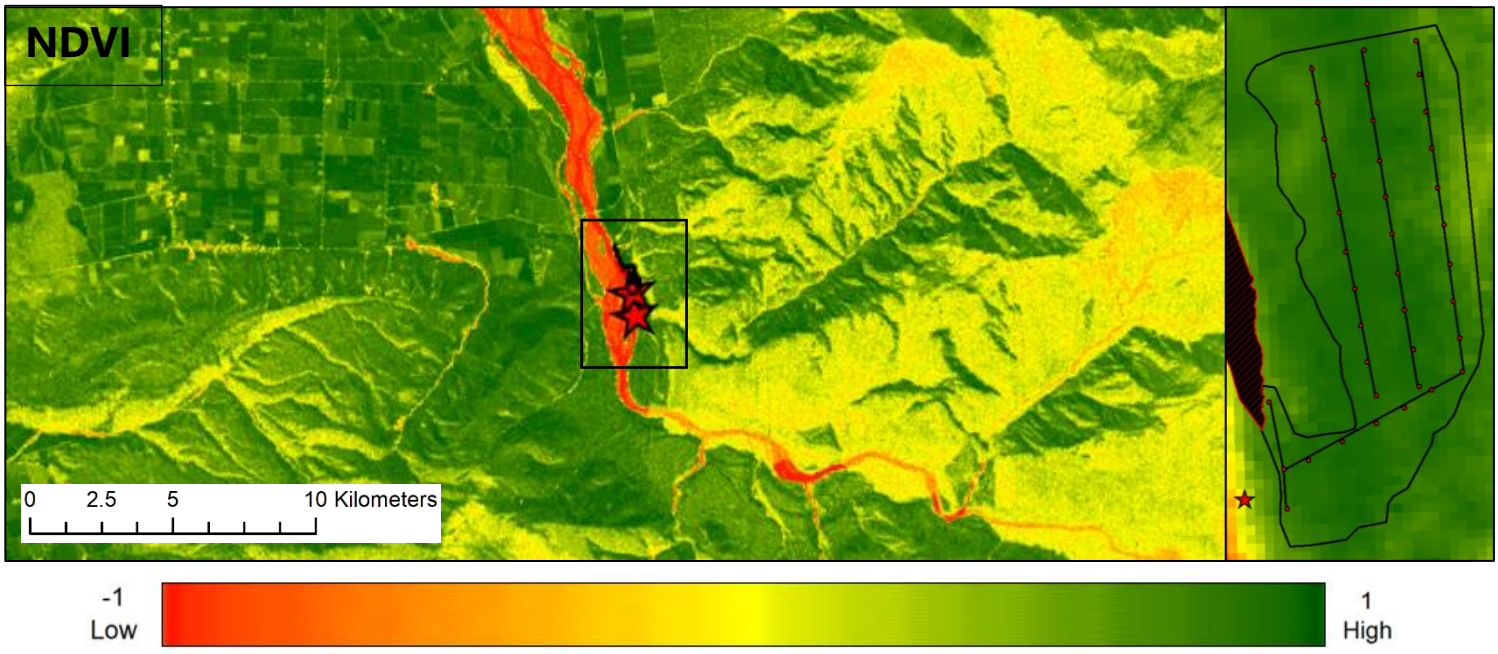

Figure 5.21: Satellite NDVI image of the region west of Harihari.

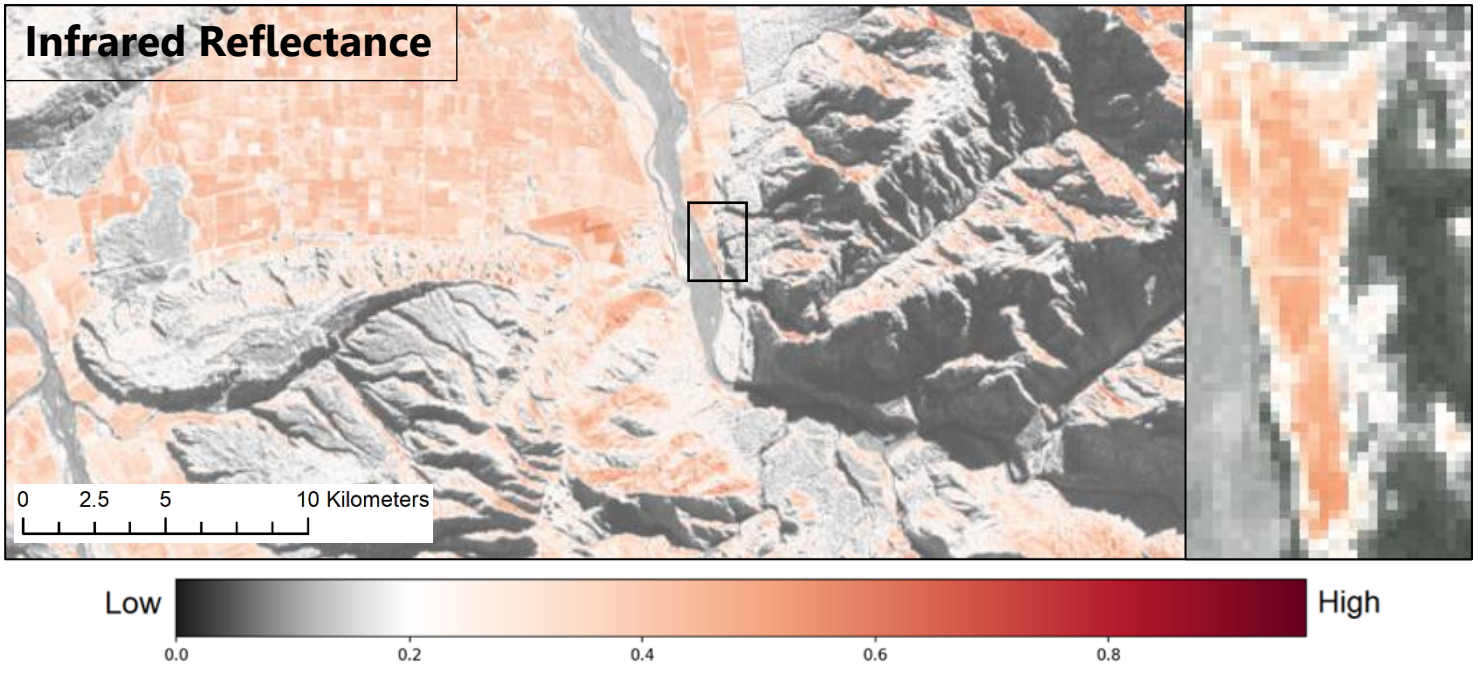

Figure 5.22: Satellite image of Infrared Reflectance in the region west of Harihari.

Soil Carbon Dioxide Flux

The CO_2 flux ranges from 0.15 to 2.05 ppm/s. The flow of CO_2 from the soil to atmosphere increases towards the south and decrease in the swamp.

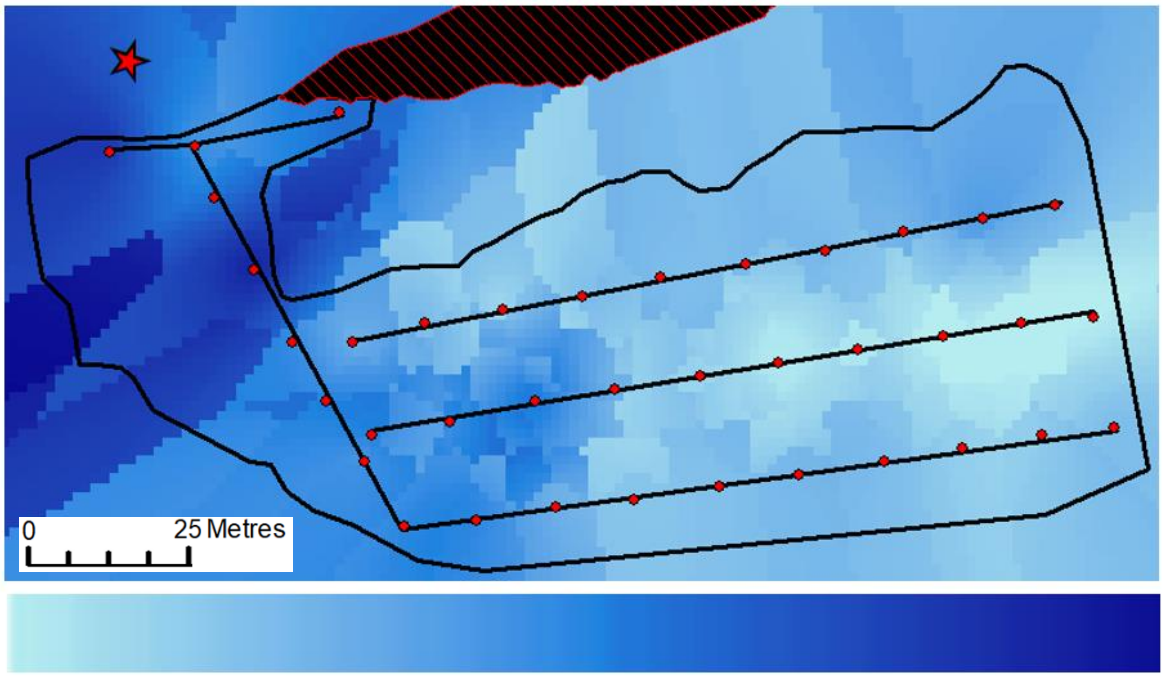

Low : 0.15 High : 2.05

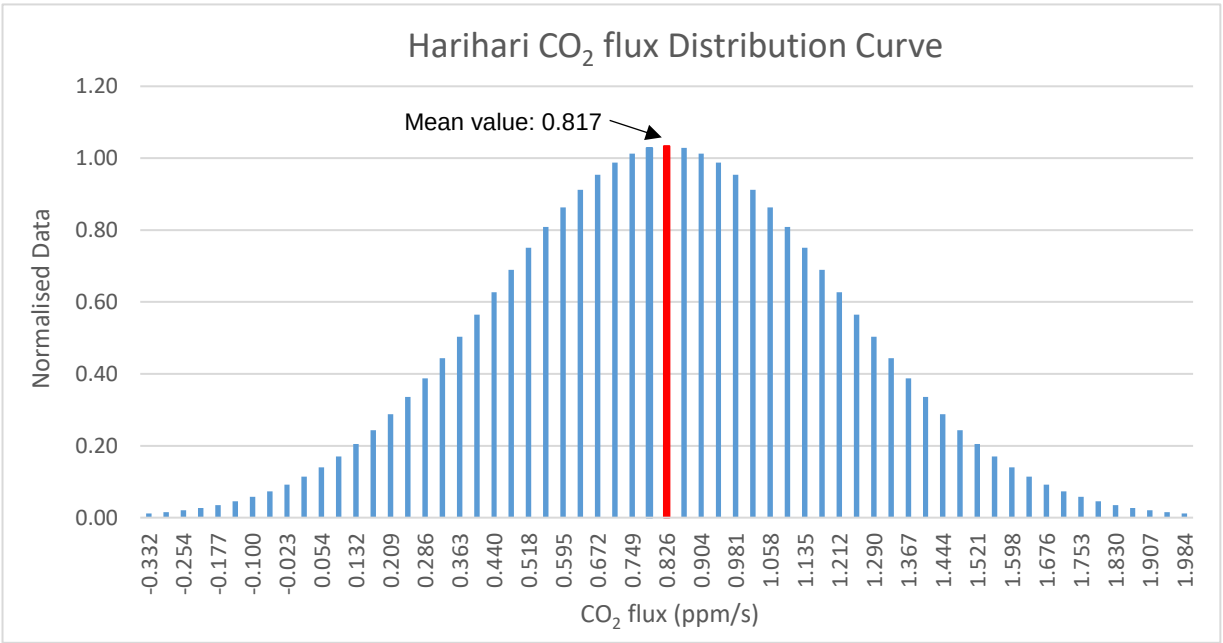

Stat	Mean	Std	Min	25%	50%	75%	Max	Range
CO_2 Flux	0.817	0.386	0.152	0.363	0.826	1.251	2.018	0.152-2.018

Figure 5.23: (Above) CO_2 flux map of Harihari Field Site.
Figure 5.24: (Middle) CO_2 flux distribution curve. (no negative flux, graph error).
Table 5.06: (Bottom) CO_2 flux Table.

Soil Temperature at 20 cm Deep

The map below shows spatial distribution of the soil temperature at 20 cm deep within the Harihari field area. The variation of soil temperature appears to be sporadic but increases to the south and in the swamp.

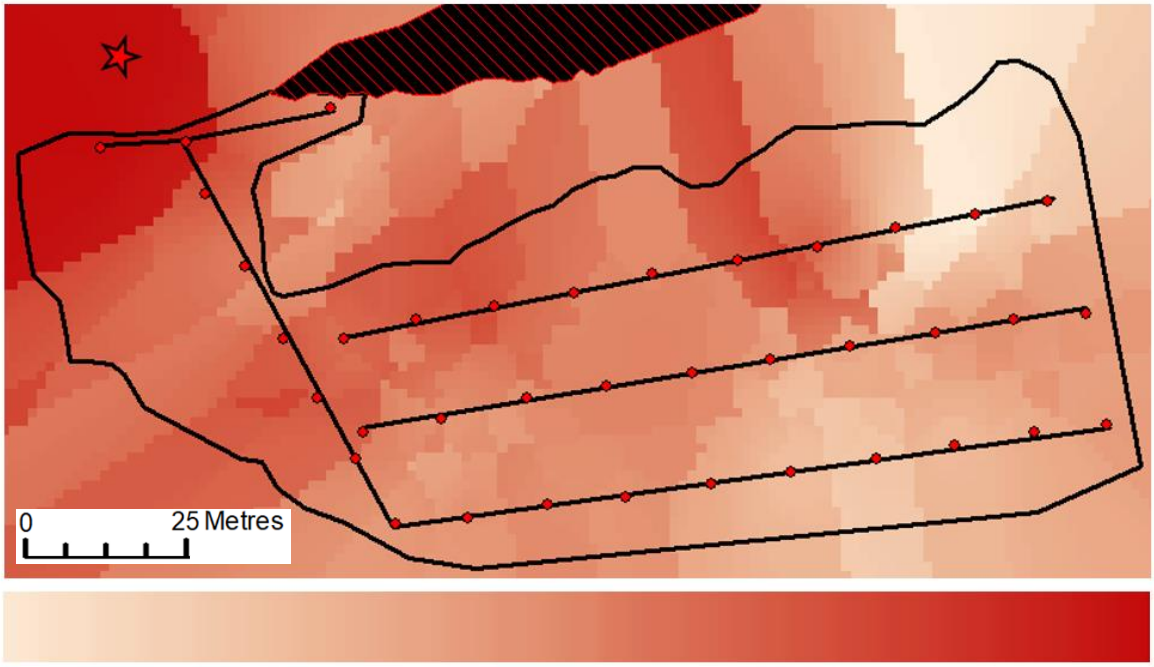

Low : 11.26 High : 13.25

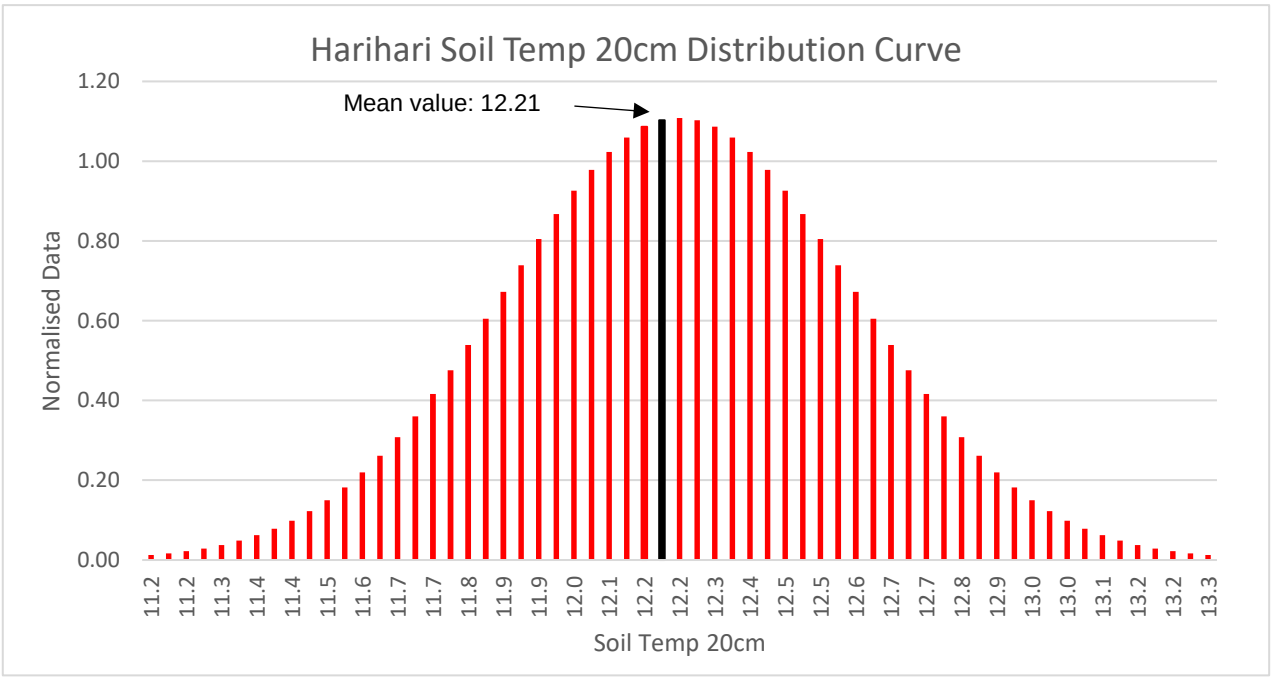

Stat	Mean	Std	Min	25%	50%	75%	Max	Range
ST20	12.21	0.366	11.26	11.98	12.22	12.73	13.31	11.26-13.25

Figure 5.25: (Above) Soil Temperature (20 cm) map of Harihari Field Site.
Figure 5.26: (Middle) Soil Temperature (20 cm) distribution curve.
Table 5.07: (Bottom) Soil Temperature (20 cm) Table.

Soil Temperature at 50 cm Deep

The 20 and 50 cm soil temperature profiles follow similar patterns and is consistently ~1 °C warmer than the 20 cm map with major spikes in the south-west and towards the swamp.

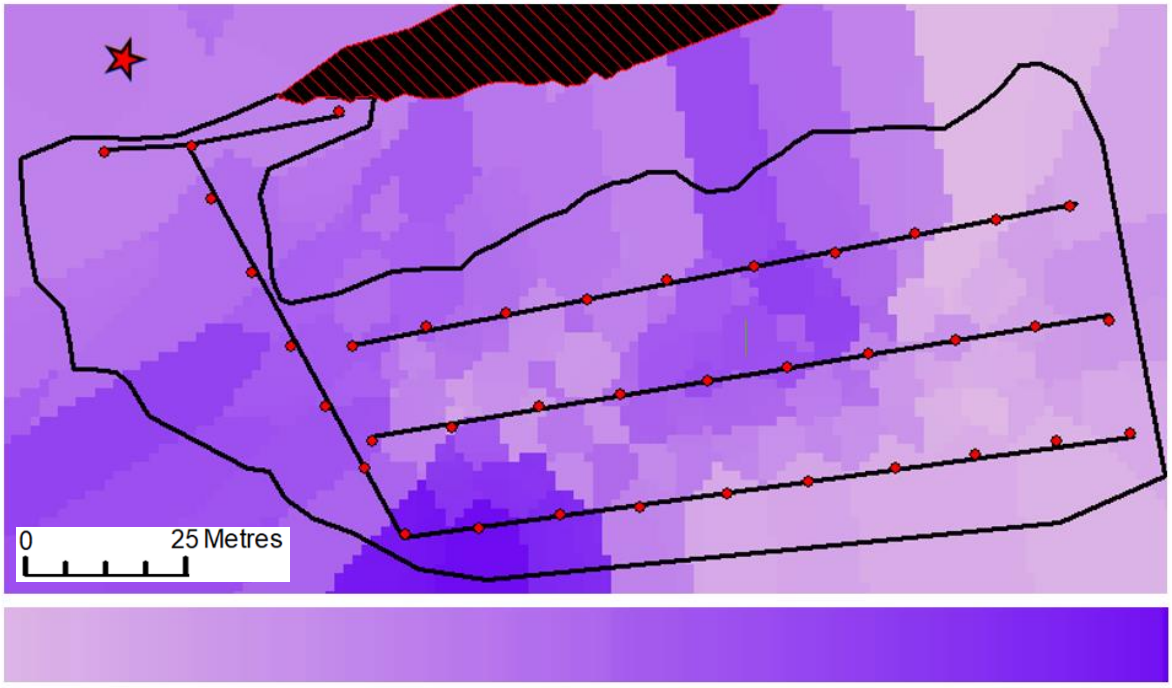

Low : 11.91 High : 14.63

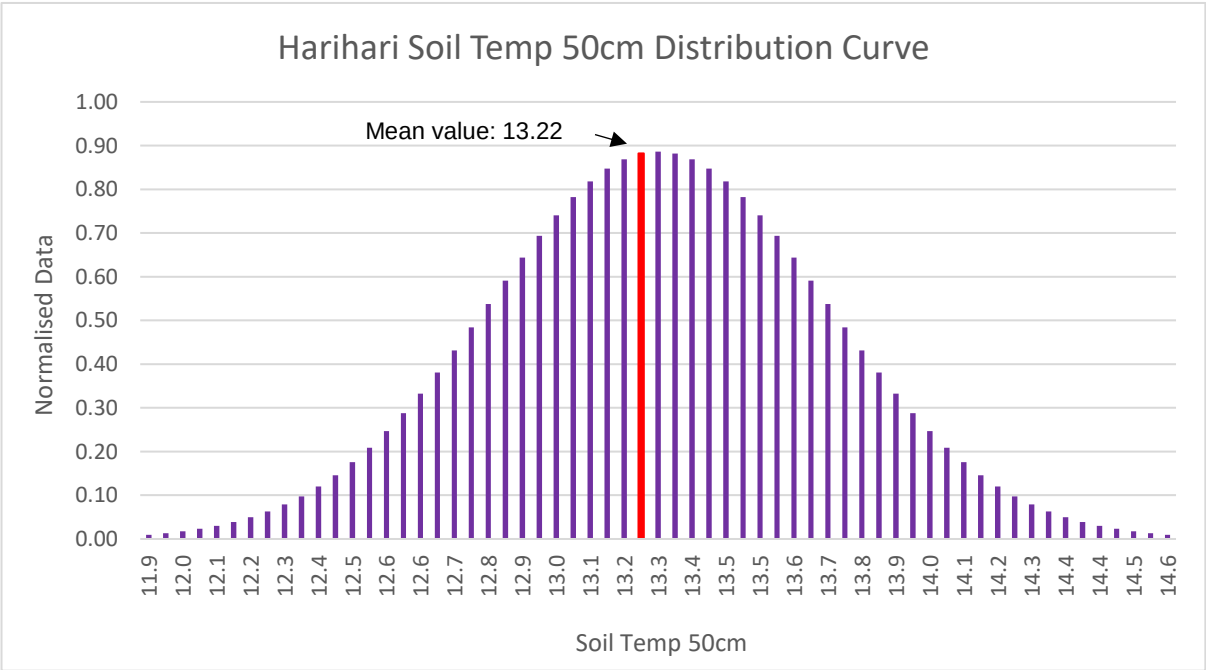

Stat	Mean	Std	Min	25%	50%	75%	Max	Range
ST50	13.22	0.48	11.91	12.77	13.32	13.80	14.63	11.91-14.63

Figure 5.27: (Above) Soil Temperature (50 cm) map of Harihari Field Site.
Figure 5.28: (Middle) Soil Temperature (50 cm) distribution curve.
Table 5.08: (Bottom) Soil Temperature (50 cm) Table.

Surface Temperature

The surface temperature recorded by the Zenmuse XT2 produced this map. A warm area consistent with the highlighted values in soil temperature, and CO_2 flux shows the same pattern. This thermal area appears to cut through the existing cooler land; and rises again towards the cliff edge.

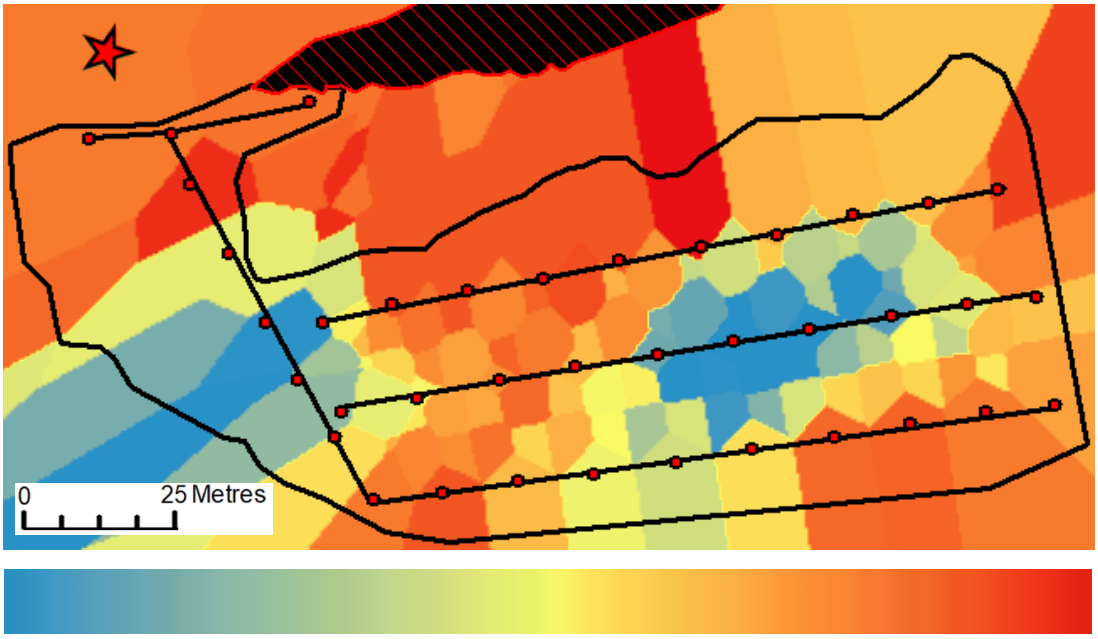

Low : 4.2

High : 6.4

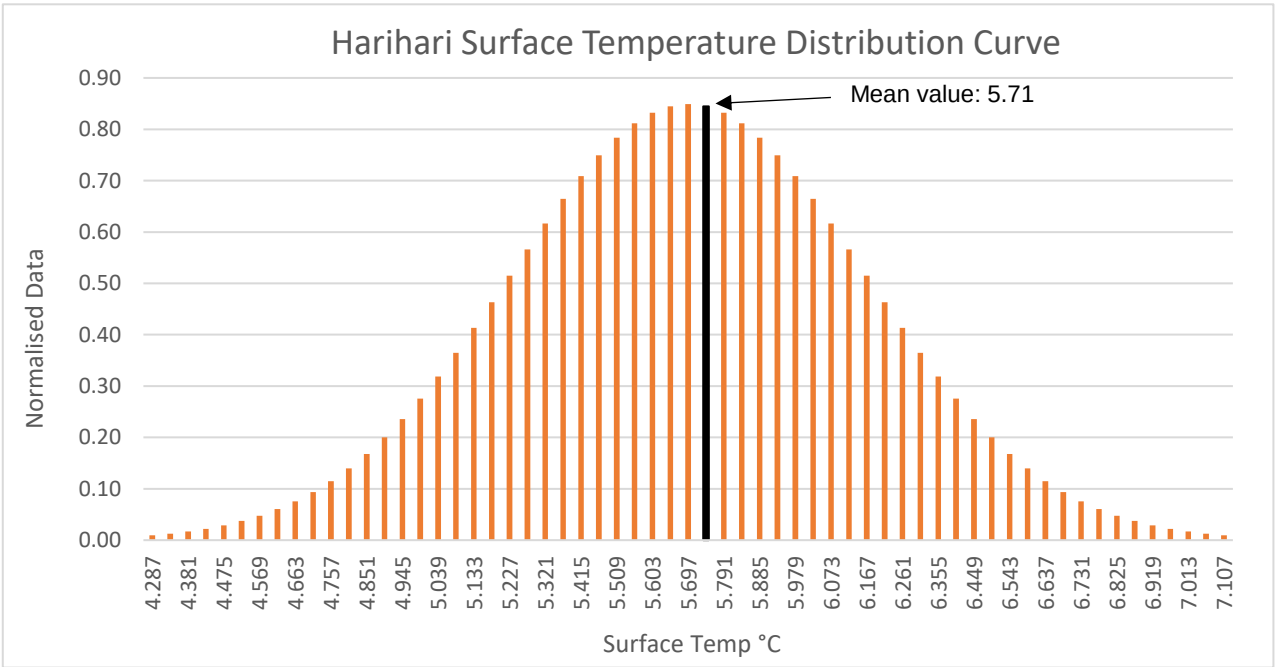

Stat	Mean	Std	Min	25%	50%	75%	Max	Range
Surface Temp	5.71	0.47	4.20	5.43	5.83	6.03	6.37	4.20-6.37

Figure 5.29: (Above) Surface Temperature map of Harihari Field Site.
Figure 5.3: (Middle) Surface Temperature distribution curve.
Table 5.09: (Bottom) Surface Temperature Table.

Thermal Optics

The thermal video over the Harihari study site was able to pick up the hydrothermal fluids protruding from the base of the cliff edge. Temperatures recorded with the Zenmuse XT2 is consistent the temperatures measured by soil probe with values of ~20 °C in the same area (figure 5.33).

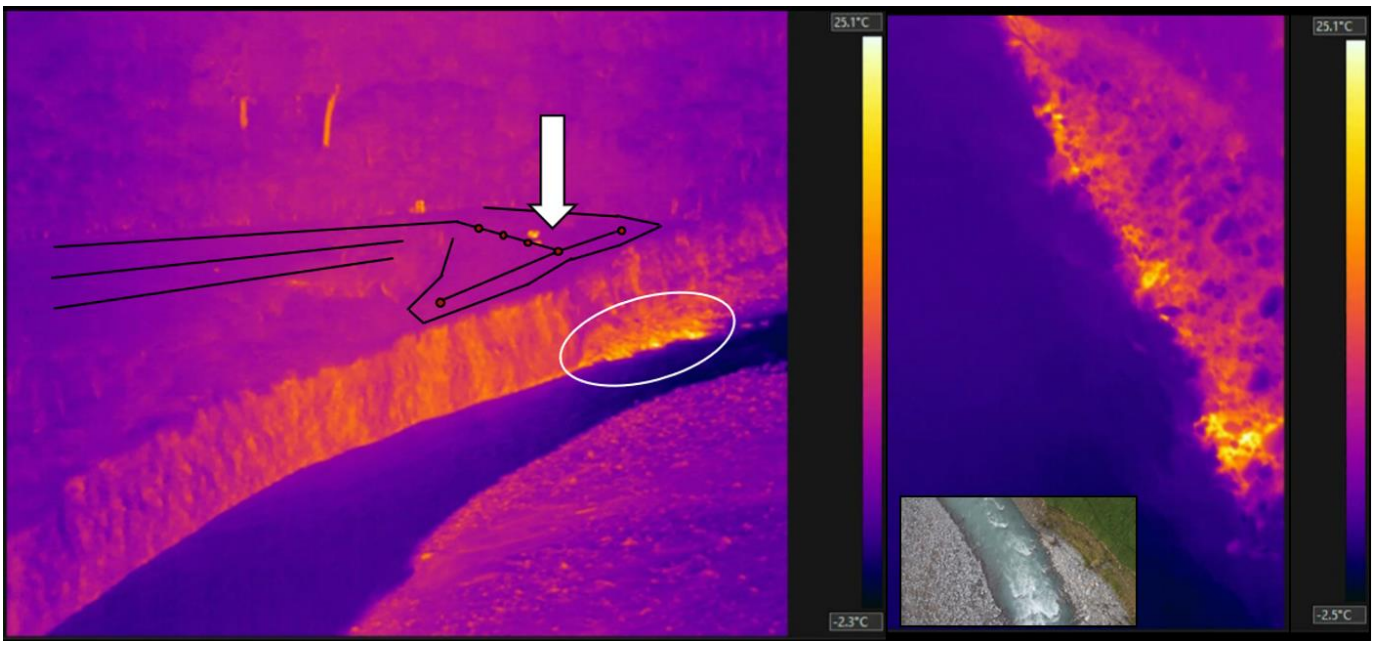

Figure 5.31: (Above) Screenshot is of a video made using video editing software (Adobe Premier CC 2019). Image shows thermal distribution on the bank of the Harihari Field Site. The close up on the right picks out the finer detail in the upwelling thermal fluids.

Figure 5.32: (Below) Image taken in 2015 of a thermal pool before the 2019 storm event that eroded a large part of the banks near the study site.

Not included in the field study but functioned as an auxiliary area, is a site further south of the Harihari field site. Field surveys produced a max temperature of 50 °c. The cluster of maps below show the thermal distribution of the hot springs.

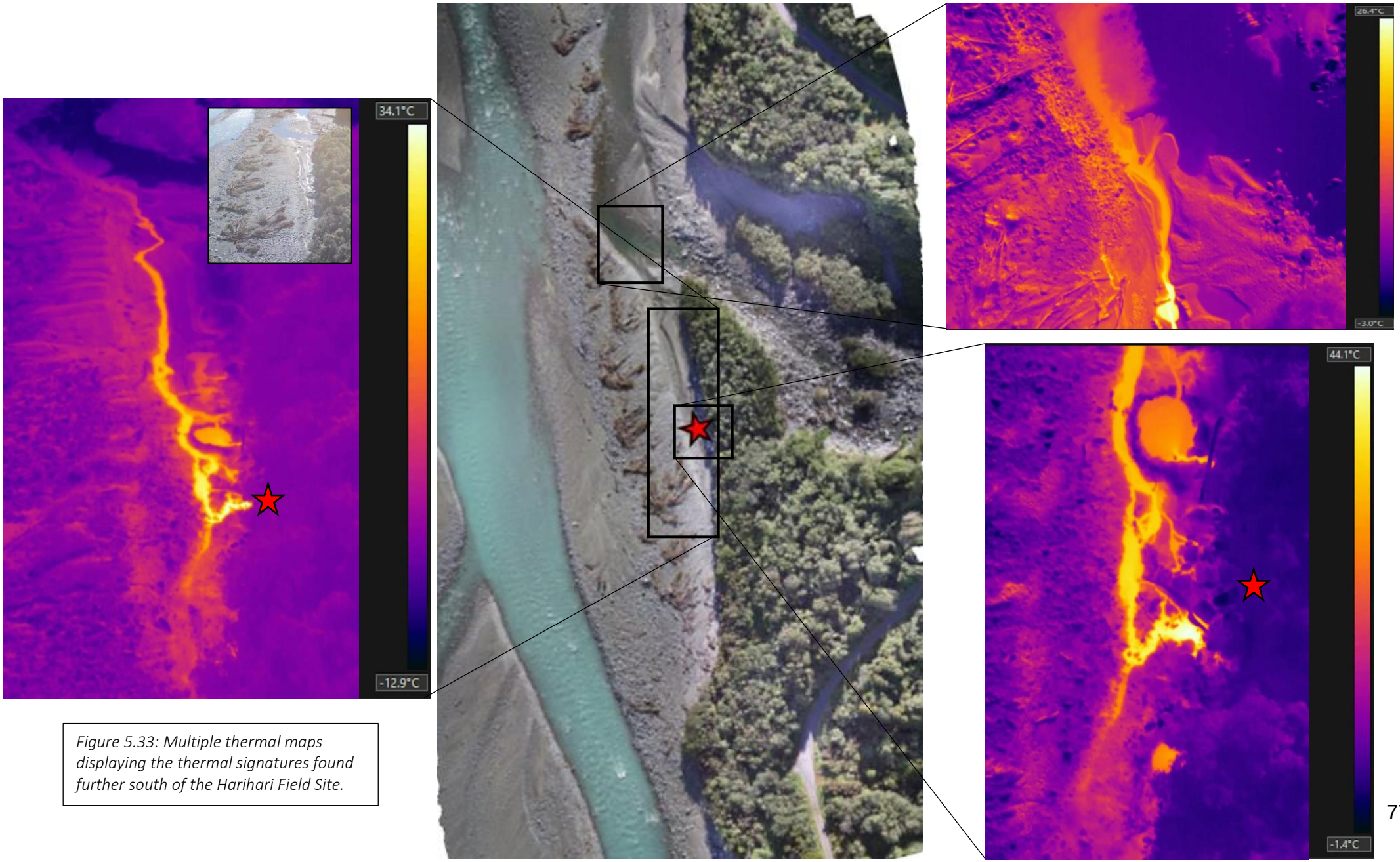

Figure 5.33: Multiple thermal maps displaying the thermal signatures found further south of the Harihari Field Site.

Figure 5.34: Photo of Amethyst hot springs further south of the Harihari Field Site. The steam can be seen rising.

Ilam: Model Data Analysis

The data analysis is done by splitting the full NDVI range into four quartiles for each site. This is done so for the four categories are split from min-low, low – med, med – high and high to max. By doing it this way the values are isolated into their respective group and closely re-examined and compared to the other three groups, these numbers are calculated using the model developed in chapter III which is derived from the field measurements.

All the statistics were calculated in python (pandas). The Ilam NDVI quartile intervals are:

I: -0.439-0.3689 [Min-Low]
II: 0.369-0.469 [Low-Med]
III: 0.470-0.5489 [Med-High]
IV: 0.549-0.924 [High-Max]

Table 5.1: Ilam NDVI Range Mean.

Ilam: NDVI Range Mean	**-0.439-0.924 [Min-Max]**			
Quartile Ranges	I	II	III	IV
CO_2 Flux	0.571	0.629	0.636	0.625
ST20	14.22	14.56	14.62	14.61
ST50	14.74	15.01	15.10	15.30
Surface Temp	6.12	5.75	5.75	6.10
NDVI	0.241	0.423	0.509	0.609
NDVI x1000	241	423	509	609
Count	2402	2389	2411	2410

As opposed to the Harihari study, with the Ilam fields data, as NDVI rises so too does soil temperature 50. CO_2 flux, soil temperature 20 drop off after III. The surface temperature does not follow suit with it dipping in II, III and rising again in IV.

Figure 5.35: Graph Ilam NDVI Range Mean.

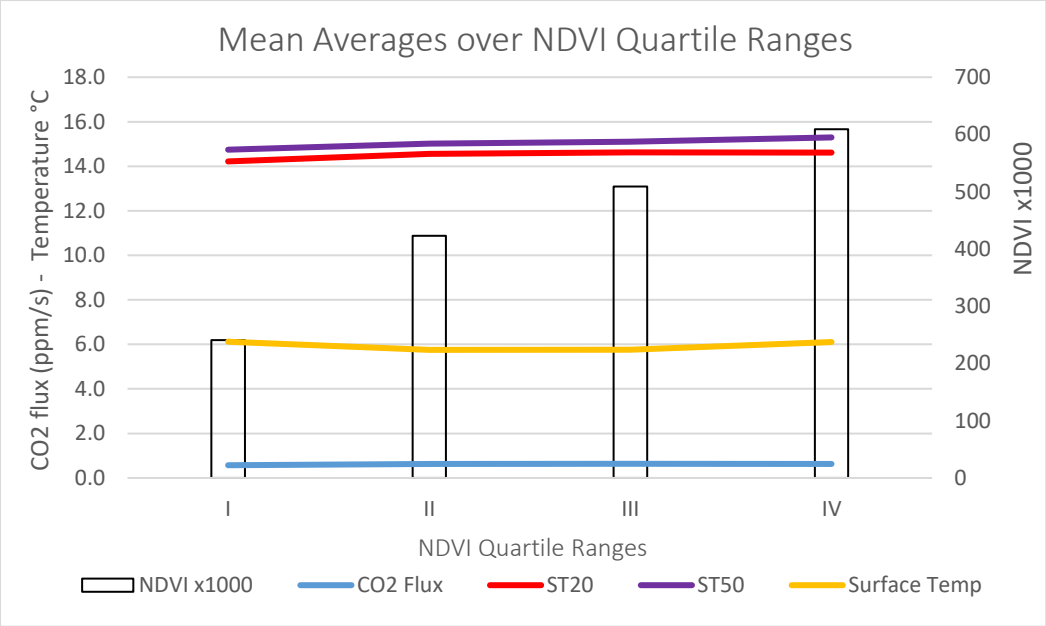

Similar to the point distribution using the average mean of all the points, but the following table and graph shows the median value (Q2).

Ilam: NDVI Range 50%	**-0.439-0.924 [Min-Max]**			
Quartile Ranges	I	II	III	IV
CO_2 Flux	0.591	0.626	0.638	0.622
ST20	14.15	14.55	14.57	14.41
ST50	14.73	15.30	15.43	15.50
Surface Temp	5.25	4.69	4.53	4.78
NDVI	0.277	0.425	0.509	0.599
NDVI x1000	277	425	509	599
Count	2402	2389	2411	2410

Table 5.11: Ilam NDVI Range 50%.

The mean and 50% tables share similar patterns with NDVI rising and CO_2 and soil temperature 50 following, and then flux, soil temperature 20 and surface temperature following the same patterns as the median table

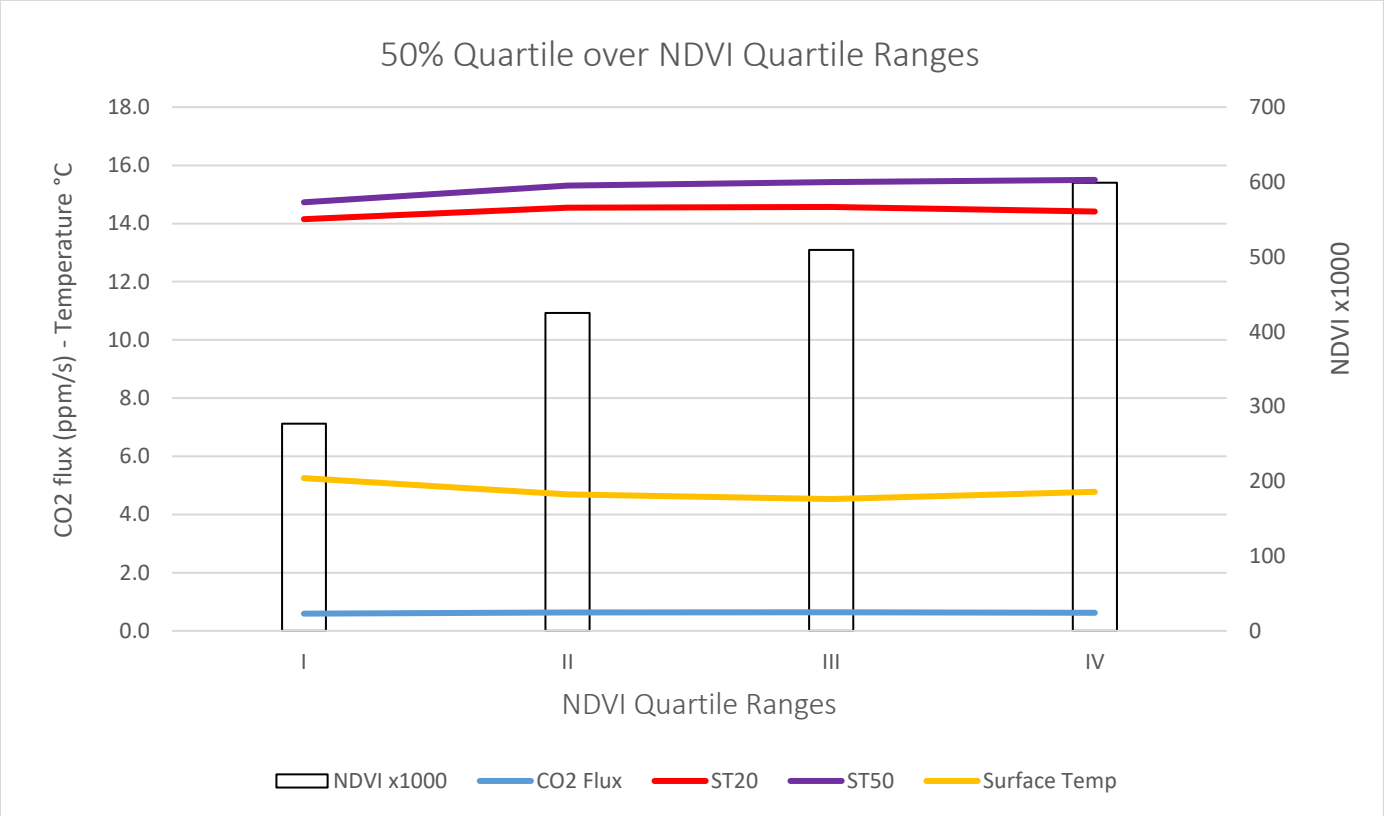

Figure 5.36: Graph Ilam NDVI Range 50%.

The table and graph below shows the standard deviation.

Ilam: NDVI Range Std	-0.439-0.924 [Min-Max]			
Quartile Ranges	I	II	III	IV
CO_2 Flux	0.195	0.200	0.199	0.182
ST20	0.91	0.80	0.78	0.78
ST50	0.94	1.07	1.06	0.92
Surface Temp	2.07	2.15	2.19	2.24
NDVI	0.119	0.029	0.023	0.047
NDVI x1000	119	29	23	47
Count	2402	2389	2411	2410

Table 5.12: Ilam NDVI Range Standard deviation.

The standard deviation appears to be consistent through the quartile ranges with NDVI spiking in I and IV. This is most likely to be caused by the absolute min and max values deviating far from the mean in the first quartile. Despite this, the standard deviation is lower compared to Harihari field site.

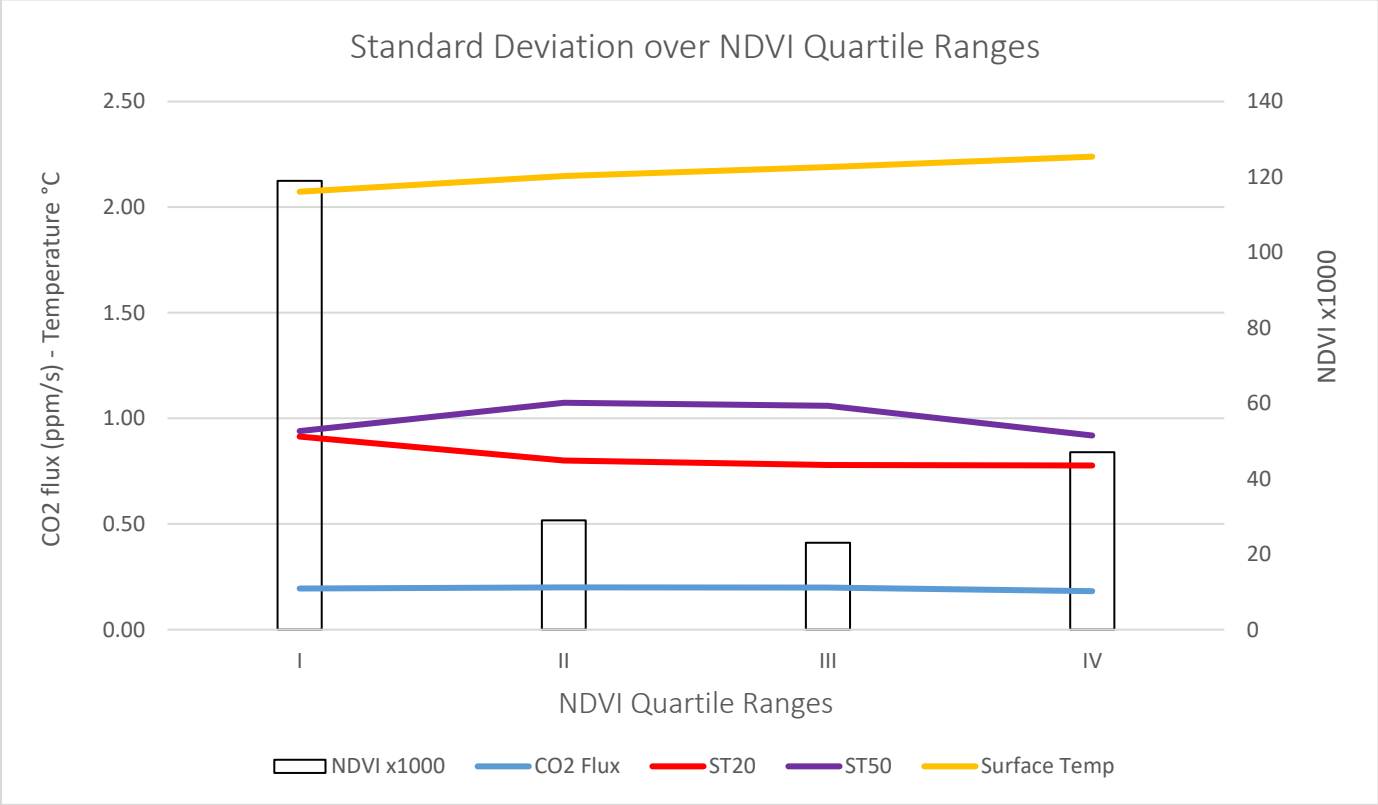

Figure 5.37: Graph Ilam NDVI Range Standard Deviation.

The table and graph below shows the calculated statistics of all points (9000+).

Ilam: NDVI Complete	**-0.439-0.924 [Min-Max] Complete Data Set**						
Stats	Mean	Std	Min	25%	50%	75%	Max
CO_2 Flux	0.615	0.196	0.213	0.493	0.620	0.727	1.147
ST20	14.50	0.84	12.66	13.99	14.43	15.03	16.62
ST50	15.04	1.02	11.54	14.33	15.30	15.77	16.70
Surface Temp	5.93	2.17	3.50	4.26	4.84	8.03	10.54
NDVI	0.446	0.151	-0.439	0.369	0.470	0.549	0.924
NDVI x1000	446	151	-439	369	470	549	924
Count	9648						

Table 5.13: Ilam NDVI Complete data set.

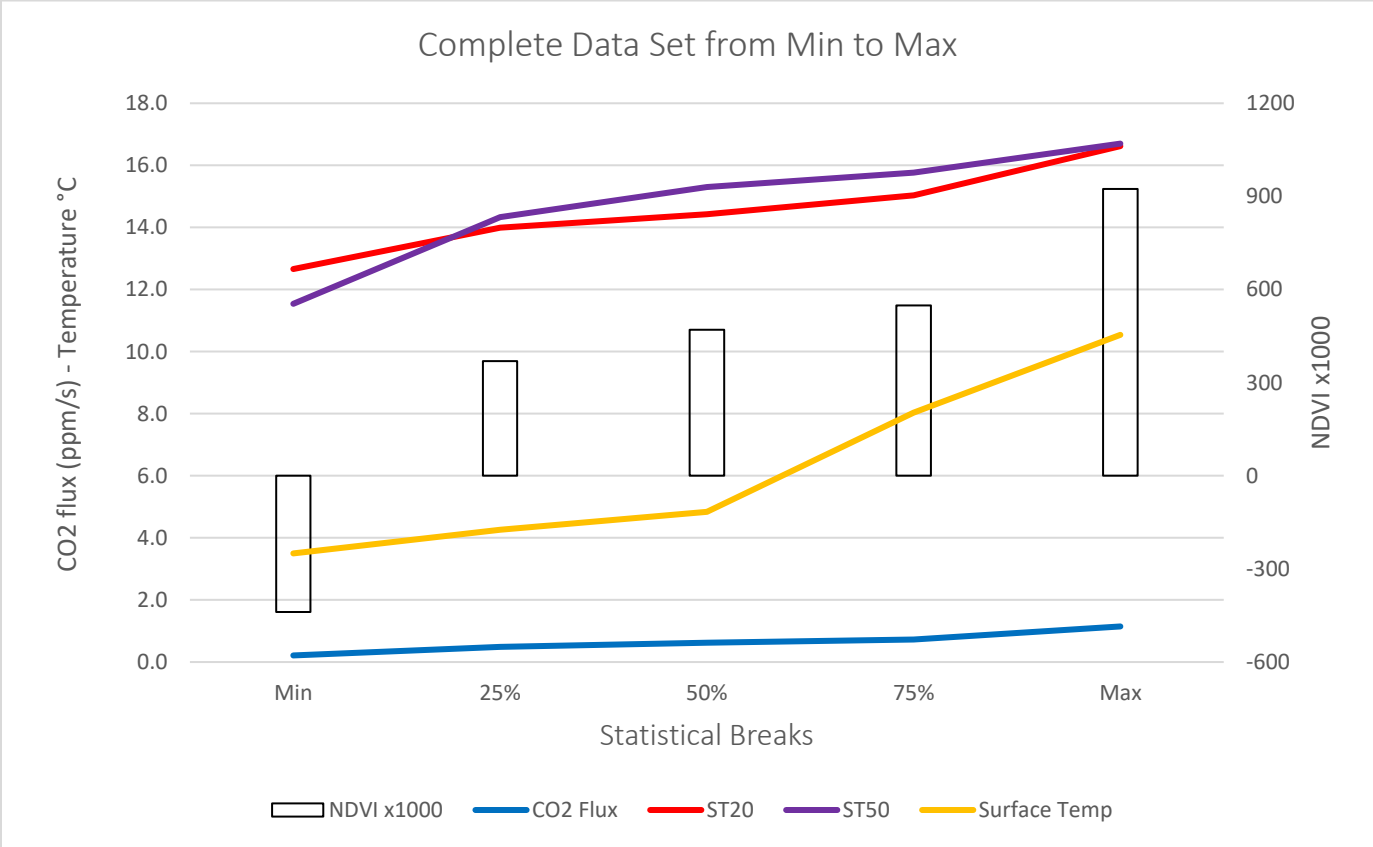

Figure 5.38: Graph Ilam NDVI Complete data set.

A graph from only the 52 sampled sites in Ilam fields, yields the triple axis graphs below

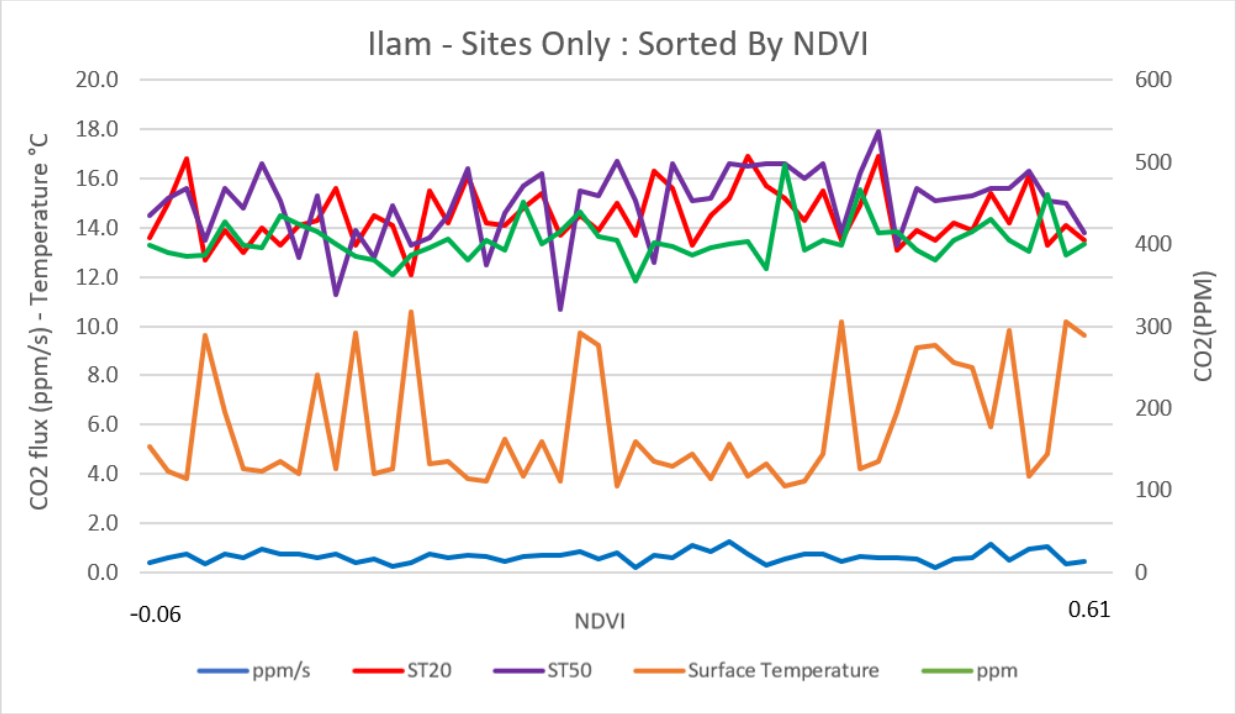

Figure 5.39: Triple axis graph shows fluctuations in field stats as NDVI Rises in Ilam.

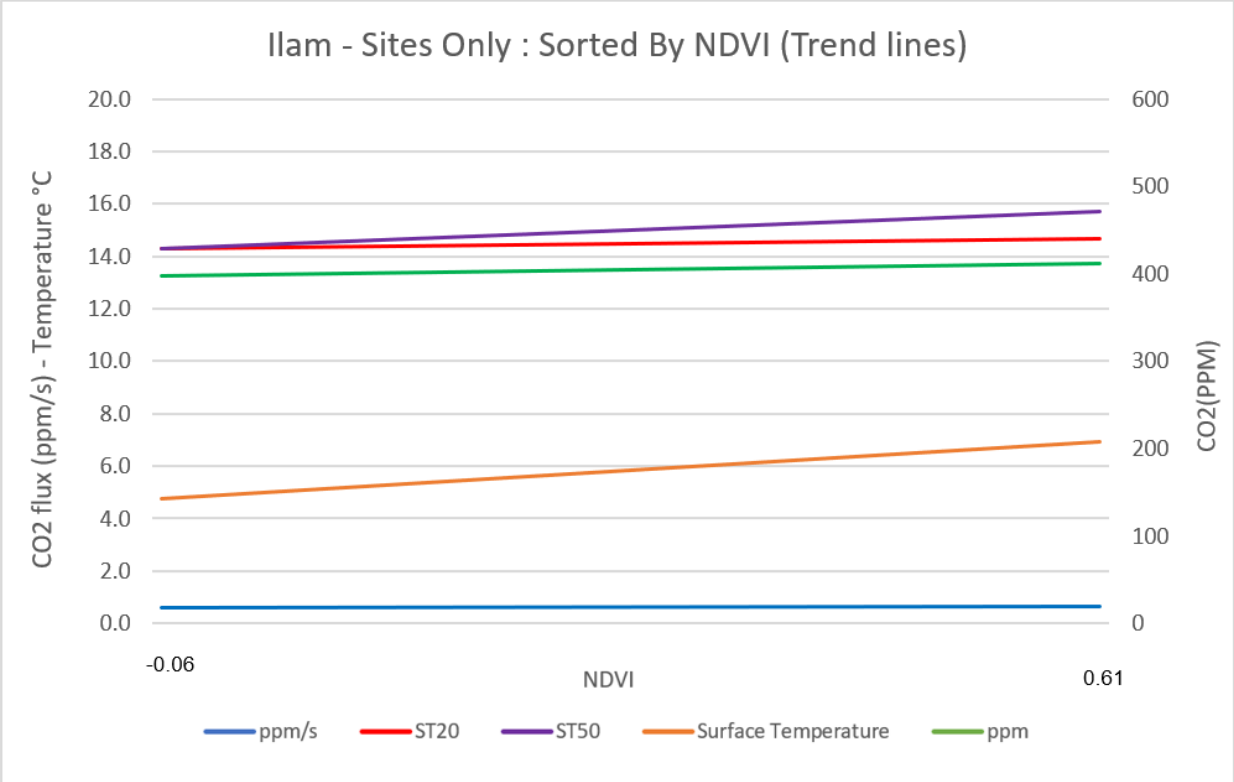

Figure 5.4: Triple axis graph shows trendlines in field stats as NDVI Rises in Ilam Fields.

Harihari: Model Data Analysis

The NDVI quartile intervals in Harihari are:

I: -0.579-0.2759 [Min-Low]
II: 0.276-0.4019 [Low-Med]
III: 0.402-0.5079 [Med-High]
IV: 0.508-0.929 [High-Max]

Count refers to number of generated points, NDVI x1000 is NDVI scaled up by x 1000 to fit the second axis.

Harihari: NDVI Range Mean	**-0.579-0.929 [Min-Max]**			
Stats	I	II	III	IV
CO_2 Flux	0.796	0.766	0.757	0.913
ST20	12.17	12.16	12.17	12.34
ST50	13.25	13.22	13.18	13.21
Surface Temp	5.63	5.69	5.71	5.80
NDVI	0.128	0.343	0.456	0.598
NDVI x1000	128	343	456	598
Count	2396	2416	2402	2419

Table 5.14: Harihari NDVI Range Mean.

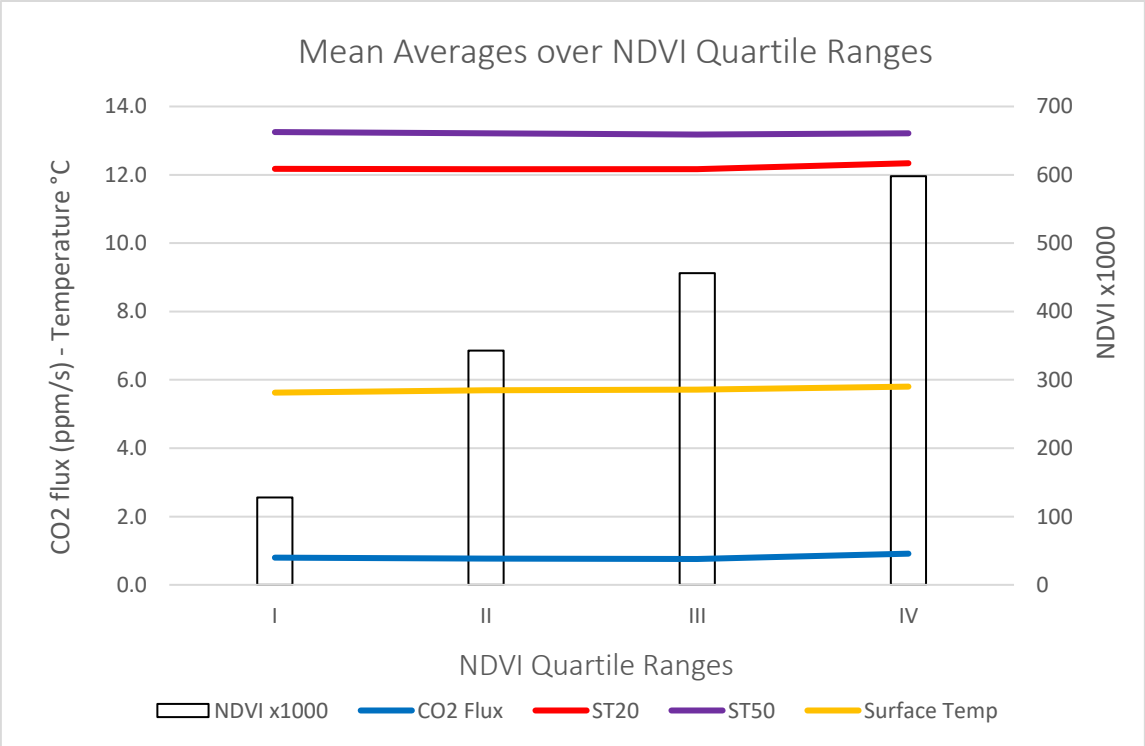

Figure 5.41: Harihari Ilam NDVI Range Mean.

The following table and graph shows the median value (Q2).

Harihari: NDVI Range 50%	-0.579-0.929 [Min-Max]			
Quartile Ranges	I	II	III	IV
CO_2 Flux	0.700	0.670	0.662	0.752
ST20	12.22	12.18	12.17	12.28
ST50	13.17	13.14	13.13	13.17
Surface Temp	5.77	5.80	5.80	6.00
NDVI	0.162	0.346	0.457	0.578
NDVI x1000	162	346	457	578
Count	2396	2416	2402	2419

Table 5.15: Harihari NDVI Range 50%.

Similar to the mean quartile table above. The median table displays a dip from I to II and III and then increases to the highs in IV.

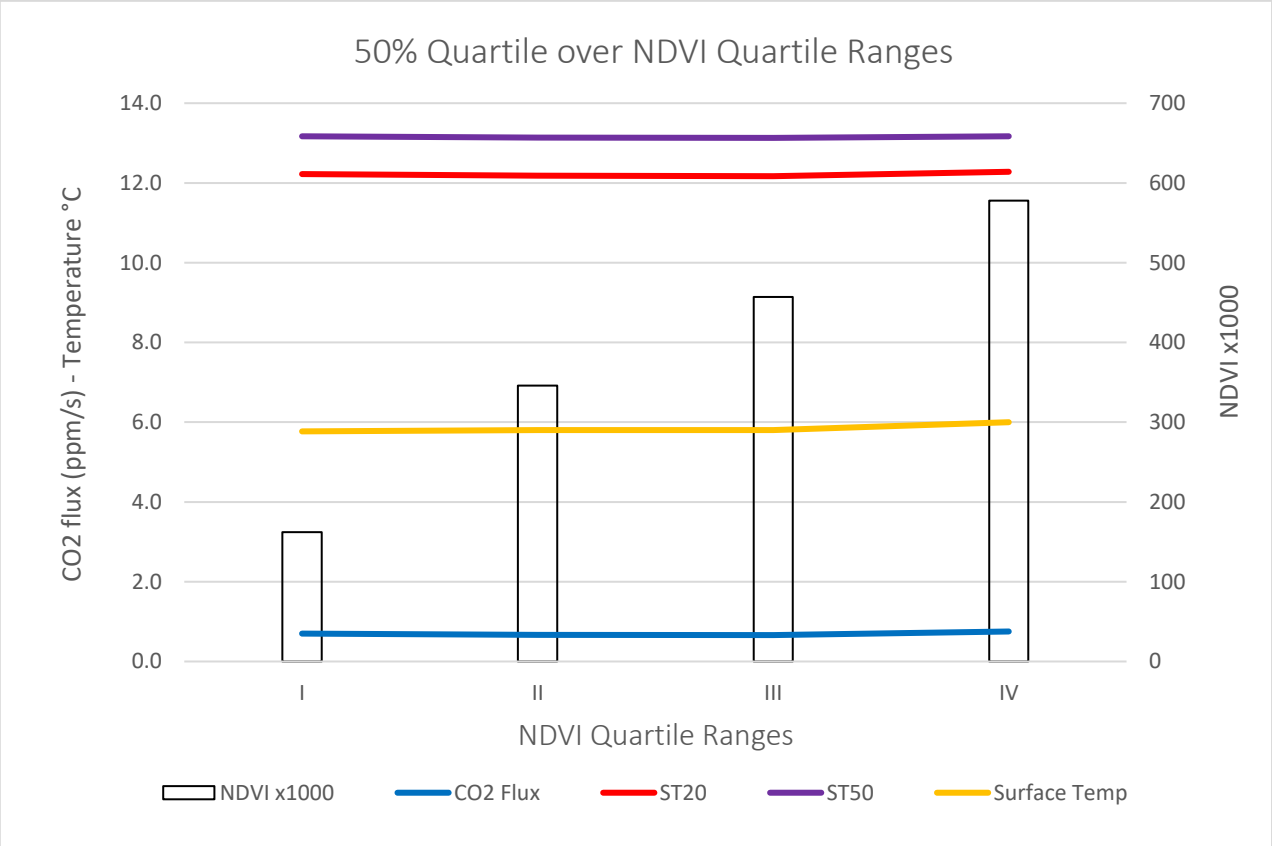

Figure 5.42: Graph Harihari NDVI Range 50%.

The table and graph below shows the standard deviation.

Harihari: NDVI Range Std	**-0.579-0.929 [Min-Max]**			
Quartile Ranges	I	II	III	IV
CO_2 Flux	0.324	0.352	0.375	0.461
ST20	0.31	0.30	0.34	0.43
ST50	0.48	0.48	0.46	0.39
Surface Temp	0.47	0.46	0.46	0.46
NDVI	0.130	0.036	0.030	0.074
NDVI x1000	130	36	30	74
Count	2396	2416	2402	2419

Table 5.16: Harihari NDVI Range Standard Deviation.

The standard deviation appears to be consistent through the quartile ranges with NDVI spiking in I and IV. This is most likely to be caused by the absolute min and max values deviating far from the mean.

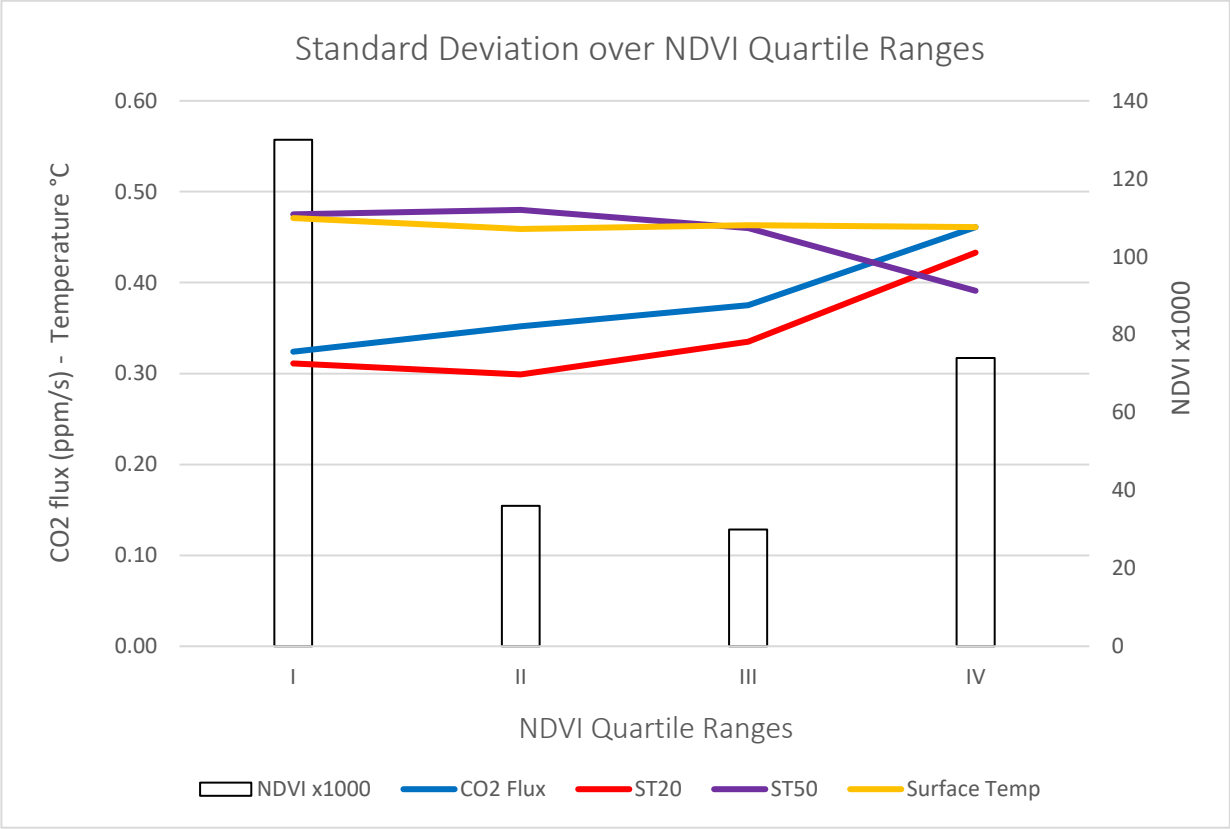

Figure 5.43: Graph Harihari NDVI Complete data.

The table and graph below shows the calculated statistics of all points (9000+)

Harihari: NDVI Complete	**-0.579-0.929 [Min-Max] Complete Data Set**						
Stats	Mean	Std	Min	25%	50%	75%	Max
CO_2 Flux	0.808	0.386	0.148	0.548	0.683	1.037	2.018
ST20	12.21	0.36	11.36	11.98	12.22	12.45	13.15
ST50	13.22	0.45	12.40	12.77	13.16	13.50	14.46
Surface Temp	5.71	0.47	4.20	5.43	5.83	6.03	6.37
NDVI	0.382	0.189	-0.579	0.276	0.402	0.508	0.929
NDVI x1000	382	189	-579	276	402	508	929
Count	9633						

Table 5.17: Harihari NDVI Complete data.

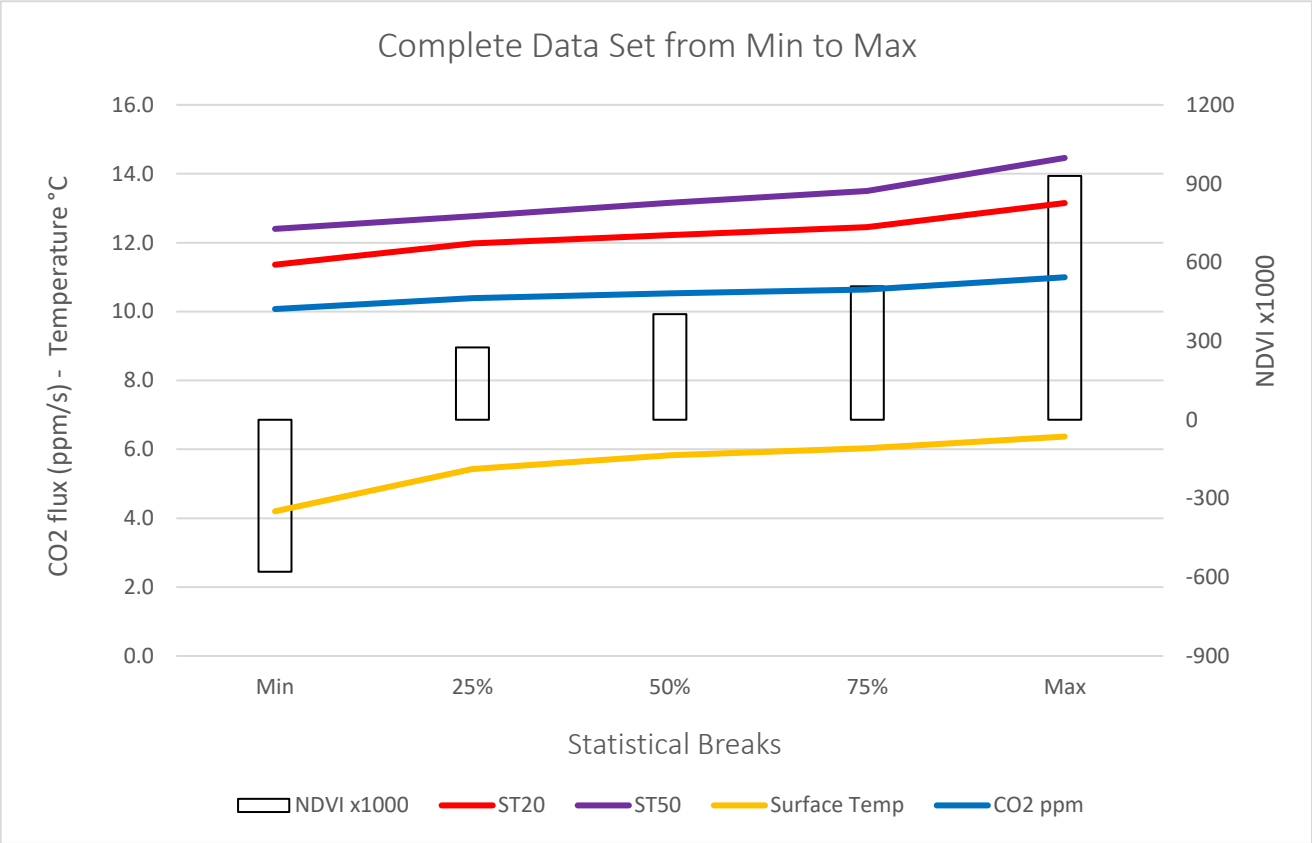

Figure 5.44: Graph Harihari NDVI Complete data.

When isolating the points, the trends become slightly easier to see. The triple axis graph is sorted from the lowest NDVI value to the highest.

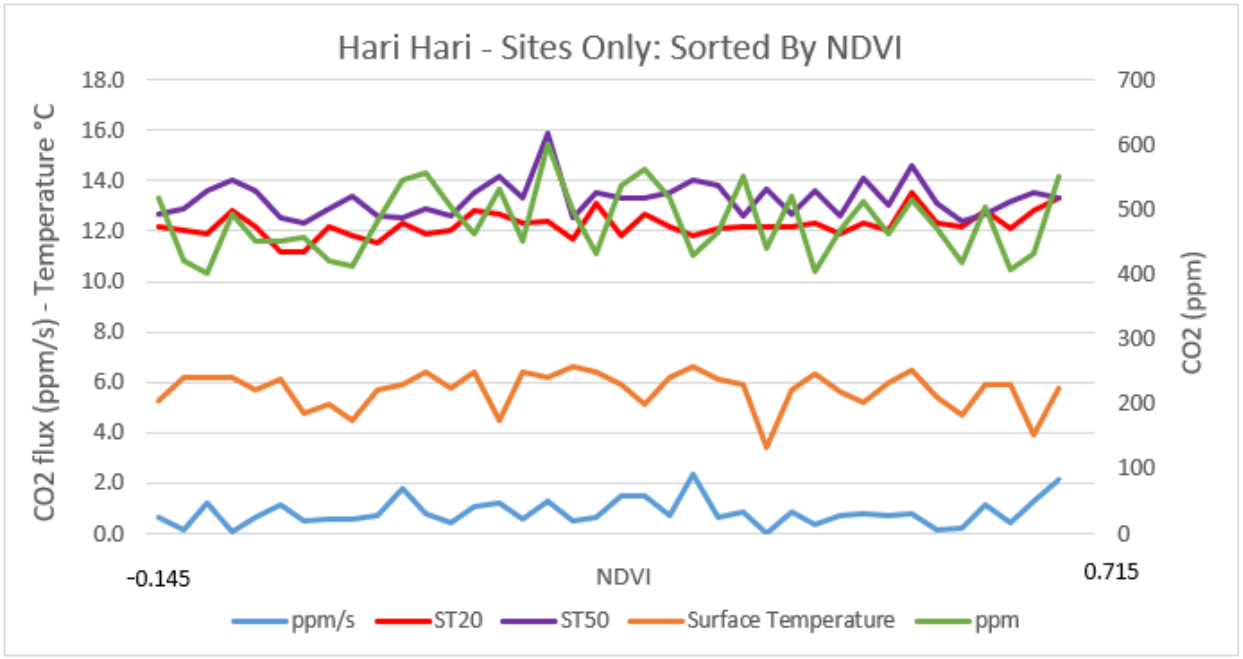

Figure 5.45: Triple axis graph shows fluctuations in field stats as NDVI Rises in Harihari.

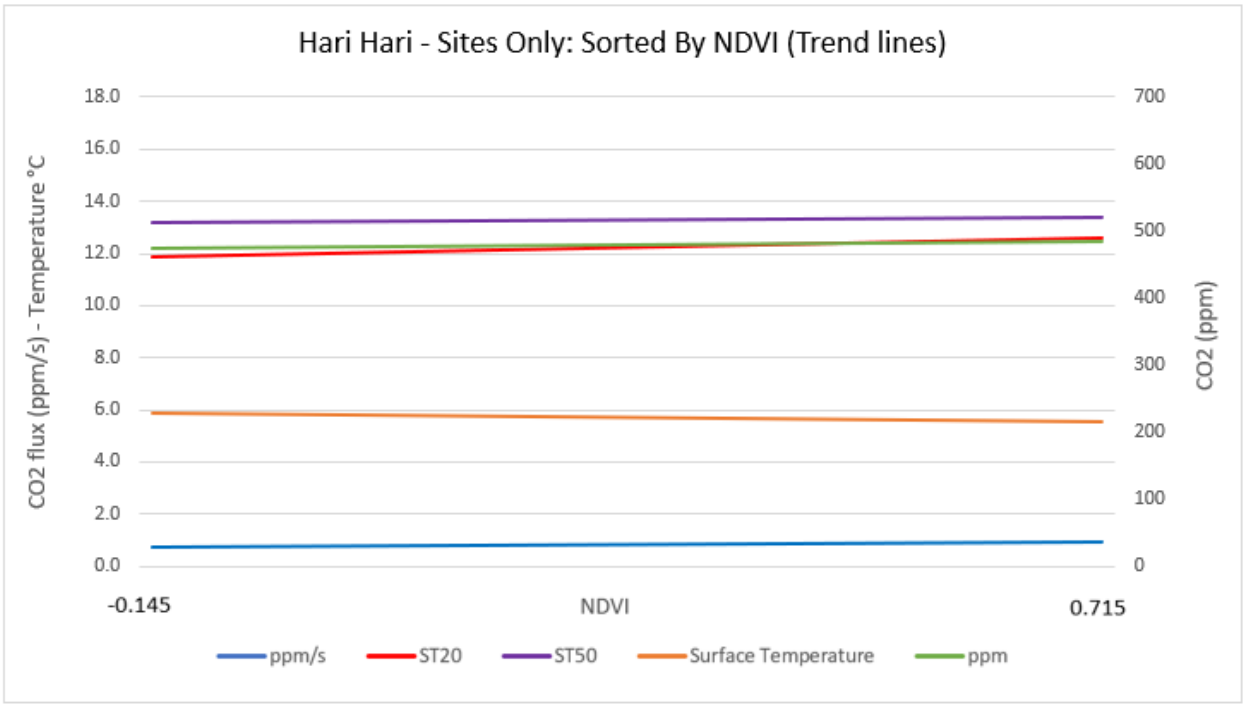

Figure 5.46: Triple axis graph shows trend lines in field stats as NDVI Rises in Harihari.

Ilam and Harihari Box and Whisker Graphs

The 10 graphs below compare Ilam and Harihari field variables box and whisker graphs with their respective standard deviation graphs from the model data developed in arcGIS. Note red line refers to the mean value.

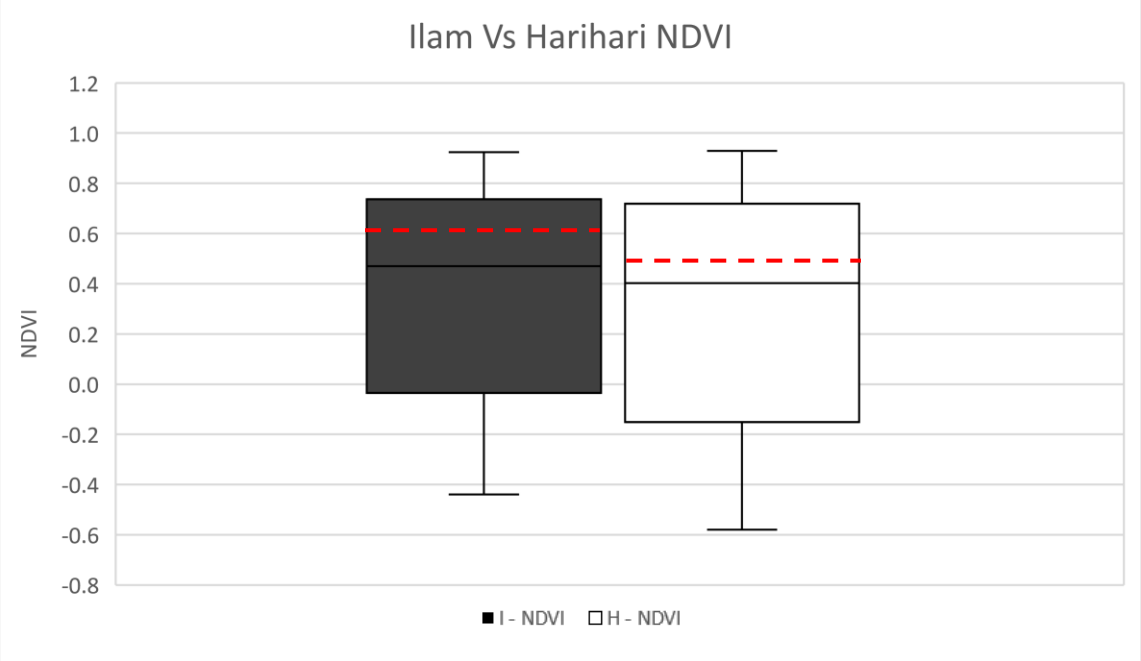

Figure 5.47: Ilam Vs Harihari NDVI box and whisker comparison

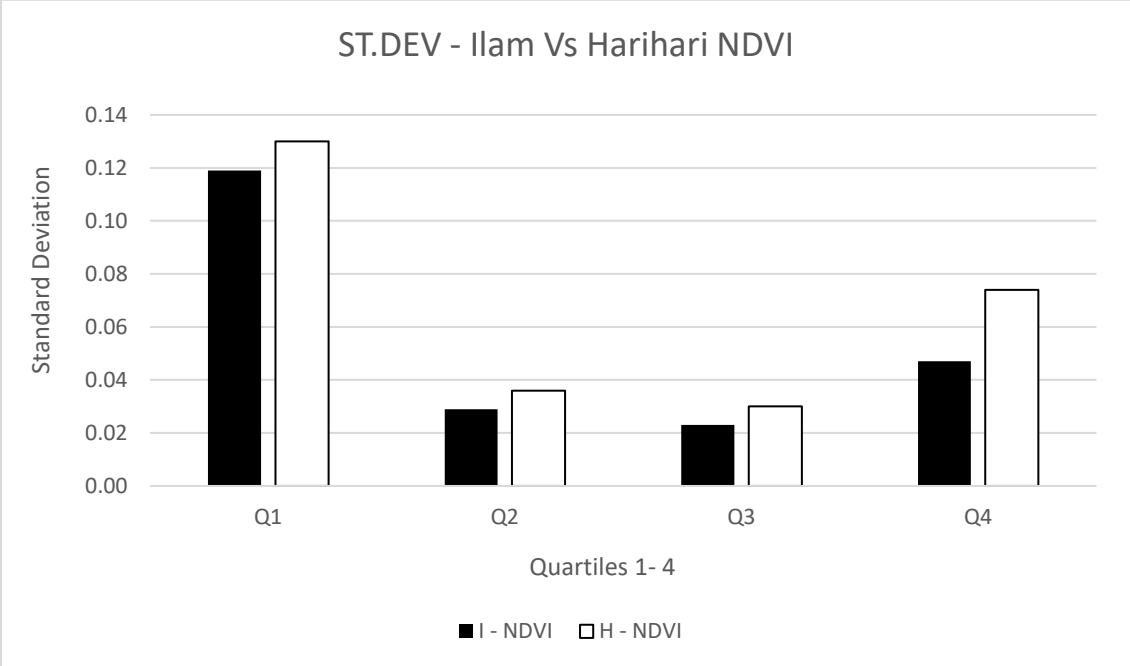

Figure 5.48: Ilam Vs Harihari NDVI standard deviation comparison

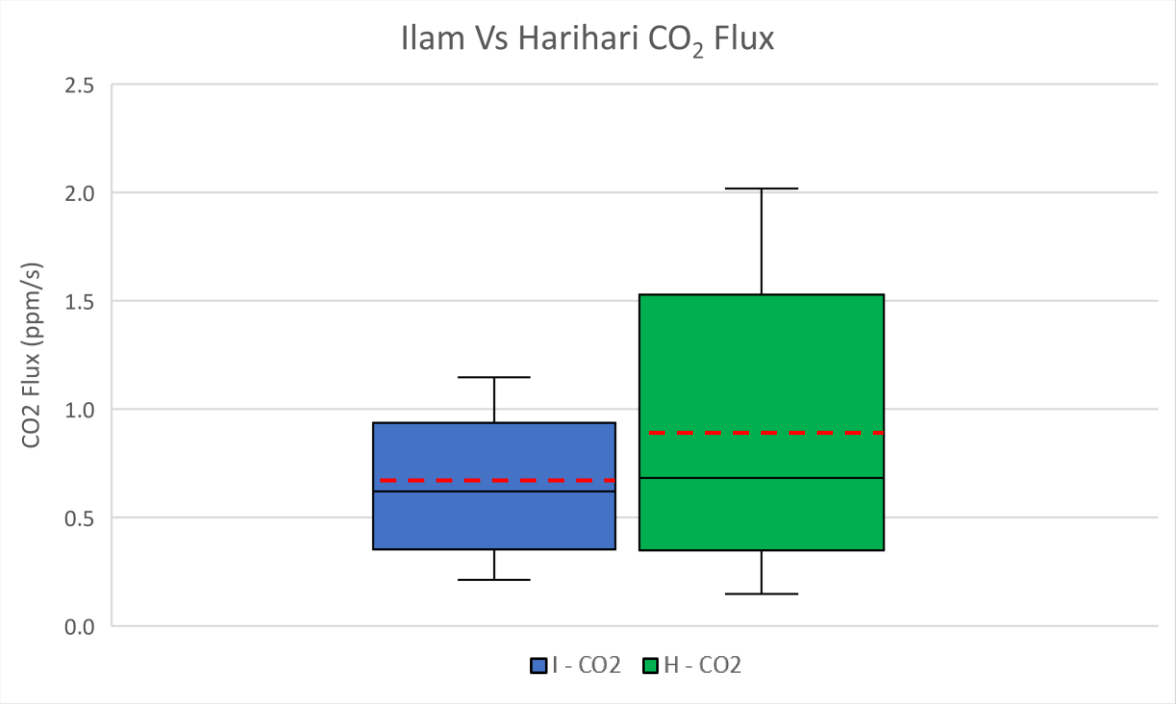

Figure 5.49: Ilam Vs Harihari CO_2 flux box and whisker comparison

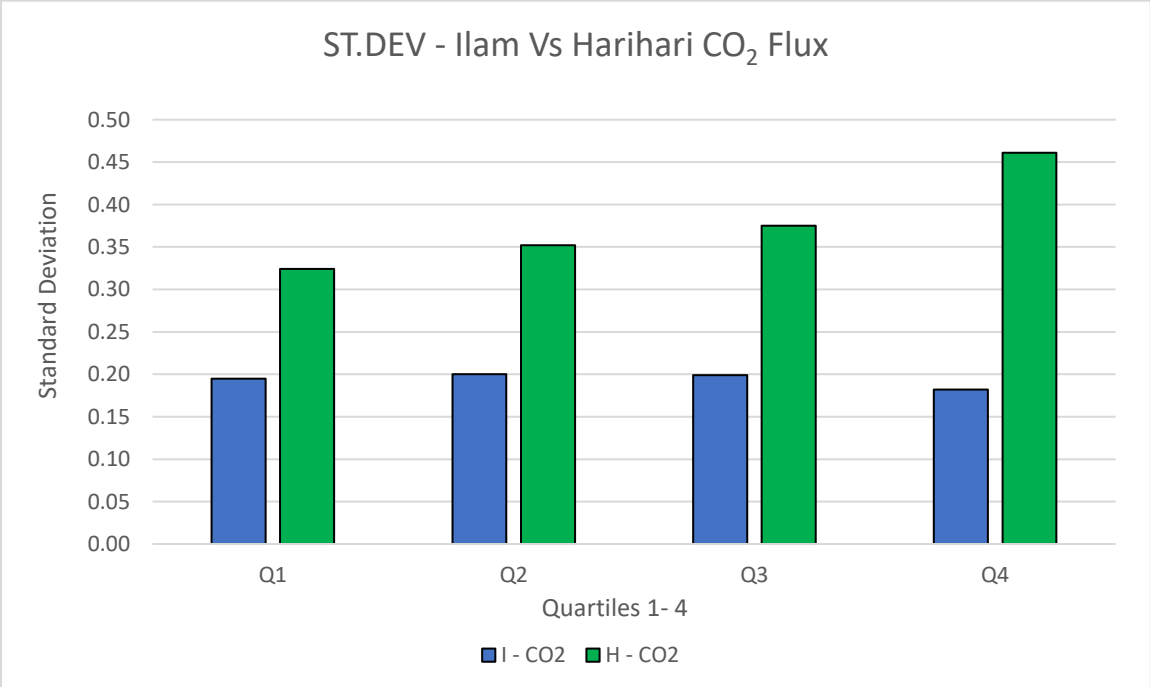

Figure 5.5: Ilam Vs Harihari CO_2 flux standard deviation comparison

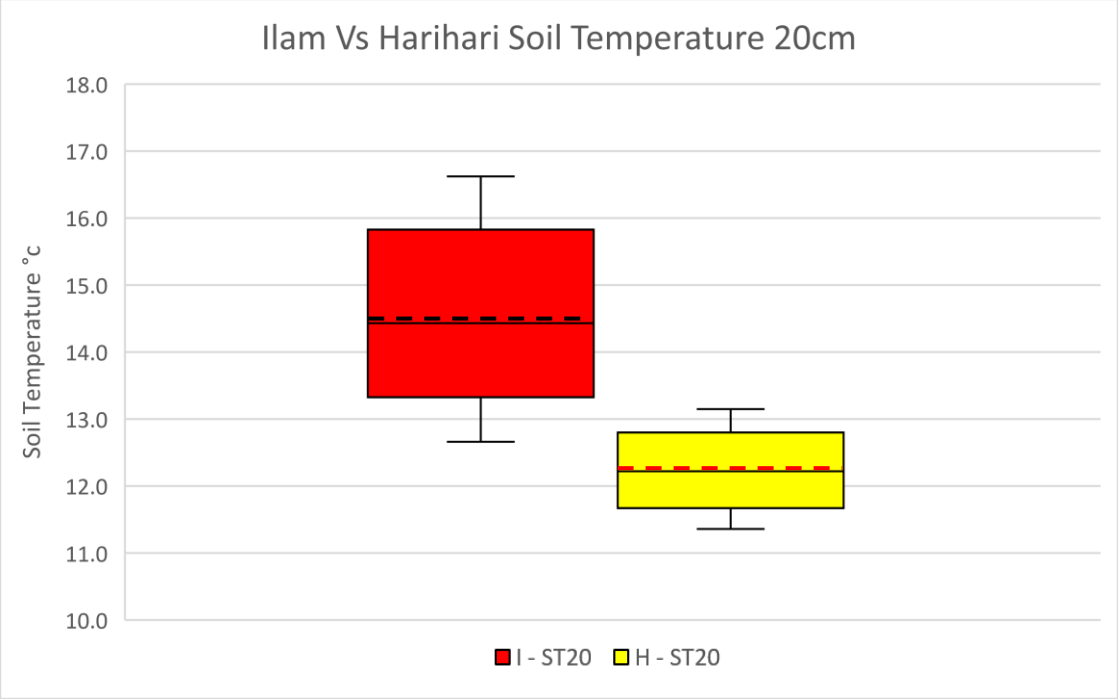

Figure 5.51: Ilam Vs Harihari soil temperature 20cm box and whisker comparison

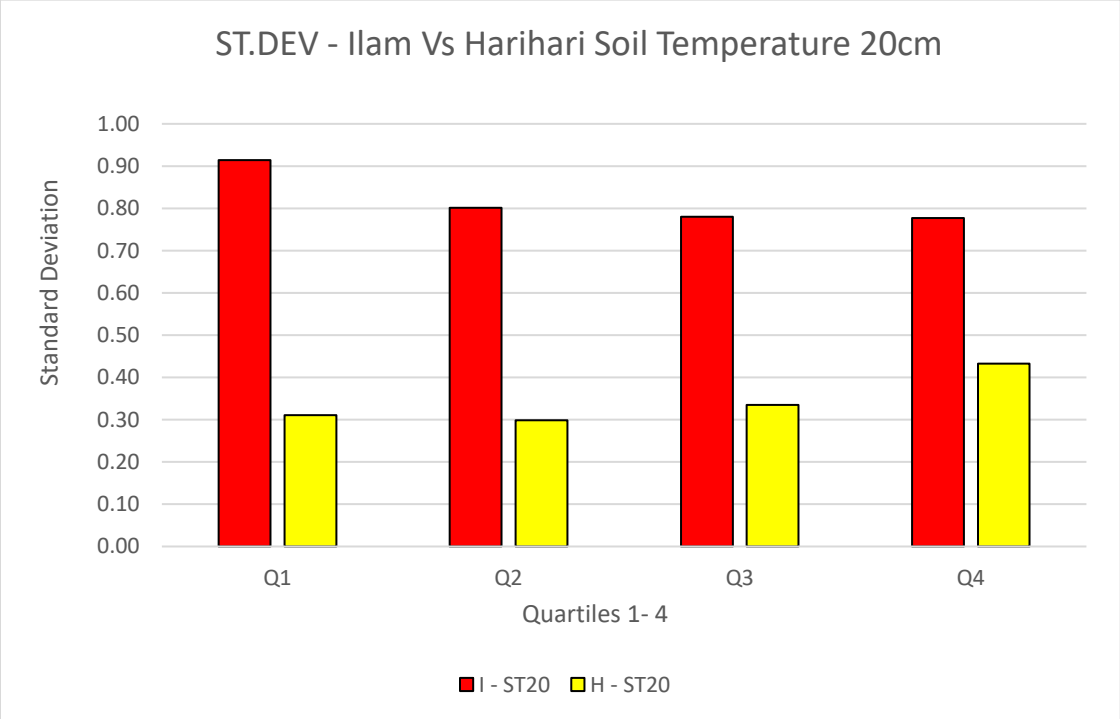

Figure 5.52: Ilam Vs Harihari soil temperature 20cm standard deviation comparison

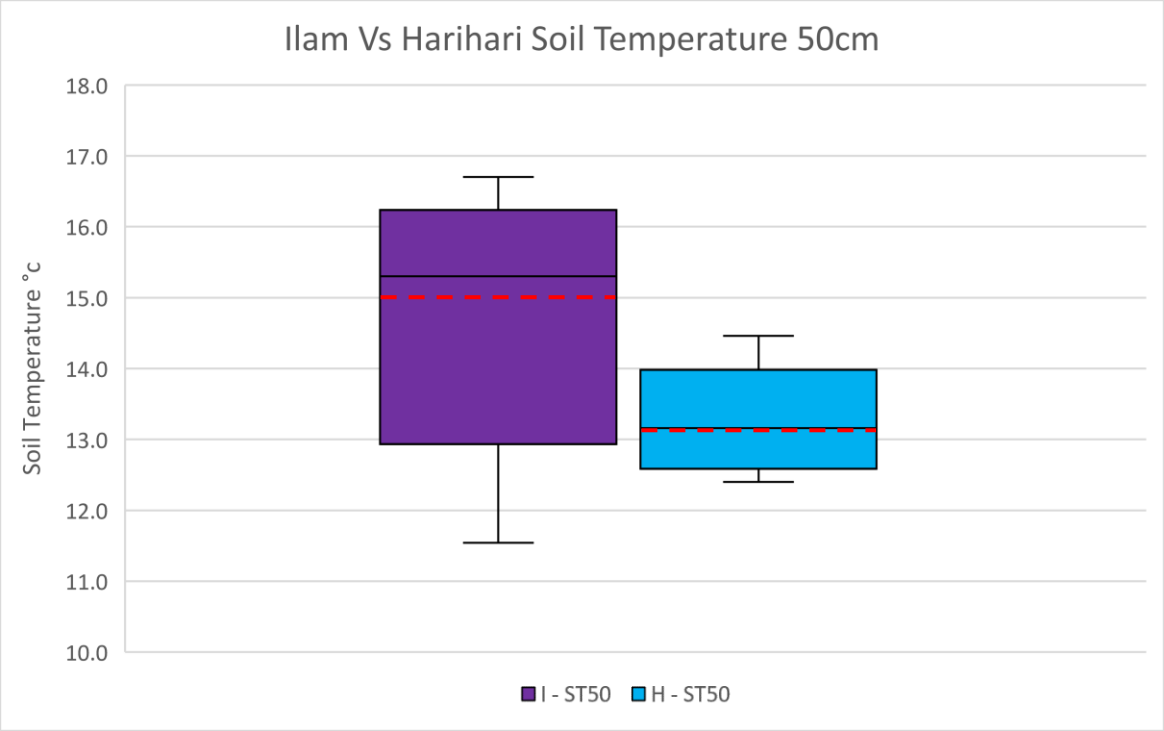

Figure 5.53: Ilam Vs Harihari soil temperature 50cm box and whisker comparison

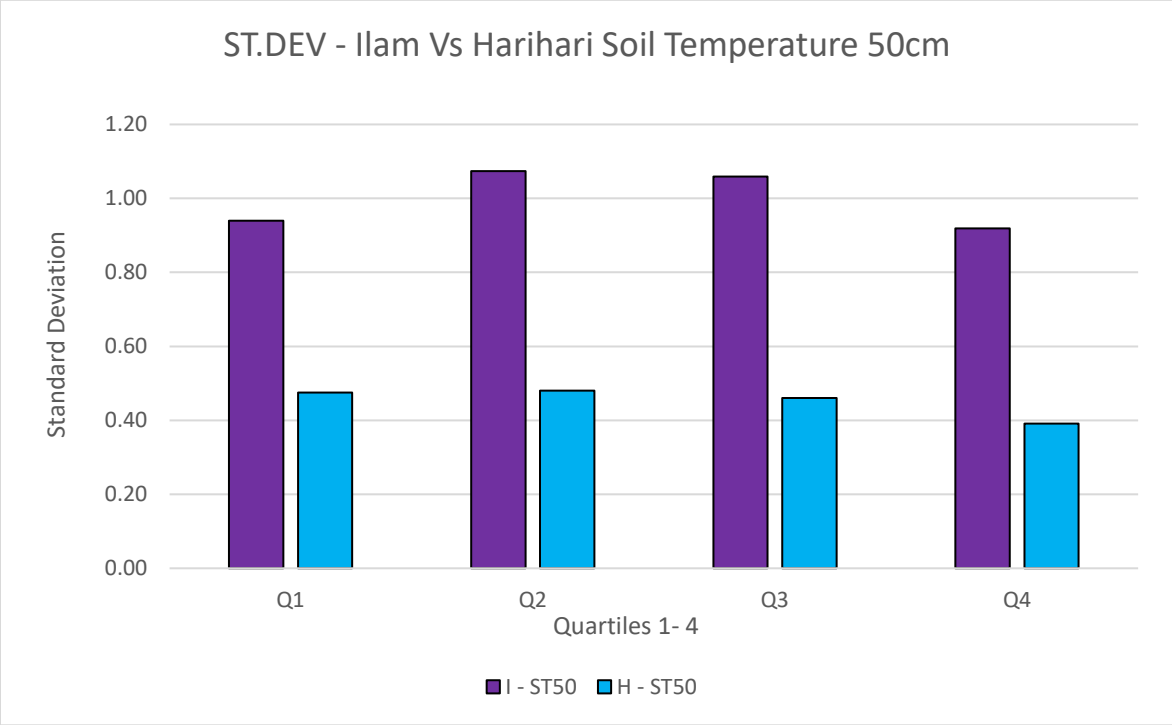

Figure 5.54: Ilam Vs Harihari soil temperature 50cm standard deviation comparison

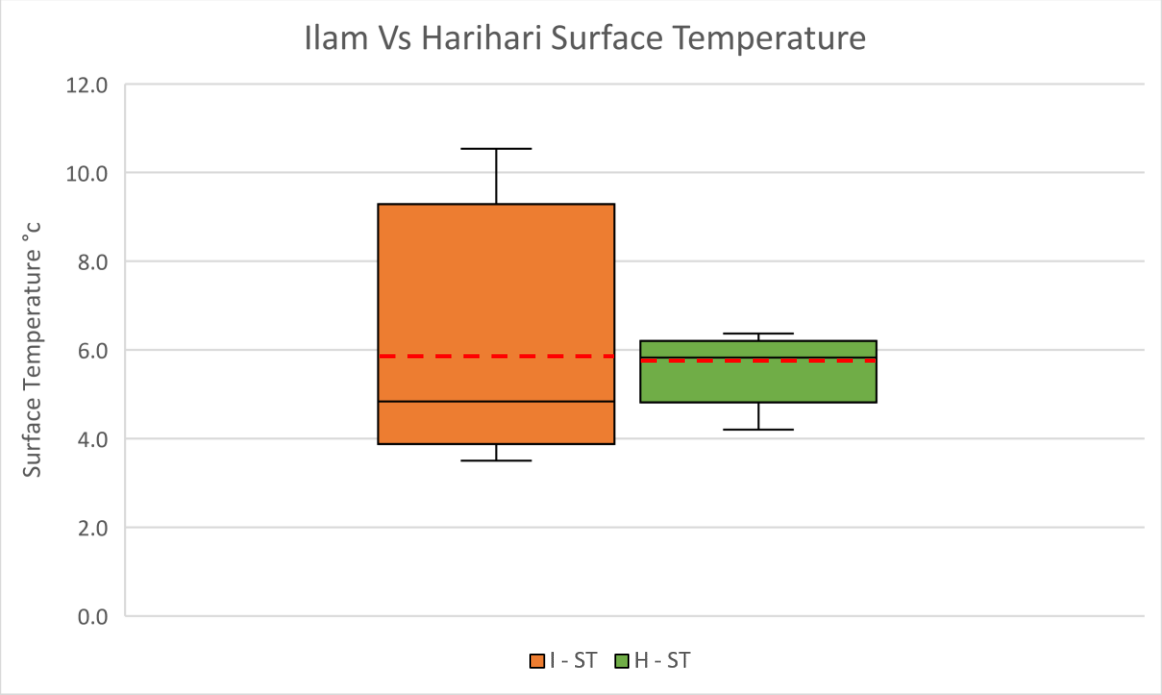

Figure 5.55: Ilam Vs Harihari surface temperature box and whisker comparison

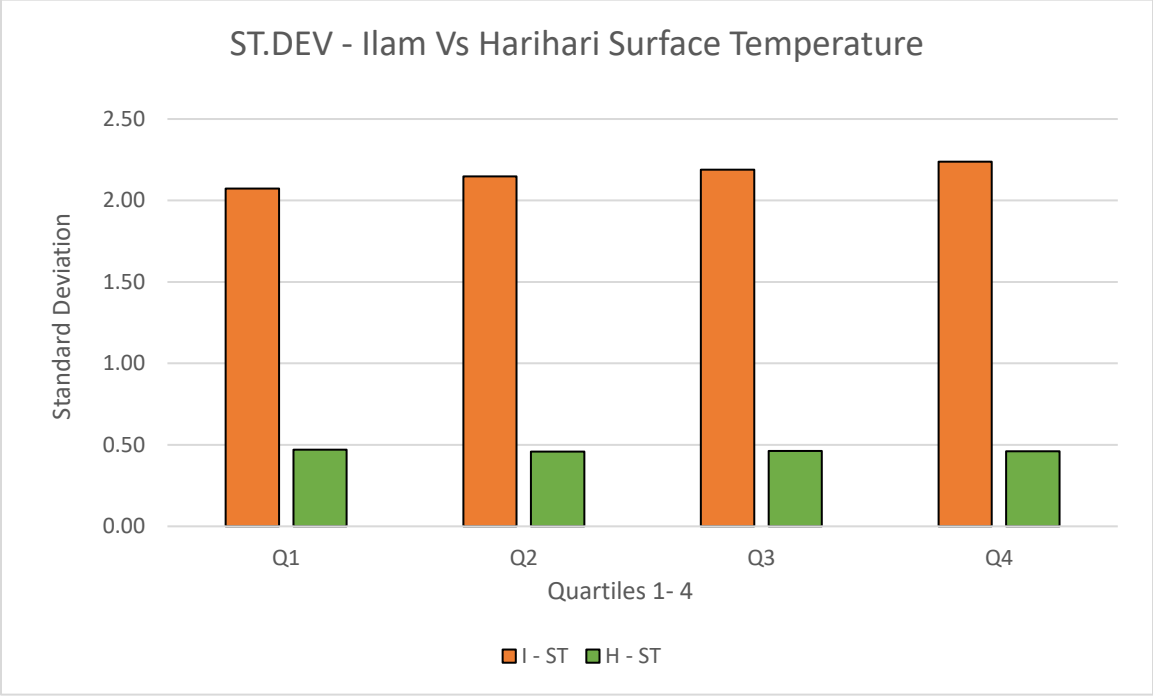

Figure 5.56: Ilam Vs Harihari surface temperature standard deviation comparison

Statistical Probability Analysis

Probability testing is best used when comparing two of the same variables, in this case Harihari and Ilam fields are not similar, however probability analysis was still done. The tables below show an Analysis of Variance (ANOVA) and T-test which compares two means eg, Ilam NDVI and Harihari NDVI etc.

These values were calculated in excel.

SS = Sum of Squares
DF = Degrees of Freedom
MS = Mean Square
F = F value
P value = Probability
F = Critical Value / F Ratio
Level of Significance (alpha) = 0.05 (5%)

NDVI						
Groups	*Count*	*Sum*	*Average*	*Variance*		
Ilam - NDVI	51	20.19	0.396	0.023		
Harihari - NDVI	38	12.38	0.326	0.049		
ANOVA						
Source of Variation	*SS*	*df*	*MS*	*F*	*P-value*	*F crit*
Between Groups	0.107	1	0.107	3.134	0.080	3.951
Within Groups	2.968	87	0.034			
Total	3.075	88				
P-Value from T-Test	0.08019					

Table 5.18: NDVI probability values derived from one-way ANOVA and T-test

CO_2 Flux						
Groups	*Count*	*Sum*	*Average*	*Variance*		
Ilam – CO_2 Flux	38	31.403	0.826	0.285		
Harihari - CO_2 Flux	51	31.822	0.624	0.052		
ANOVA						
Source of Variation	*SS*	*df*	*MS*	*F*	*P-value*	*F crit*
Between Groups	0.892	1	0.892	5.920	0.017	3.951
Within Groups	13.113	87	0.151			
Total	14.005	88				
P-Value from T-Test	0.017013					

Table 5.19: CO_2 flux probability values derived from one-way ANOVA and T-test

Soil Temperature 20cm						
Groups	*Count*	*Sum*	*Average*	*Variance*		
Ilam - ST20	38	464.9	12.234	0.252		
Harihari - ST20	51	738.4	14.478	1.224		
ANOVA						
Source of Variation	*SS*	*df*	*MS*	*F*	*P-value*	*F crit*
Between Groups	109.672	1	109.672	135.317	2.05E-19	3.951
Within Groups	70.512	87	0.810			
Total	180.184	88				
P-Value from T-Test	2.05E-19					

Table 5.2: Soil temperature at 20cm probability values derived from one-way ANOVA and T-test

Soil Temperature 50cm						
Groups	*Count*	*Sum*	*Average*	*Variance*		
Ilam - ST50	38	504.4	13.274	0.516		
Harihari - ST50	51	764.2	14.984	2.161		
ANOVA						
Source of Variation	*SS*	*df*	*MS*	*F*	*P-value*	*F crit*
Between Groups	63.720	1	63.720	43.595	3.06E-09	3.951
Within Groups	127.161	87	1.462			
Total	190.881	88				
P-Value from T-Test	3.06E-09					

Table 5.21: Soil temperature at 50cm probability values derived from one-way ANOVA and T-test

Surface Temperature						
Groups	*Count*	*Sum*	*Average*	*Variance*		
Ilam - ST	38	216.5	5.697	0.565		
Harihari - ST	51	296.6	5.816	5.540		
ANOVA						
Source of Variation	*SS*	*df*	*MS*	*F*	*P-value*	*F crit*
Between Groups	0.305	1	0.305	0.089	0.766	3.951
Within Groups	297.917	87	3.424			
Total	298.222	88				
P-Value from T-Test	0.766138					

Table 5.22: Surface temperature probability values derived from one-way ANOVA and T-test

VI. DISCUSSION

The South Island of New Zealand contains numerous low enthalpy geothermal systems associated with the Alpine Fault Zone (Hansen, M., 2015). However, locating geothermal activity proves elusive where there are no obvious products of geothermal activity present at the surface, such as: hot springs, fumaroles, geysers, landslides, subsidence, geothermal alteration, steam and other such manifestations. Nevertheless, through the use of infrared imaging, thermal imaging and field surveying, hydrothermal fluids at depth are detectable; as found under the cliff edge and the swamp in Harihari.

As part of the process of locating hidden geothermal systems, determining that spikes in CO_2 flux and soil and surface temperatures are actually the results of geothermal activity and not merely the results of other sources, such as biogenic influences, is paramount. Concerning the Harihari field, it was hypothesized that the active geothermal system hidden under the surface could be detected through the measuring of certain variables (soil and surface temperature, CO_2 flux). The variables measured throughout the survey suggested that where anomalous spikes in the field variables occurred it was a direct result of the underlying geothermal activity.

In general, the anomalous spikes in these measurements occur very close to each other and even overlap (spatially), suggest this is evidence that there is a detectable geothermal resource hidden below. This discovery provides a good starting point in developing new methodology and practices for more effectively and accurately identifying the location of blind geothermal systems.

Field Data Summary

The Ilam and Harihari fields presented contrasting landscapes that were ideal for the carrying out of this survey; there were a number of similarities and differences between the two sites that were essential to obtaining meaningful data.

The main difference between Ilam fields and Harihari was the actual field site itself. Specifically, the vegetation present in each field differed significantly. Ilam fields is homogeneously covered with grass and is managed as an actively used recreational area that hosts activities including sports and musical events. Whereas, the Harihari field site is an un-grazed field that is made up of long grass, docks, sorrel, rushes and creeping buttercup, surrounded by native conifer-podocarp forest. The terrace is very poorly sorted and coarse grained. The lower banks that bordered the field, are made up of river deposits ranging from bare coarse sand to cobbles.

Another difference between the sites was that because the field used in Harihari was the back-up site from the originally intended study site, a different setup was required for each field. The original study site in Harihari was an elongated terrace (>300 metres) that ran parallel closest to the hot spring; however, it was eroded weeks before the team could commence field data collection (figure 5.17). In response to this event the study site at Harihari was moved further inland however, this meant that the new smaller field site would not be suitable for the longer transect survey, as done in Ilam fields (>350m), and thus a grid style survey was used as the next best option (~150m). The use of grids and transects still did a great job of showing the spatial variation of recorded field data.

From the initial surveys, both Ilam and Harihari field sites showed that where NDVI values fluctuated the sampled variables behaved in a similar way; higher NDVI values typically correlated to higher soil and surface temperatures as well as a higher CO_2 flux.

However, the control site in Ilam showed that the measured peak values of CO_2 flux, soil temperature and surface temperature did not align together at all; suggesting there was no present geothermal activity in that area. This was the expected result and was the reason why Ilam was selected as the control site to practice the sampling methods. In comparison, the target site in Harihari showed a strong alignment of peak measurements of sampled variables in two areas; closer to the cliff edge above the hot spring and by the swamp.

The area around the swamp showed that soil temperature at 20 and 50 cm and surface temperature increased around the swamp however, in contrast, CO_2 flux plummeted. This is actually to be expected as the highly saturated nature of swampy soil is known to inhibit CO_2 movement. The area around the cliff edge showed high values in CO_2 flux, high soil temperature and high surface temperature.

Impediments

Commencing the data collection process was arduous, however once the UAVs were up in air, there were no further hindrances. Data reconnaissance required the service of remote sensing; enlisting multiple UAVs, special infrared cameras and thermal optics that required technical expertise. This caused the sampling process to be 'technogically' intensive and in addition these essential high-tech gadgets did not always want to cooperate. There was a continual cycle of updating the ever-growing library of proprietary firmware that was not always compatible with the following iterations of hardware from different manufactures. Weather and batteries also hindered progress, but this was overcome with time and pre-emptive trouble shooting. Collecting field data was much more straight-forward. With one person to sample Ilam fields (CO_2, soil temperature) it would take a whole day (8hrs+), but

another set of hands greatly sped up the process (<~2.5hrs). It is estimated that the total time lost during the one-year period of research was two and a half to three months.

Statistically Assessing The Results

Probability testing Ilam and Harihari field data using the students T-Test and ANOVA produced the same P values found below. Note alpha or level of significance is 0.05. Null hypothesis (H_0) (or default position) refers the notion in statistical probability that if the probability value is greater than 0.05 (5%) the two populations are the same or not different enough to draw any conclusions. If it is lower than 0.05 it is accepted, meaning that the null hypothesis is rejected (ie the two populations are not the same) and there is an association between the two measured phenomena.

NDVI	T-Test	ANOVA	Alpha	Null H_0
P-Value	0.08019	0.080	0.05	Accept

CO_2 Flux	T-Test	ANOVA	Alpha	Null H_0
P-Value	0.01701	0.0170	0.05	Reject

ST20	T-Test	ANOVA	Alpha	Null H_0
P-Value	$2.05x10^{-19}$	$2.05x10^{-19}$	0.05	Reject

ST50	T-Test	ANOVA	Alpha	Null H_0
P-Value	$3.06x10^{-9}$	$3.06x10^{-9}$	0.05	Reject

ST	T-Test	ANOVA	Alpha	Null H_0
P-Value	0.76614	0.766	0.05	Accept

Of the five variables, based on P values calculated through the T-test and ANOVA, the radiometric data, NDVI and surface temperature of Ilam fields and Harihari not significantly different (0.080 and 0.766 respectively) and do not differ enough to draw any other conclusions. The effect that Ilam and Harihari have are not significant, thus the null hypothesis is accepted.

However, when looking at CO_2 flux, soil temperature 20 & 50cm, the P values from the T-test and ANOVA indicate that when comparing these three variables, the populations observed are statistically different (0.0170, $2.05x10^{-19}$, $3.06x10^{-9}$, respectively) the null hypothesis is rejected and is unlikely to be a result of random sampling.

Further Assessment Of The Results

Surface temperature indicated a relationship with NDVI in Harihari, but not in Ilam. The standard deviation of all field variables remained consistent throughout the four NDVI quartile ranges in Ilam and Harihari. However, the NDVI value in the first quartile range had a large spread because of the extremely low values (~-0.5 – 0.2); which is thought to be caused by sensory issues where the angle of sun reflectance of infrared radiation off a blade of grass (which shows very bright in a .TIFF image) appears as a null value, despite actually reflecting infrared radiation in reality. Other cases could involve non-vegetation objects like concrete or rock etc. In Harihari, as NDVI increased, 20 cm soil temperature and CO_2 flux spread increased and 50 cm soil temperature dropped slightly. This is more likely to be of a result of irregular NDVI values (mentioned above) than to the cooling of soil temperature at 50 cm.

The use of mean and 50% (Q2) values help to increase understanding of the data set; rather than just relying on mean values. The highest values in soil temperature did not always equate to the highest CO_2 flux, surface temperature and vice versa. Excluding NDVI, there was not a clear-cut pattern that each field variable followed in association with another variable. For example, in an area where CO_2 flux was at its highest so too was soil temperature at 50 cm but in another area where CO_2 flux was also high, soil temperature at 50 cm depth was relatively low. This can be found when each variable is cross examined with each other.

Essentially, these results show that NDVI while useful, is not enough in isolation to identify hidden geothermal systems; Ilam and Harihari displayed similar trends with rising NDVI. The location and ultimate comparison of the peak values in soil and surface temperature, CO_2 flux ought to be assessed to determine where, if any, geothermal activity is present.

Interpreting Surface Anomalies

The field site in Harihari that borders the Wanganui river that is made up of predominantly long grass. Over time there appears to be a muddy bog that has developed. This bog is recognised as a surface anomaly and could be a result of meteoric origin or geothermal or a mixture of the two. There are several interpretations into the possible genesis of the swamp.

First, it is a puddle: The lowest point in the field is located in the swamp. It is possible that meteoric water could have accumulated in the field and developed a large puddle.

Second, it is a low temperature ground water spring: Could be a result of the underground movement of low temperature ground water into the swampy area.

Third, it is a thermal spring/ swamp: To start with why it is likely that the swamp is likely to be of hydrothermal origin, I will outline why the swamp is unlikely to be a result of meteoric water accumulation. For meteoric water accumulation to be present on the surface, the puddle must be sealed on top of a layer of impermeable strata. In the field, this is not the case, the sediment is very poorly sorted and coarse gained, this leads to the pore spaces being of a high percentage that allows water to percolate down into the ground water table.

It is unlikely that the swamp is caused by a low temperature ground water spring because just like a puddle of meteoric origin, the temperature of the fluid found in the swamp is relatively high compared what would be found from typical meteoric water and ground water temperatures.

Elevated fluid thermal temperatures are consistent with a surface hydrothermal features like hot springs found in the area, however those temperatures were much higher and ranged from 20-50 °C and the temperature in the swamp is found to be approximately ~13 °C.

The CO_2 flux found in the swamp is relatively low because the porous sediment is blocked with slightly warm water that restricts CO_2 gas movement from the soil to the atmosphere (Klusman R.W., et al., 2000).

Hypothesis, Deductions and Interpretations

Ilam fields was used as the field to test and develop the methods that were subsequently taken to Harihari to assess the accuracy of detecting blind geothermal systems on a similar scale. The field data surveyed suggests that, unless measurements are taken in close proximity to them, hidden geothermal hotspots are difficult to detect. Based on the research presented here, the two geothermal related areas in the field (the swamp and cliff edge) presented notable overlap between soil temperature and CO_2 flux (figure 6.0).

Figure 6.0 (Right): Map showing where the peak values in field variables are located in the field, these areas signify the location of geothermal activity present in the field.

Map is supported with an overview of the thermal fluids at the base of the cliff.

Elevated values of the following:

- CO_2 Flux
- Soil Temperature 20 cm
- Soil Temperature 50 cm
- Surface Temperature

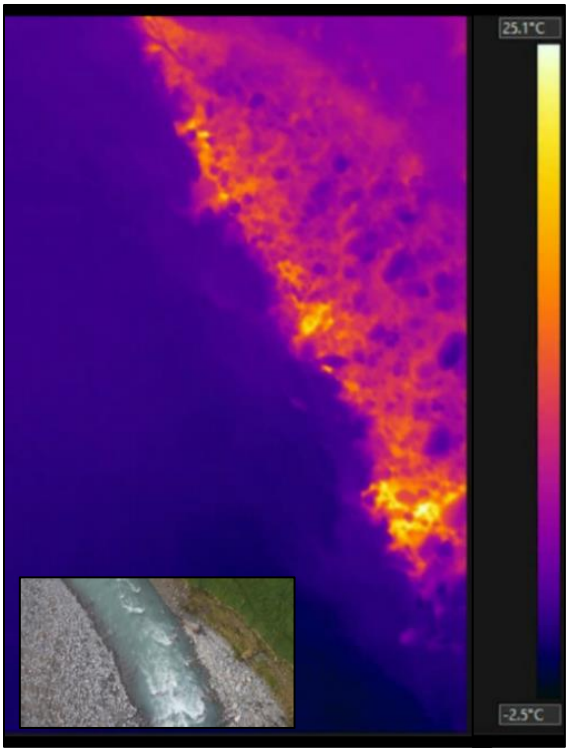

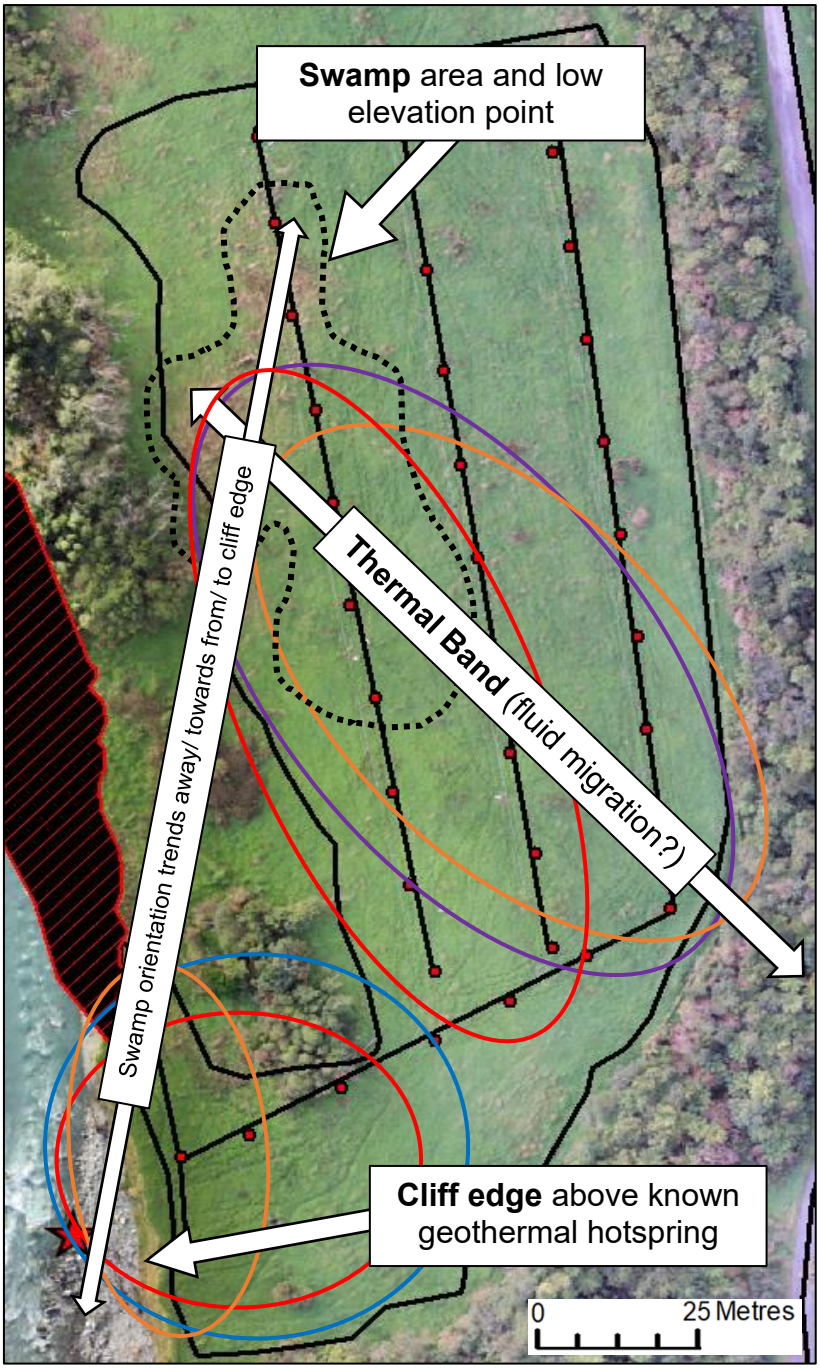

Swamp

The swamp area, which is ostensibly a surface manifestation of underlying geothermal activity, is split into two main parts. The top half, where the hydrothermal fluids reach the surface, is marked where the muddy soil is most prevalent. This can be identified by the significant vegetation growth in this area (figure 6.01). The second part of the swamp further south, appears to be less muddy on the surface and continues down the transect further away from the more vegetated area. While lacking vegetation on the surface and being slightly less waterlogged, the muddy area (further south), just like the vegetated area, displayed the residual effects of geothermal interaction in the surrounding soil (with spikes in soil and surface temperatures), suggesting that this swamp system propagates further outwards underground. The swamp extends further down the field away or towards to/ from the known hot spring near cliff edge (figure 6.0), which could suggest that the swamp and the hot spring near cliff edge are related.

The swampy area was the only zone in the field that exhibited significant water saturation in the soil. The swamp area existed both on the surface and underground and was the perfect target, upon which to test these methods.

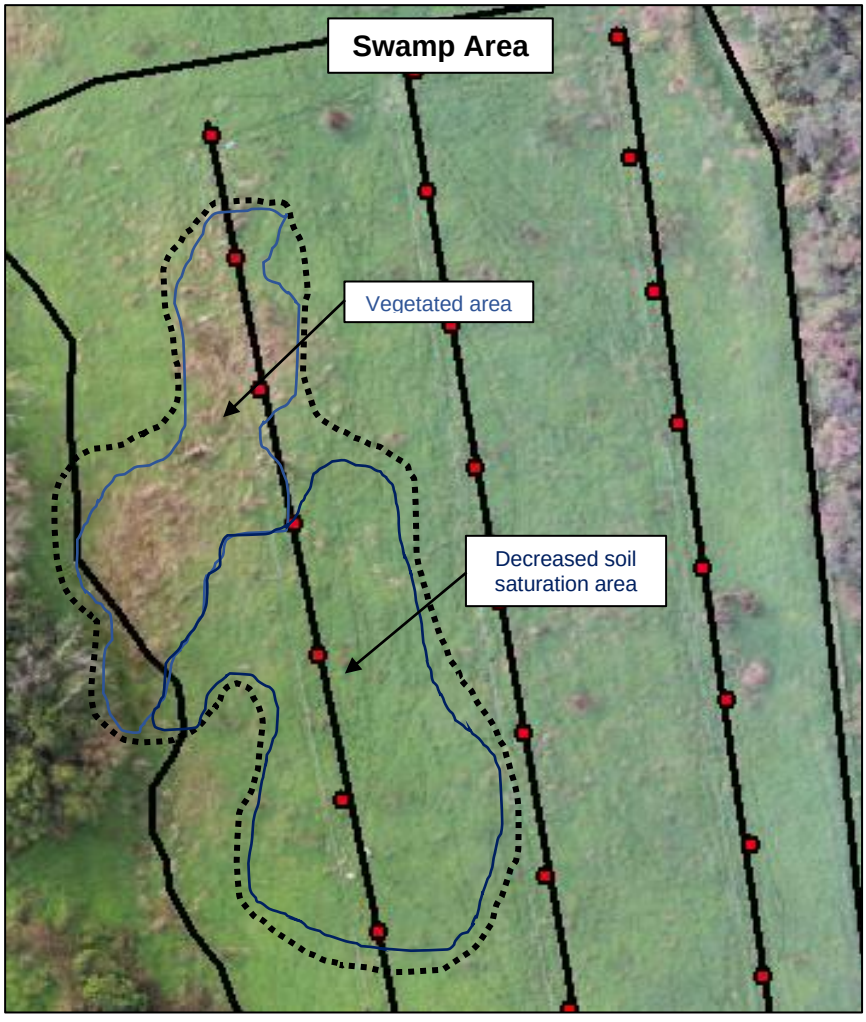

Figure 6.01: (Left) Breakdown map of the swamp.

Thermal Band

The swamp area marked in Figure 6.01 was one of the lower areas located in the field. The thermal band marked an area with minor undulating terrain on the surface. This soil above the thermal band did not appear to be muddy in nature like the swamp as evidenced with the increased CO_2 flux. The thermal band consisted of medium-high 50 cm soil temperature profiles, slightly above average CO_2 flux and high surface temperatures which cut though the field and exited into the swamp (figure 6.01 and figure 6.02). The approximate average CO_2 flux, 50cm soil temperature and surface temperature through this band was, ~1.15 ppm/s, ~13.5 °C and ~5.5 °C respectively. It was noted that on either side of the thermal band there were two spots that had cooler surface temperatures which suggests, the thermal band is cutting through the existing cooler soil. The exact formation of the swamp leads to, two possible explanations (figure 6.02).

Both explanations rely upon the hypothesis that the thermal band is cutting through an existing strip of colder land, where the migrating hydrothermal fluids trend north-east. The first theory is that the migrating fluids exit into the low point building a muddy swamp, that is rich in nutrients in CO_2 and warmer fluids which promote vegetation growth. The second theory is that the hydrothermal fluids, which originate beneath the bog, are protruding to the surface, filling the muddy bog from below and then migrating outwards, away in the form of the thermal band. The first theory is thought to be more likely, however, it could also be a combination of the two.

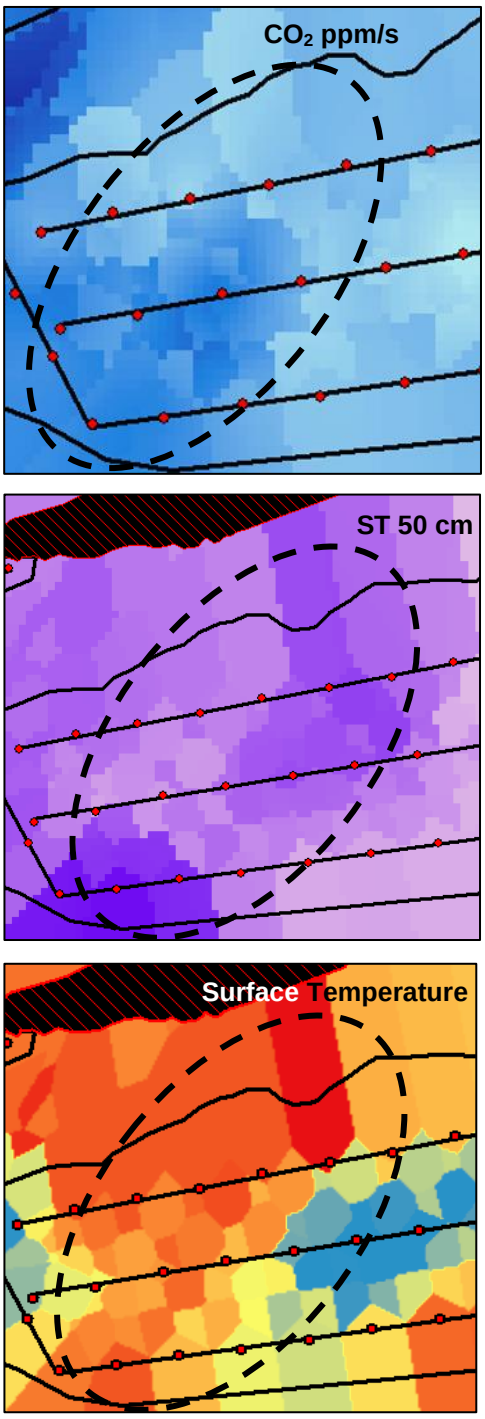

Figure 6.02: (Above) displays elevated values in CO_2 flux, 50 cm soil temperature profiles and surface temperature.

Cliff Edge

The cliff edge is located above active hydrothermal fluids that protrude at the base of the cliff face (figure 6.0). The hot spring is highlighted in the thermal optics image below (figure 6.03). The increases in thermal flux are identified by a brighter yellow/white colour. This is further reinforced when looking at an extended view of the cliff edge comparing the hydrothermally enriched sediment (~25 °C) with the colder (~8 °C) river sediments. This is consistent with field recordings of the sediment deposit where the sand on the banks had a thermal temperature of 20-26 °C and the surrounding river deposits were ~8 °C.

Approaching the cliff edge, the vegetation's NDVI values, CO_2 flux, 20cm soil temperature and surface temperature increased to ~0.75, 1.5-2 ppm/s, ~13 °C and ~6 °C respectively. The thermal imaging was great for detecting thermal fluid outflows that can be seen from above. An extended view of the cliff base shows the contrast between sediment that has integrated with hydrothermal fluids and the colder river bank sediment (figure 6.03).

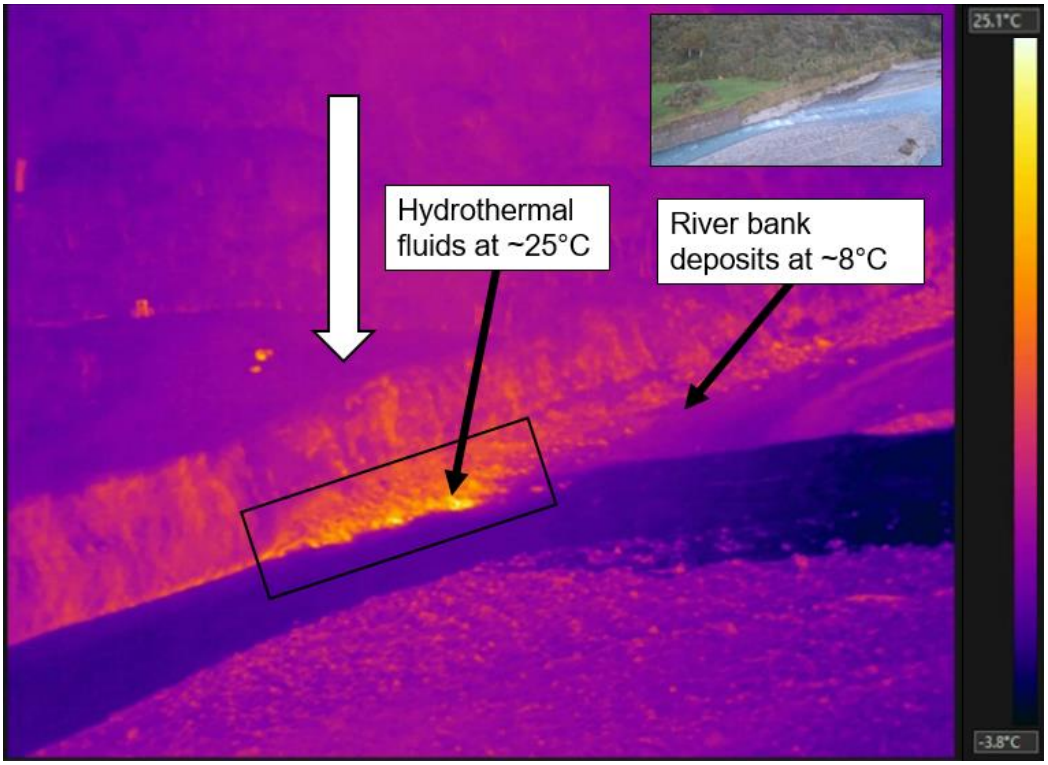

Figure 6.03: Thermal image of an extended view of the thermal fluids that contrast to the surrounding river deposits.

Ilam Fields

The control site in Ilam has no geothermal activity and so the peak values in soil and surface temperature and CO_2 flux are separated away from each other (figure 6.04). At this time NDVI cannot be solely used to identify potential geothermal areas in low enthalpy systems. The control site in Ilam and the target site in Harihari both showed an increase with soil and surface temperature and CO_2 flux with rising NDVI (figure 5.41 and 5.47), suggesting that while NDVI can be used estimate soil conditions, it does not signify geothermal activity here.

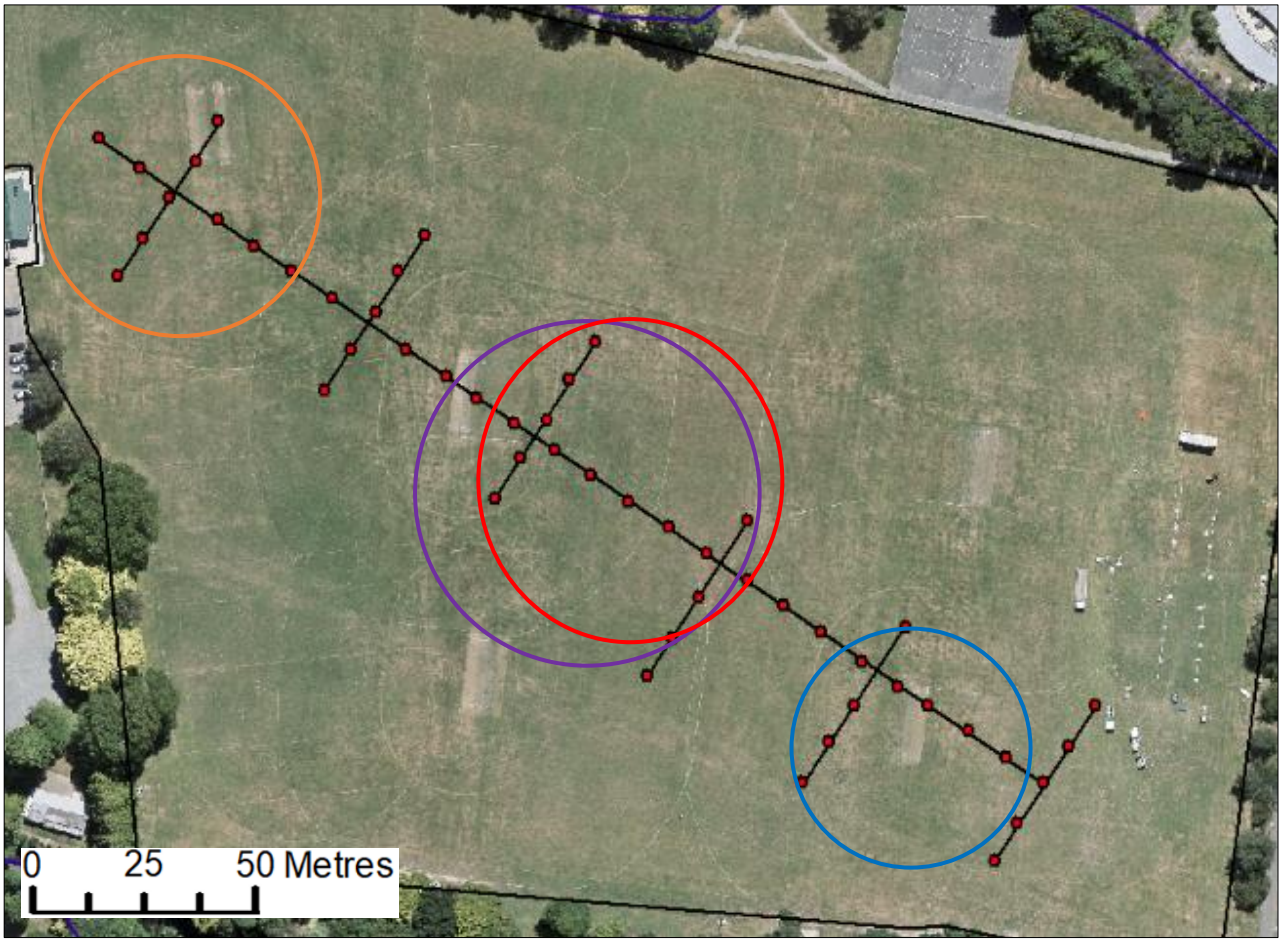

Figure 6.04: Ilam map displaying the location of where the field variables peak.

Previous Research

The field site in Harihari used in this thesis was originally used as the field site as part of M. Hansen, et al., research in 2015 titled 'Soil CO_2 flux and isotopic surveys to identify and characterize low enthalpy springs associated with the Alpine Fault, New Zealand' (figure 6.05).

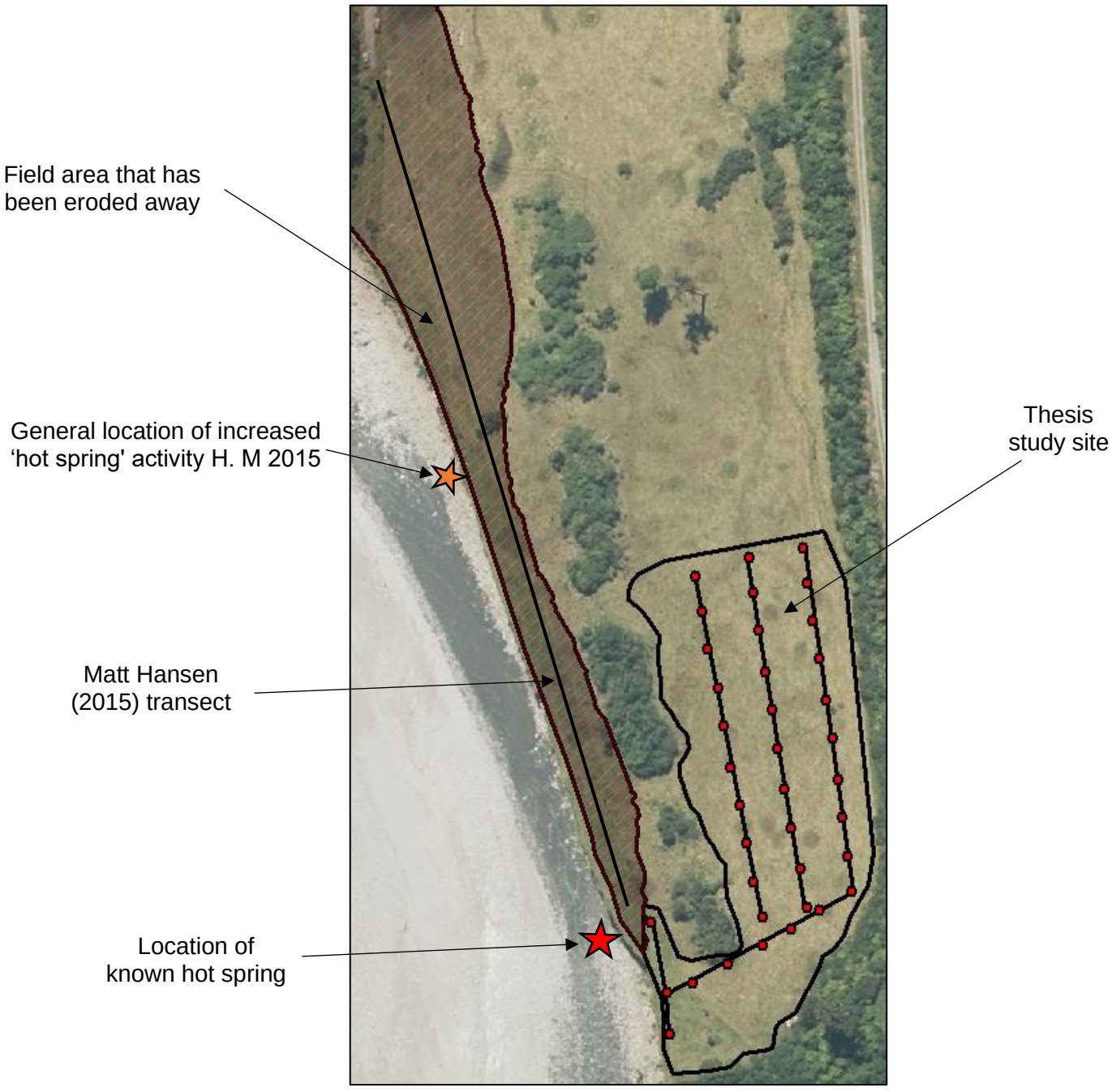

Figure 6.05: Map displaying the location MC Hanson's study site.

However, all of the valuable land used in that study eroded away during the flooding event in March 2019. That research focused on identifying carbon sources in low enthalpy systems using carbon isotopes and soil temperature. The sampling was conducted on a transect that ran parallel to the hot spring.

Hansen's studies showed there were minimal changes in the soil temperature along the transect; ranging from 13.3 to 18.3 °C, with none greater than 20 °C. The research discovered a "general increase in 10 cm temperature as the transect approaches the spring" (Hansen, M., et al., 2015). The same study also concluded that the highest soil temperature values did not always correlate to the highest CO_2 flux value, which is similar to the research found for this thesis.

In another location on the transect further north (200-210 m away from the known spring) it was found that the 10 cm temperature profiles, CO_2 flux, and d13 CO_2 all increased, suggesting that this area also contained another warm spring that is hidden by the transported river gravels (Hansen, M., et al., 2015).

CO_2 fluxes generated from geothermal activity are generally undetectable on the surface except when observed directly above those geothermal systems. CO_2 flux and 10 cm soil temperature surveys are capable of identifying thermal activity despite the lack of visible surface expression (Hansen, M., et al., 2015). The hot spring that was sampled by Hansen, has now been buried by the dynamic river system that is the Wanganui River.

Current Research

Time constraints limited our methods to data collection to NDVI, Thermal, Soil gas CO_2 flux and soil temperature, but there are more methods that are used in other research focusing on remote sensing application in geothermal areas. Some are listed below;

Hydrothermal Alteration Mapping	Controlled Source Electromagnetic Survey
Stress Field Estimates	Electrical Resistivity
Gravimetric/ Seismic Surveys	Core Drilling
Magnetotelluric	Hydraulic, pore and permeability testing
Geochemical Surveys	Structural Geology

Table 6.01: Location of Matthew Hanson's study site back in 2015.

Study Site Features and Nuances

The two maps (figure 6.06 and 6.07) below show the details picked up in the false colour raw infrared NDVI image.

Ilam Fields

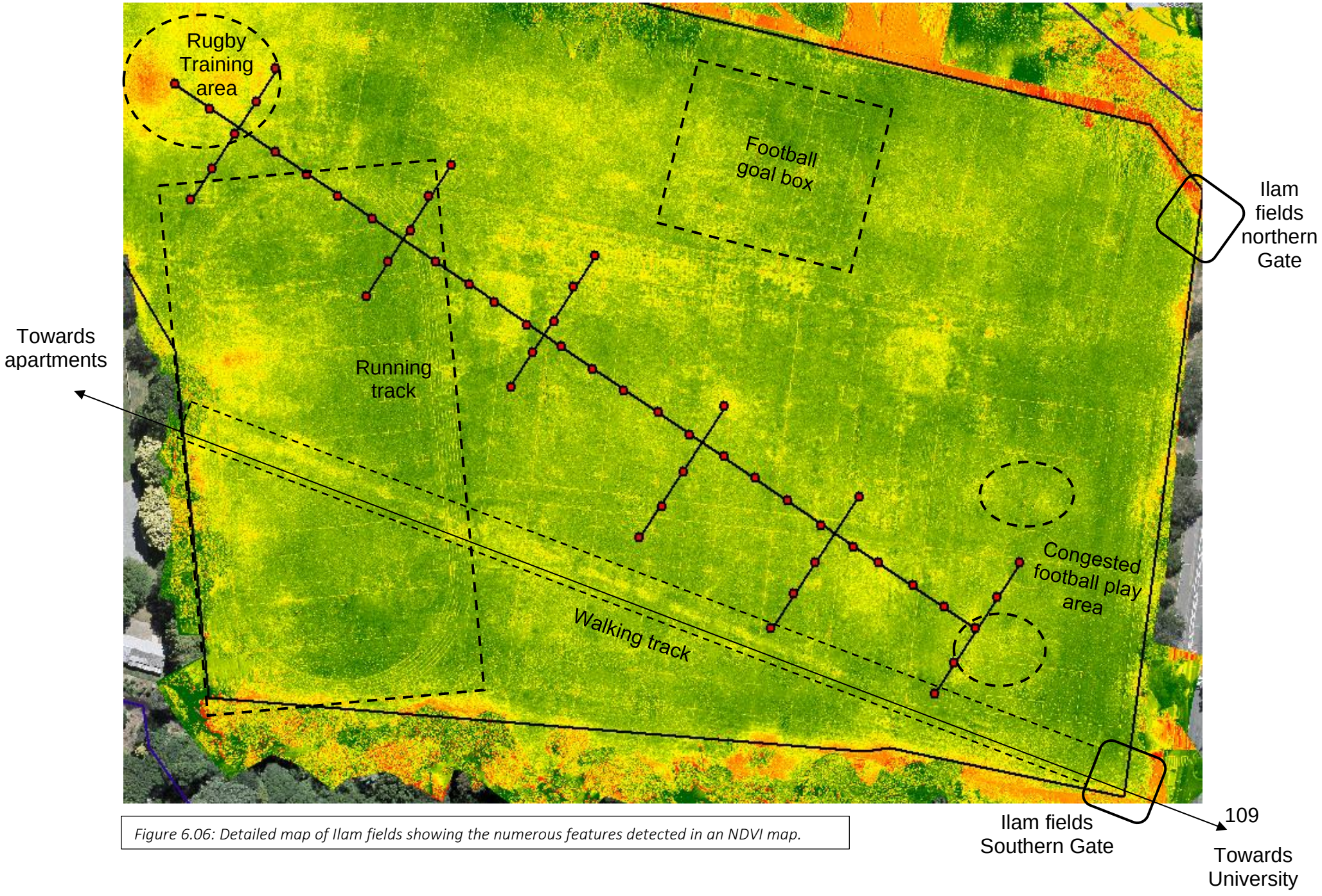

Figure 6.06: Detailed map of Ilam fields showing the numerous features detected in an NDVI map.

Harihari

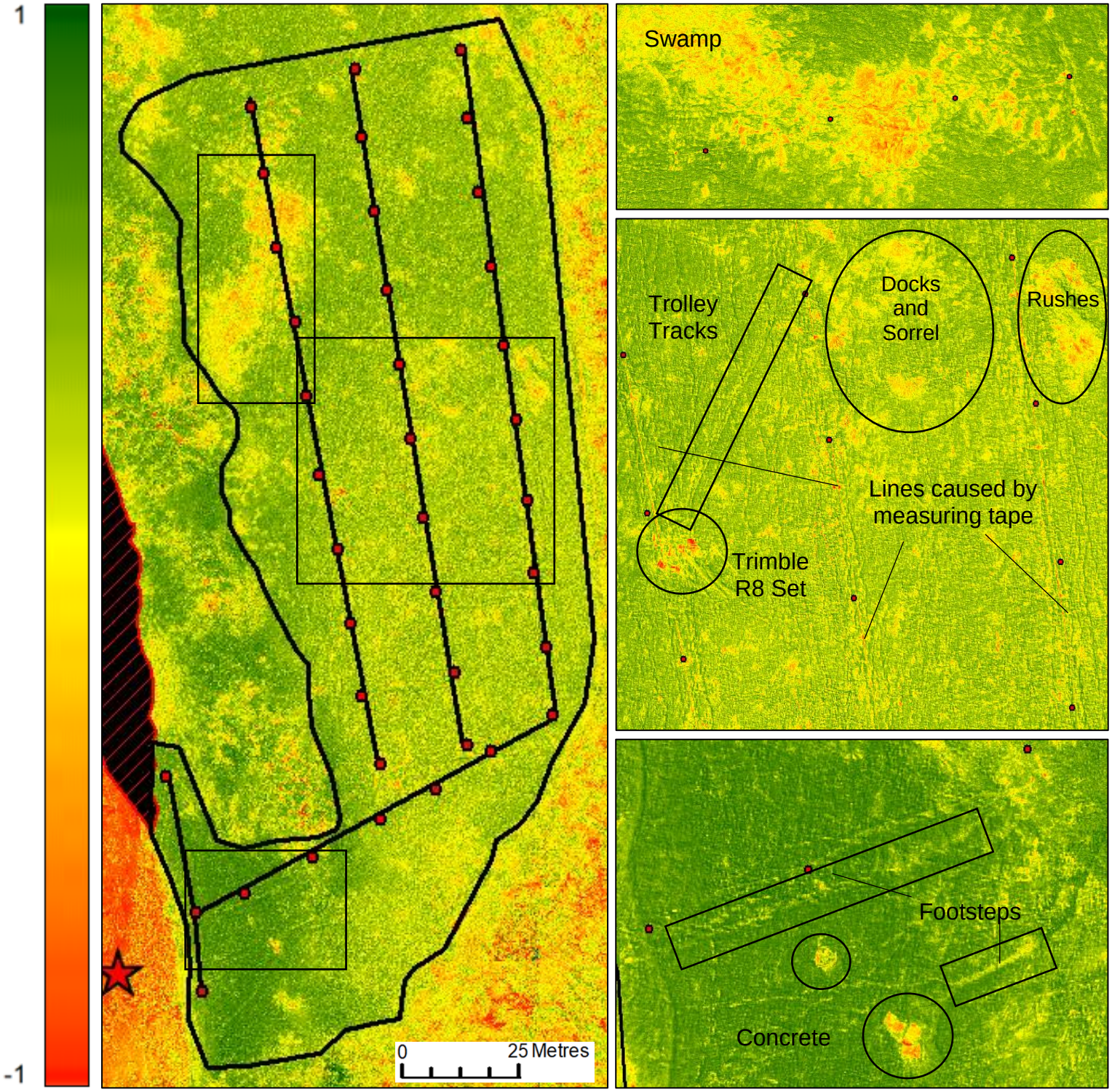

Figure 6.07: Detailed map of Harihari field site showing the numerous features detected in an NDVI map.

The Next Step

Had a significant amount of time not been lost to equipment malfunctions, I would have liked to have categorised all surface types (grass, bush, alternate plants types, water, soil, rock, sand, and etc.) in both Ilam and Harihari and measure the thermal emissivity index and adjusted NDVI of these for a more accurate analysis in surface thermography and NDVI. This would have enabled me to more accurately assess the viability of NDVI being used to detect geothermal systems; though I feel the same result would have been concluded with.

The location with the highest NDVI value in Harihari and Ilam did not directly correlate with the highest surface and soil temperature or highest CO_2 flux. Low NDVI values were recorded when surveying the swamp. These results were unexpected, but understandably explained by the overgrowth of bushes and presence of mud in the area. Although the swamp is a surface product of geothermal activity, not all instances of bush growth can be classified as a direct result of geothermal activity; must assess soil conditions to conclude as such. The extensive growth bushes in the swamp negatively altered the NDVI values recorded, thus relying on spectral imaging alone in this type of situation is not dependable.

The geothermal system present in Harihari is estimated to have originated from kilometres below the surface, but the exact distance of which the hydrothermal fluids interact with the soil above is unknown. But due to the results concluded, it must be rather close perhaps ~10 metres below where the thermal band is located and slowly climbs until it reaches the surface in the swamp, but this is just an estimate. There are hydrothermal fluids present on the surface in the swamp and also at the base of the cliff. Currently, analysis into the depths of the hydrothermal fluids under the terrace has yet to be conducted.

Despite the rather minor effluxes at the surface, remote sensing combined with field surveying of CO_2 flux and soil temperature demonstrated the ability to potentially detect blind low enthalpy geothermal systems. However, in these low flux environments alternative factors such as permeability and perturbation to the pedosphere–biosphere, complicate result analysis (Hansen, M., et al., 2015). These results suggest that high resolution transect XY grid surveys deliver a promising method of geothermal exploration at this scale, within environments that don't produce high CO_2 flux on the surface. Currently, the limitations for high resolution transect surveys are expertise, cost, and time required for vast field sampling.

Further advancements in technology and methodology would enable future exploration projects of a similar type to be conducted with increased efficiency and at a lower cost. Existing methods of large aircraft aerial flights and core drilling are incredibly expensive in resource prospect evaluation and can be hit or miss.

Technological advancements could consist of field data being able to be remotely sensed at incredibly higher resolutions that would additionally include measurements CO_2 flux, and soil and surface temperatures. Greater satellite resolutions would most likely also reduce surveying costs. Currently, a sole reliance on spectral data is most likely to produce highly variable results. This is evidenced by the NDVI measurements taken which displayed similar trends at both test sites, even though the Harihari site showed actual evidence of underlying geothermal activity.

Only one site involved with geothermal activity was sampled, so being able to add more sites and to continue a larger study by revisiting them across multiple seasons to record any changes in vegetation behaviour over the year in geothermal environments, as well as being able to assess the changes in water table and to run night missions with thermal imaging for an even greater thermal contrast is hypothesised to further develop and potentially add significantly to the conclusions found in this research. Such advances would become an important asset for geothermal resource exploration. While the results are not 100% conclusive, there is enough here to go on as the results look promising. The model developed here can be re-used in its entirety and/ or tweaked to one's preference for future missions.

VII. CONCLUSION

Ilam fields provided a great opportunity to develop testing methods that would later be used in Harihari. Learning the procedure of how to use the equipment was instrumental into successfully collecting field data in Harihari without running into issues that was ever so present in Ilam fields. During the first test runs in Ilam many issues were encountered both in the field and then again in post processing. I needed to develop the skills required in the field with the equipment (UAV, flux meter etc) and with the software (python, Arcmap, Agisoft Photoscan, Adobe Premier, FLIR tools etc).

Conclusions Suggested By This Thesis

There are 10 main conclusions supported by the results presented in this thesis:

1) The area overlying the known geothermal hotspring (cliff edge) (Fig. 5.31; Fig. 6.0; Fig. 6.3) shows an elevated 20cm soil temperature (13.2°C versus field mean of 12.2°C; Table 5.07; Fig. 5.25).

2) The area overlying the known geothermal hotspring (cliff edge) (Fig. 5.31; Fig. 6.0; Fig. 6.3) shows an elevated CO_2 flux (1.86 ppm/s versus the mean 0.808 ppm/s; Table 5.06; Fig. 5.23).

3) The area overlying the known geothermal hotspring (cliff edge) (Fig. 5.31; Fig. 6.0; Fig. 6.3) shows an elevated surface temperature (6.2°C versus the mean 5.7°C; Table 5.09; Fig. 5.29).

4) The area overlying the anomalously warm and wet area in the Harihari survey site (Fig. 5.18; Fig. 6.0; Fig. 6.01; Fig. 6.3) shows an elevated 20cm soil temperature (~12.4°C versus the mean 12.2°C; Table 5.07; Fig. 5.25).

5) The area overlying the anomalously warm and wet area in the Harihari survey site (Fig. 5.18; Fig. 6.0; Fig. 6.01; Fig. 6.3) shows an elevated 50cm soil temperature (~13.5°C versus the mean 13.2°C; Table 5.08; Fig. 5.27).

6) The area overlying the anomalously warm and wet area in the Harihari survey site (Fig. 5.18; Fig. 6.0; Fig. 6.01; Fig. 6.3) shows relatively low CO_2 flux (~0.435 ppm/s versus the mean 0.808 ppm/s; Table 5.06; Fig. 5.23). Consistent with the filling of permeable pore space with elevated temperature fluid.

7) The area overlying the anomalously warm and wet area in the Harihari survey site (Fig. 5.18; Fig. 6.0; Fig. 6.01; Fig. 6.3) shows an elevated surface temperature (~6.0°C versus the mean 5.7°C; Table 5.09; Fig. 5.29).

8) The suggested thermal area that cuts through the field in Harihari (Fig. 6.0; Fig. 6.02) shows an elevated 20cm soil temperature (~12.7°C versus the mean 12.2°C; Table 5.07; Fig. 5.25).

9) The suggested thermal area that cuts through the field in Harihari (Fig. 6.0; Fig. 6.02) shows an elevated 50cm soil temperature (~14.1°C versus the mean 13.2°C; Table 5.08; Fig. 5.27).

10) The suggested thermal area that cuts through the field in Harihari (Fig. 6.0; Fig. 6.02) shows an elevated surface temperature (6.2°C versus the mean 5.7°C; Table 5.09; Fig. 5.29).

Surface temperature suggests that the conclusions indicate surface anomalies of geothermal origin (cliff edge, swamp and thermal band) but radiometric data and the respective high p value (0.766) suggests that this surface temperature data is likely to be random.

Assessing The Probability Values

The P values calculated through the T-test and ANOVA (table 5.18; table 5.22) (0.080 and 0.766 respectively) suggest that radiometric data (NDVI and Surface Temperature) alone do not completely indicate geothermal features. Ilam and Harihari do not differ enough to draw any conclusions. Unlike the radiometric data, the CO_2 flux, soil temperature 20 & 50cm P values from the T-test and ANOVA (table 5.19; table 5.2; table 5.21) (0.0170, 2.05×10^{-19}, 3.06×10^{-9} respectively), do suggest that these three field variables are statistically significant when comparing Ilam field data to Harihari field data.

There are a number of reasons why the two study sites presented here might be similar, or significantly different. Statistical tests alone cannot prove the existence of a surface blind geothermal system. This is why geoscientists rely on geological reasoning, just as much if not more, than they rely on statistics. There are many reasons why a direct scientifically-robust comparison is not recommended given the time frame (for this thesis). The sites sampled could be significantly different or not for a number of reasons, I will just name a few.

1) Climate / weather
2) Biome
3) Soil type & composition
4) Bed rock weathering
5) Soil moisture %
6) Soil pH
7) Field set up (ungrazed compared to fertilized, poisoning, mowed etc)
8) Soil compaction

Importantly, Ilam and Harihari are significantly different but not necessarily significantly different due to the presence/absence of a surface-blind geothermal resource. Probability testing can help in isolating or detecting if the sample set is a result of chance: but the ONLY way to INFER the presence/absence of a geothermal resource at depth is to apply geological reasoning to a diverse suite of data-based indicators/variable (e.g. soil temp.; CO_2 flux; etc.).

The purpose of adding Ilam fields to the study was to learn the skills/tools locally prior to going to Harihari. The inclusion Ilam field data was also meant to deliver a broad perspective of what field data could look like in geothermal and non-geothermal environments, a statistical comparative analysis was never the intention.

Justification Of Transect Design

The use of transect was used assess fluctuations in surface variables (CO_2 flux, soil temperature) through equally spaced intervals. This allowed us to understand the profiles of the variables measured and develop an understanding of how the measured variables fluctuate throughout the field.

Final Remarks

Circling back to the question posed by this thesis 'what is potential application of remote sensing and field surveying in identifying blind low enthalpy geothermal systems', the results suggest it is possible (see: 10 conclusions suggested by this thesis).

However, geological sub-surface inference based on surface observations cannot perfectly predict whether or not a potential geothermal resource is present at depth. The research presented here suggests that multi-proxy approaches, including NDVI, soil temperature, infrared imaging and soil CO_2 flux are useful for detecting areas of elevated heat flow within the Amethyst hot springs system. Including stable isotopic tracers (Hanson, et al., 2015) would further strengthen inferential geothermal resource targeting in metamorphic/structurally-controlled systems like those adjacent to the Alpine Fault.

NDVI can be used as litmus for vegetation health, but preferably in areas that have only one type of vegetation to keep variables to a minimum. NDVI alone is not enough in low enthalpy systems because the control and target site showed similar overall trends.

If technology can advance enough to attain a high enough resolution for infrared and thermal for surface mapping on the centimeter scale. If a future method of quickly measuring CO_2 concentration and CO_2 flux and soil temperature remotely would provide unprecedented benefits to geothermal exploration.

VIII. EPILOGUE

I want to start off by thanking my supervisors Travis Horton and Peyman Zawar-Reza for assisting me over the year, giving me valuable feedback and their help in shaping my thesis with their guidance. Thanks to Alex Nichols for his support too.

I would also like to acknowledge Stan Mordensky for acting as a mentor to me during the early stages of my thesis giving me advice and being supportive.

Obviously thanks to all staff and technicians. Nick K. and Paul B. for the UAV work, Michelle L. with the Planet.com access, Matt C. with the CO_2 Li-COR, Sacha B. with DCP and Cathy H. with her help in using the Trimble R8 GNSS system.

Also want to thank Sammy Griffin with her help at the beginning of my thesis, I wish her well with her pHD in the UK.

And want to thank Jordan M. Lafaele for assistance during the editing process.

IX. REFERENCES

Aerial Crystal Mark, (2019). Absorption graph comparing healthy and unhealthy vegetation retrieved from Agricultural Surveys URL: 'Aerial.crystalmark.co.uk', March 14, 2019.

Agba, E.H., Laogun, A.A., Nathaniel. A., (2009). A comparison of the effect of diagnostic X-rays on the radio frequency dielectric properties of bovine liver wint bovine kidney tissues. Nigerian Journal of Physics. 20. 10.4314/njphy.v20i1.38149.

Allis, R.G., Shi, Y., (1995). New insights to temperature and pressure beneath the central Southern Alps, New Zealand, New Zealand Journal of Geology and Geophysics, 38:4, 585-592.

Angelov, P., Baber, C., Delgado, L., Ford, J.J., Lai, J., et al., (2012). Sense and Avoid in UAS Research and Applications.

Berryman, K.R., Beanland, S., Cooper, A.F., Cutten, H.N., Norris, R.J., Wood, P.R., (1992). The Alpine Fault, New Zealand: Variation in Quaternary Structural Style and Geomorphic Expression, Annales Tectonicae, Supplement, v6, p126-195.

Casagrande, G., Sik, A., Szabo, G., (2018). Small Flying Drones, Applications for Geographic Observation.

Chen, D., Huazhong, R., Qiming, Q., Jinjie, M., Shaohua, Z., (2015). A Practical Split-Window Algorithm for Estimating Land Surface Temperature from Landsat 8 Data.

Chuai, X.W., Huang, X.J., Wang, W.J., Bao,G., (2013). NDVI, Temperature and Precipitation Changes and Their relationships With Different Vegetation Types During 1998–2007 In Inner Mongolia, China.

Cui, L.L., Shi, J., (2010). Temporal and spatial response of vegetation NDVI to temperature and precipitation in eastern China. Journal of Geographical Sciences.

Cox, S.C., Menzies, C.D., Sutherland, R., Denys, P.H., Chamberlain, C., Teagle, D.A.H., (2015). Changes in hot spring temperature and hydrogeology

of the Alpine Fault hanging wall, New Zealand, induced by distal South Island earthquakes: Geofluids, v.15, no.1-2, p.216–239, doi: 10.1111/gfl.12093.

Dahl, R., (2018). General Manager of OptoDiode Corporation, Photonics Handbook.

Droneteck.ca, (2019). Image retrieved, November 14th 2018.

E-education.psu.edu, (2019). Image retrieved, November 9th 2018.

Fertoing.com, (2019). Image retrieved November 2nd 2018.

Fischer, T.P., Santiago, A., Simon, C., Alessandro, A., Bo, G., Patrick, A., Taryn, L., Hiroshi, S., Peter, K., Cynthia, W., Carlo, C., Chiodini, G., (2019) The emissions of CO2 and other volatiles from the world's subaerial volcanoes. Scientific Reports. 9. 10.1038/s41598-019-54682-1.

Giggenbach, W. F., Sano, Y., Wakita, H., (1993). Isotopic composition of helium, and CO_2 and CH_4, contents in gases produced along the New Zealand part of a convergent plate boundary.

Grant, B.G., (2011). Field Guide to Radiometry.

Harvey, M.C., Rowland, J.V., Luketina, K.M., (2016). Drone with thermal infrared camera provides high resolution georeferenced imagery of the Waikite geothermal area, New Zealand

Hanson, M.C., Oze, C., Horton T.W., (2015). Cavity Ring Down Spectroscopy for the Rapid Estimation of δ13C of Soil CO2 Flux in H2S-rich Geothermal Areas.

Honsberg, C.B., Bowden, S.G., (2019). Absorption Coefficient, https://www. pveducation.org /pvcdrom/pn-junctions/absorption-coefficient.

Humboldt University, (2019). Image retrieved from URL: 'http://gsp.humboldt .edu/OLM/ Courses/GSP 216 Online/lesson4-1/radiometric.html' July 4th, 2019.

International Civil Aviation Organization (ICAO). (2011). Unmanned Aircraft Systems (UAS).

Infinity-theory.com, (2019). Image retrieved November, 14th 2018.

integraldrones.com.au, (2019). Image retrieved November, 16th 2018.

Karnieli, A., Gabai, A., Ichoku, C., Zaady, E., Shachak, M., (2002). "Temporal Dynamics Of Soil And Vegetation Spectral Responses In A Semi-arid Environment." International Journal Of Remote Sensing.
Kevin A.R, Michael S.R., (2013). Exploration of geothermal systems using hyperspectral thermal infrared remote sensing

Klusman, R., Moore, J., LeRoy, M., (2000). Potential for surface gas flux measurements in exploration and surface evaluation of geothermal resources. Geothermics. 29. 637-670. 10.1016/S0375-6505(00)00036-5.

Kohler, M., Eberhart-Phillips, D. (2003). Intermediate-depth Earthquakes in a Region of Continental Convergence: South Island, New Zealand, Bull Seis. Soc Amer, 93, 85-93.

Koons, P.O., Craw, D., (1991). Evolution of fluid driving forces and composition.

Koons, P.O., Craw, D., Cox, S.C., Upton, P., Templeton, A.S., Chamberlain, C.P., (1998). Fluid flow during active oblique convergence: A Southern Alps model from mechanical and geochemical observations within collisional orogens: Geophysical Research Letters.

Koons, P.O. (1987). Some Thermal and Mechanical Consequences of Rapid Uplift, an Example from the Southern Alps, New Zealand, Earth Planet. Sci. Lett., 86, 307-319.

Koons, P.O., (1989). The topographic evolution of collisional mountain belts; a numerical look at the Southern Alps, New Zealand: American Journal of Science, 289, p.1041–1069.

Menzies, C.D., Wright, S.L., Craw, D., Rachael H.J, Jeffrey C.A, Cox, S.C., Iain K.P, Damon A.H.T., (2017). Carbon dioxide generation and drawdown during active orogenesis of siliciclastic rocks in the Southern Alps, New Zealand

National Aeronautics and Space Administration (NASA). Science Mission Directorate. (2010). Visible Light. (https://science.nasa.gov /ems/09_ visiblelight).

Nemani, R., Keeling, C., Hashimoto, H., Jolly, W., Piper, S., Tucker, C., Myneni, R., Running, S., (2003). Climate-driven increases in global terrestrial net primary production from 1982 to 1999. Science. 300. 1560.

The New Zealand National Climate Database (NIWA), (2019).

Omnes, F., & Monroy, E., (2010). Ultraviolet Photodetectors. 10.1002/ 9780470 611630.ch6.

Overton, G., (2014). Photonics Applied: Terrestrial Imaging: Spectral Imaging Satellites Monitor Global Vegetation Health via NASA.

Papa, U., (2018). Introduction to Unmanned Aircraft Systems (UAS). 10.1007/978-3-319-73174-2_1.

Pessarakli, M., (2016). Handbook of Photosynthesis 3rd edition.

Planet Application Program Interface (2019). In Space for Life on Earth. San Francisco, CA.

Resource Supply LLC, (2019). Image retrieved from URL: 'https://www. resourcesupplyllc.com/product-tag/atlas-rtk-gnss/', June 12, 2019.

Rey, G., Spindler, C., Babbe, F., Rachad, W., Siebentritt, S., (2017). Laboratory for Photovoltaics, Physics and Materials Science Research Unit, L-4422 Belvaux, Luxembourg M. Nuys and R. Carius Forschungszentrum Jülich GmbH Institut für Energie und Klimaforschung, 52425.

Reyes, A.G., Britten, K., (2007). Variations in Chemical and Isotopic Compositions of Mineral Spring Systems in South Island, New Zealand: no.2001, p.1–6.

Reyes A.G., (2010). Assessing the Flow of Thermal Waters in Low-Temperature Academic Press, 3rd Ed.

Roerink, G.J., Menenti, M., Su, Z., Soepboer, W., (2003). Assessment of climate impact on vegetation dynamics by using remote sensing. Geophys. Res. Abstr. 4 (2002): 1 p. (cd). 28.

Rouse, W., Well, R.H., Deering, D. W., (1974) Monitoring vegetation systems in the great plains with ERTS.

Schimel, D.S., House, J.I., Hibbard, K.A., Bousquet, P., Ciais, P., Peylin, P., Braswell, B.H., Apps, M.J., Baker, D., Bondeau, A., Canadell, J., Churkina, G., Cramer, W., Denning, A.S., Field, C.B., Friedlingstein, P., Goodale, C., Heimann, M., Houghton, R.A., Melillo, J.M., Moore, B., Murdiyarso, D., Noble, I., Pacala, S.W., Prentice, I.C., Raupach, M.R., Rayner, P.J., Scholes, R.J., Steffen, W.L., Wirth, C., (2001). Recent patterns and mechanism of carbon exchange by terrestrial ecosystems. Nature 414.

Schowengerdt, R.A., (2007). Remote Sensing: Models And Methods For Image Processing.

Sheng, S.L., (2006). Semiconductor Physical Electronics.

Shi, Y., Allis, R., Davey, F., (1995). Thermal Modelling of the Southern Alps, New Zealand.

Stanley, C., Enrico, P.M., Margaret, A.B., (1974). Third Earth Resources Technology Satellite-1 Symposium-Volume I: Technical Presentations Section A: The proceedings of a symposium held by Goddard Space Flight Center at Washington, D.C. on December 10-14,1973.

Strathclyde University, (2019). Image retrieved from URL: ‘Strath.ac.uk/ Electrical engineering’, Feb 26, 2019.

Siu, Wai-Lok & Fung, Tung. (2000). Environmental quality and its changes, an analysis using NDVI. International Journal of Remote Sensing - INT J REMOTE SENS. 21. 1011-1024. 10.1080/014311600210407.

Stephens, R., (2018). retrieved from URL: ‘https://diydrones.com/photo/drone-typology’, April 10, 2019.

Vollmer, M., Möllmann, K.P., (2018). ‘Infrared Thermal Imaging, Fundamental, Research and Applications, 2nd Edition.

Wardlow, B., Egbert, Stephen., (2008). Large-area crop mapping using time-series MODIS 250 m NDVI data: An assessment for the U.S. Central Great Plains. Remote Sensing of Environment. 112. 1096-1116. 10.1016/j.rse.2007.07.019.

Warren, R., Price, J., Vanderwal, J., Cornelius, S., Sohl, H., (2018). The implications of the United Nations Paris Agreement on climate change for globally significant biodiversity areas. Climatic Change. 10.1007/s10584-018-2158-6.

Weier, J., Herring D., (2000). Measuring Vegetation (NDVI and EVI).

Weiss, J.L, Gutzler, D.S., Coonrod, J.E.A., Dahm, C.N., (2004). Seasonal and inter-annual relationships between vegetation and climate in central New Mexico, USA. Journal of arid Environments 57(4): 507–534.

Wellman, H., (1979). An Uplift Map for the South Island of New Zealand, and a Model for Uplift of the Southern Alps.

West systems., (2012). Portable diffuse flux meter with LI-COR CO2 detector Handbook.

Won-Taek & Kang, Seonghun & Park, Keunbo & Lee, Jong-Sub. (2016). Evaluation of Active Layer Depth using Dynamic Cone Penetrometer. Journal of the Korean Geoenvironmental Society. 17. 49-54. 10.14481/jkges.2016.17.1.49.

Zenmuse XT2 User Manual, (2019). Image retrieved January 28th 2019.

Zhang, G.L., Xu, X.L., Zhou, C.P., Zhang, H.B., Ouyang, H., (2011). Responses of grassland vegetation to climatic variations on different temporal scales in Hulun Buir Grassland in the past 30 years. Journal of Geographical Sciences.